Chapter 12

Damping Ring

12.1 Damping Ring Overview

12.1.1 Layout of the system

The positron beam is generated at Sector 1 by bombarding a tungsten target with an intense electron beam. The positron beam is subsequently accelerated to 1.1 GeV with the S-band linac before injected to the damping ring (DR) at the end of Sector 2. A transport line from the linac to DR (LTR) is incorporated with an energy compression system(ECS) that rotates the longitudinal phase space to compress the energy spread within the energy acceptance of the DR. After staying 40 ms (2 linac pulses) in the DR, the damped beam is extracted from the DR and resumed to the entrance of Sector 3 through a transport line (RTL). Fig. 12.1 shows the layout of the system. The bunch length of the extracted beam is compressed with the bunch compression system(BCS), which is embedded in the RTL.

12.1.2 Beam parameters

Beam parameters of the incoming beam are shown in Table 12.1. Since the energy spread of incoming positron beam is too large for the acceptance of the DR it is reduced by one third before injection by making use of the ECS. The DR thus must have a large acceptance in both of transverse and longitudinal plane.

Fig. 12.2 shows the injection aperture as a function of the emittance of the injected beam. Here, we have assumed the effective thickness of the injection septum to be 3 mm and the beta function at the injection point to be 120 m. The injection aperture is defined as the action of particles that have 2.5 sigma of injected beam. We also assume a minimum dynamic aperture of the LER to be 0.7 μm and 18 nm in horizontal and
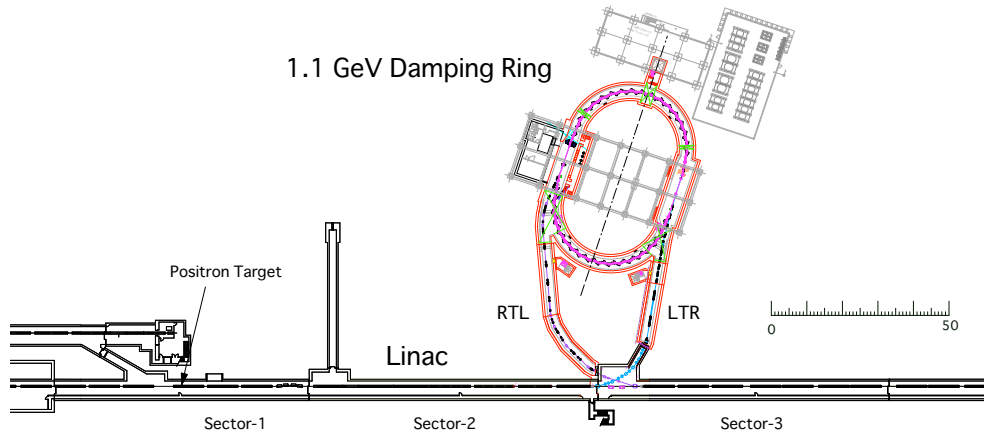
Figure 12.1: Layout of the damping ring system

Table 12.1: Parameters of the injected beam

	before ECS	after ECS	unit
Energy		1.1	GeV
Repetition frequency		50	Hz
Emittance		1.4	μm
Energy spread[†]	1.67	0.50	%
Bunch length[†]	2.67	11.7	mm
Number of bunches		2	
Bunch spacing		96	ns
Bunch charge		4	nC

† defined as extension that contains 99.7% divided by 6.

vertical plane, respectively. From Fig. 12.2 the horizontal emittance of the injected beam must be less than 14.5 nm. Taking into account the acceleration from 1.1 GeV to 4 GeV, horizontal emittance of the DR must be less than 53 nm. The vertical emittance of the DR, similarly, must be less than 10.5 nm. The emittance ratio is thus about 20 %, which is not difficult to realize. Note that the injection aperture is dominated by the septum width and less dependent on the emittance of the injected beam.

Parameters of the DR are shown in Table 12.2. The coupling of 5 % is much less than the required value of 20 %.

Though the maximum bunch-charge of the injector linac is 4 nC/bunch in design, we adopted the maximum stored current of 70.8 mA as an ultimate goal, which corresponds to 8 nC/bunch of the injected beam. Factor two is a margin for expected future
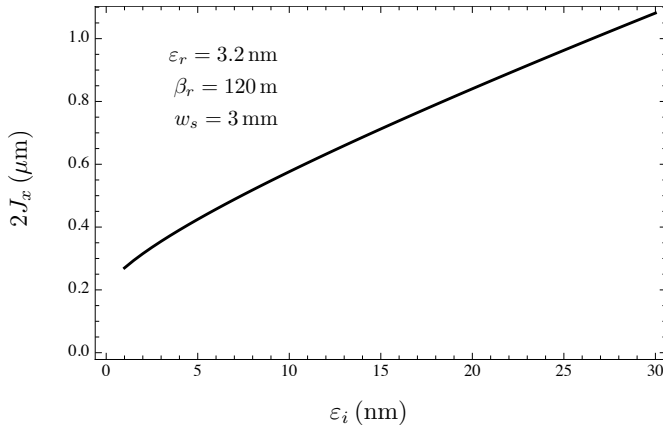
Figure 12.2: LER Injection Aperture

upgrades of the linac. Design parameters of every hardware component should be compatible with this value.

12.1.3 Lattice Design

Damping time. The emittance at extraction ε_{ext} is given by the equation,

$$\varepsilon_{ext} = \varepsilon_0 + (\varepsilon_i - \varepsilon_0)e^{-2T/\tau}, \tag{12.1}$$

where T is the store-time in the DR, 40 ms, and ε_0 and ε_i are the emittance of the DR and that of the injected beam, respectively. The second term of the Eq. (12.1) must be sufficiently smaller than the first term. Assuming their ratio to be 0.05 and the emittance of the DR to be 53 nm, which is the minimum requirement from the dynamic aperture of the LER, the damping time must be less than 12.8 ms.

Circumference. The damping time is in proportional to the bending radius ρ and to the circumference C as shown in the following equation,

$$\tau \;=\; \frac{3T_0}{r_e\gamma^3 J_x I_2} = \frac{3}{2\pi c\, r_e J_x}\frac{\rho}{\gamma^3}C. \tag{12.2}$$

The last equality holds for storage rings that includes only positive bends. Minimum value of the circumference, on the other hand, will be given by $c(2t_s + t_r + t_f)$, where $t_s = 96\,\text{ns}$ is the bunch separation and t_r and t_f are rise- and fall-time of the kickers. If $t_r = t_f = 100\,\text{ns}$ the minimum circumference will be 120 m. Taking into account of a margin for the bunch selection, we have chosen135 m as the circumference. In order to realize the damping time of 12.8 ms the bending radius thus needs to be 1.67 m, which means a magnetic field must be 2.2 T.

Table 12.2: Parameters of the Damping Ring

Energy		1.1		GeV
No. of bunch trains		2		
No. of bunches / train		2		
Circumference		135.49829		m
Max. stored current		70.8		mA
Energy loss / turn		0.091		MV
Hor. damping time		10.87		ms
Inj.-beam emittance		1400		nm
Emittance (h/v)		42.6 / 2.13		nm
Energy spread		5.5×10^{-4}		
Coupling		5		%
Extracted emittance (h/v)		43.5 / 3.15		nm
Cavity voltage		0.5	1.4	MV
Bucket height		0.8	1.5	%
Synchrotron tune	0.0153	0.0261		
Bunch-length		11.18	6.56	mm
Phase advance/cell (h/v)		64.39 / 64.64		deg
Momentum compaction		0.0143		
Bend-angle ratio		0.35		
No. of normal-cells		40		
RF frequency		509		MHz
Chamber diameter (h/v)		34 / 24		mm

Reverse-bend FODO. Since the inner diameter of the chamber, 24 mm, is relatively large it will be difficult to design a bend having the field greater than, say, 1.5 T. Therefore we have adopted a special lattice, "Reverse-bend FODO", that enables shorter damping time using a relatively low field[1]. In the proposed lattice one of the bends in the ordinary FODO is reversed in its bend direction while preserving the bend radius. Let r be a bend-angle ratio of the reversed bend to the normal positive bend, the damping time, τ, is given by the following equation,

$$\tau = \frac{3T_0}{r_e \gamma^3 J_x I_2} = \frac{3}{2\pi c\, r_e J_x} \frac{\rho}{\gamma^3} C \frac{1-r}{1+|r|} \,. \tag{12.3}$$

The factor $(1-r)/(1+|r|)$ originates from that the total bend angle increases to $2\pi(1+|r|)/(1-r)$ in this lattice. One can see that for the given damping time, bend-radius can be increased by a factor $(1+|r|)/(1-r)$. From Eq. (12.3), for a given circumference

and a bend-radius, the bend-angle ratio r can be expressed as a function of τ. Fig. 12.3 shows the bend-angle ratio as a function of the damping time assuming $\rho = 2.7$ m or equivalently $B = 1.36$ T. We have chosen the parameter $r = 0.35$ that ensures the damping time of 10 ms.
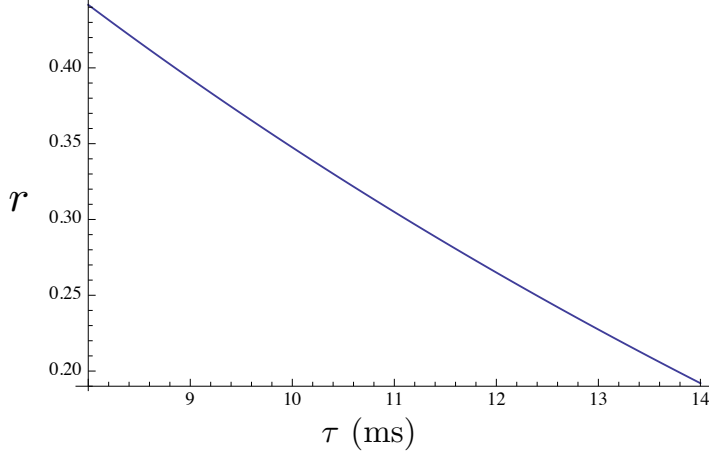

Figure 12.3: Bend-angle ratio as a function of damping time

Thus, by adopting the proposed lattice, the required damping time can be realized with dramatically low magnetic field. One should note, however, that the circumference is given by $C = 2\pi\rho(1+|r|)/(1-r)+L_1$, with L_1 being a total length except bends. For a given circumference the L_1 get shorter for larger r, which means the ring must be more densely packed with bends. With $\rho = 2.7$ and $r = 0.35$ we obtain $L_1 = 100$ m.

Number of cells. Fig. 12.4 shows an example of optical functions of the reverse-bend FODO cell. The symbol B2 designates a reverse bend. The bend angle of B1 and B2 is θ and $-r\theta$, respectively. In a thin lens approximation the momentum compaction factor (α_p) is given by[1]

$$\alpha_p = G(r,\mu)\theta^2, \tag{12.4}$$

$$G(r,\mu) = \frac{(1+r^2)(3+\cos\mu) - 8r}{16\sin^2(\mu/2)}, \tag{12.5}$$

where μ is the phase advance per cell. An equal phase advance for the horizontal and vertical planes was assumed. The emittance, on the other hand, is given by the following expressions in the thin-lens model[1]:

$$\varepsilon_0 = C_q \frac{\ell\theta^2}{\rho}\gamma^2 F(r,\mu), \tag{12.6}$$

$$F(r,\mu) = \frac{1}{24\sin^2(\mu/2)\sin\mu}\left\{1 + 5|r| + r^2 + \right.$$
$$\left. 2(5 - 12r - 2|r| + 5r^2)\cos^2(\mu/2) + (1 - |r| + r^2)\cos^2\mu\right\}, \tag{12.7}$$

515

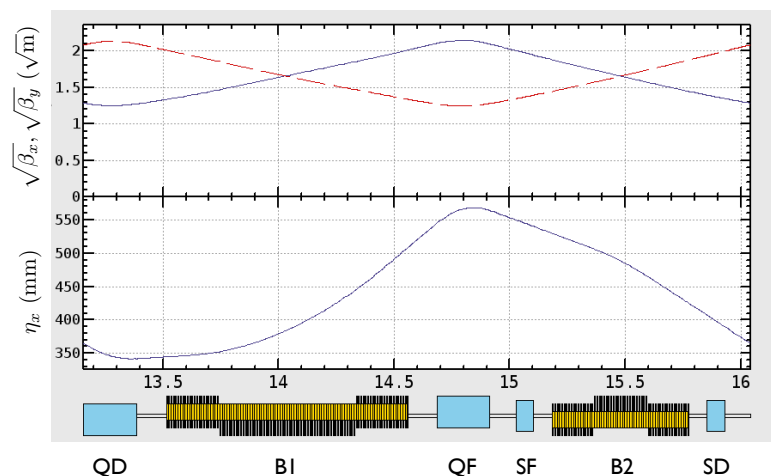Figure 12.4: An example of optical functions of the reverse-bend FODO cell. B2 is a reverse bend. The bend angle of B1 and B2 is θ and $-r\theta$, respectively.

where ℓ is the half cell-length, ρ the bending radius, and $C_q = \frac{55}{32\sqrt{3}}\frac{\hbar}{mc}$. Denoting the number of cells by N_c, the bend-angle θ and the half cell-length ℓ are expressed as $\theta = 2\pi/N_c(1-r)$ and $\ell = C/2N_c$. If we fix the N_c and r, by eliminating μ from Eqs. (12.4) and (12.6), the emittance ε_0 can be expressed as a function of α_p as shown in Fig. 12.5. Requirement on the α_p is not strict but a larger α_p is preferable from
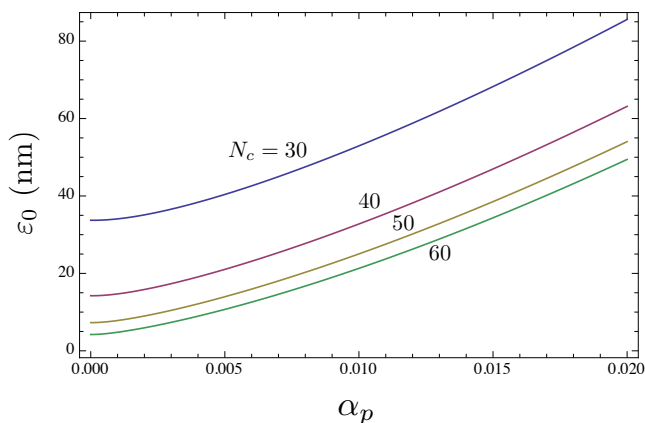

Figure 12.5: Emittance as a function of momentum compaction factor for various number of cells.

the viewpoint of longitudinal instabilities, especially for the microwave instability due to CSR wake, as described in the subsection 12.2. Under the requirement that the emittance should be less than 53 nm, a larger number-of-cells is preferable to obtain larger α_p. From Fig. 12.5 the N_c larger than, say, 50 is not so effective to get larger α_p.

On the other hand the magnet length of B2 is given by $L(B2) = 2\pi\rho\, r/N_c(1-r)$ and it is 0.228 m and 0.183 m for $N_c = 40$ and $N_c = 50$, respectively. We have adopted $N_c = 40$ since it is considered to be difficult to design a bend which has a high-field of 1.36 T and a length shorter than 0.2 m from a viewpoint of the leakage field.

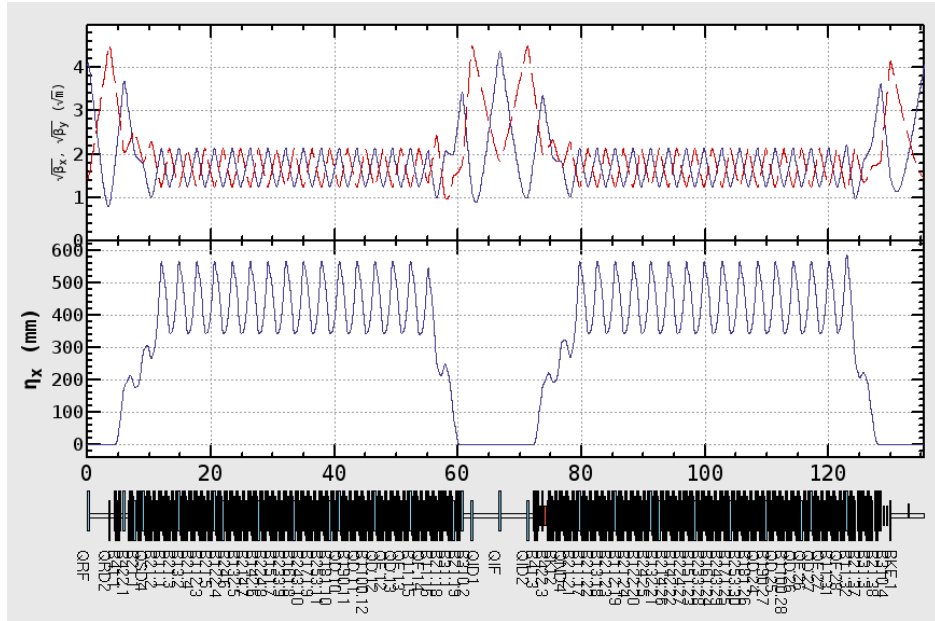**Linear optics.** Optical functions of the normal is shown in Fig. 12.4. For the en   h a

Figure 12.6: Optical functions of the DR. Upper and lower figure show beta- and dispersion functions, respectively.

length of 8.85 m. Each straight section consists of two drifts with a horizontal-focus quad in between them. RF cavities occupy one of drifts in the straight section for extraction. Since the two straight sections are not identical the ring has no super-periodicity. Dispersion function is suppressed to zero at the straight section, using 5 or 6 independent quads in each end of the arc. Fig. 12.7 and Fig. 12.8 shows optics of the straight section for the injection and extraction, respectively. Septum magnets for the injection is placed in the straight between the quads QID1 and QIF, while those for the extraction is in the straight between the quads QRF and QRD2. Kicker magnets for the injection is placed in the both side of QNF4, while those for the extraction is placed between QSF3 and QRD1. Since the bending magnets are densely packed in the ring the ceramic chambers for the kickers inevitably receive a synchrotron radiation (SR) on the side wall. For the injection kicker, maximum SR power is estimated to be 16 W in the chamber length of 50 cm. A mask is built at the near side of the bend to protect the welded part of the chamber although its shadow does not cover the whole length of chamber.
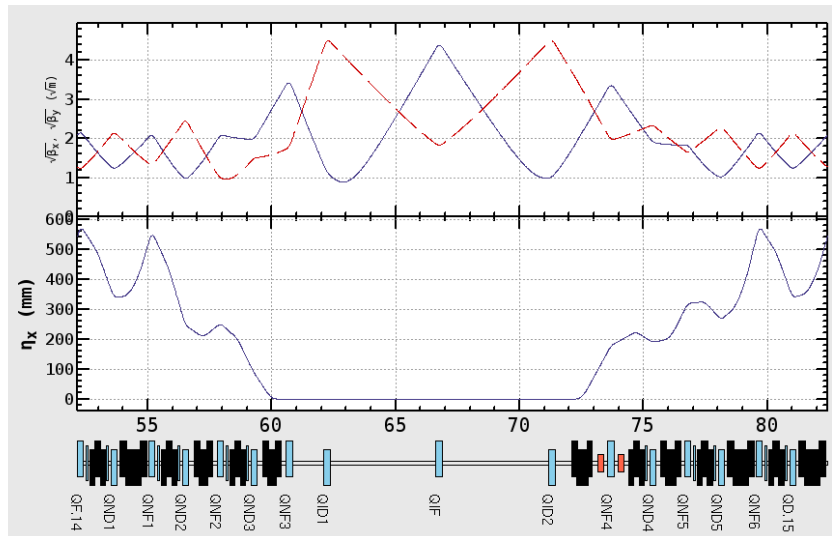
Figure 12.7: Optics of the straight section for the injection.

For the chromaticity correction a sextupole magnet is located near to every quads in the arcs. Sixteen independent sextupole families are available, including 2 families in the normal-cell and 14 families at the dispersion-suppressor quadrupoles. Fig. 12.9 shows a dependence of tunes and beta functions on the momentum. Though the tunes deviate from the design value by 0.15 and beta functions changes 11 % in the momentum band-width of ± 1.5 % the particles stay stable as described in subsection 12.1.4
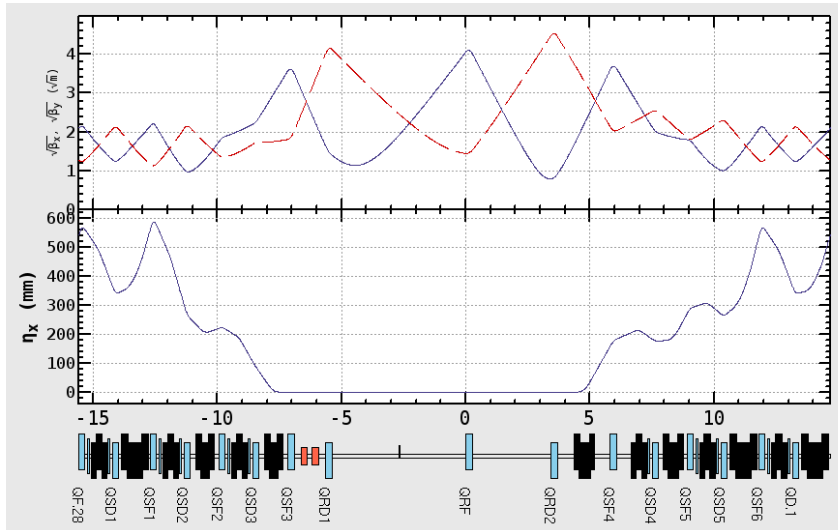
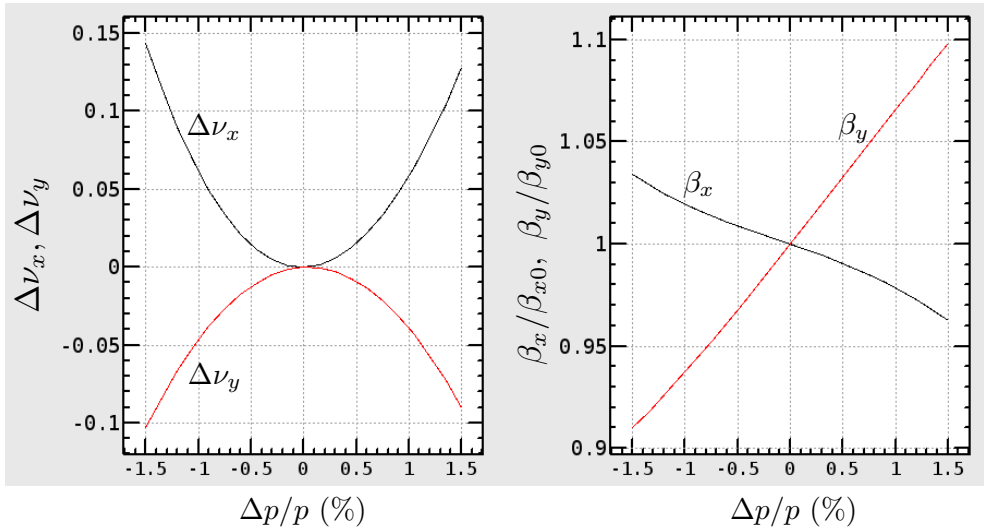Figure 12.8: Optics of the straight section for the extraction.

Figure 12.9: Momentum dependence of tunes and the beta functions.

519
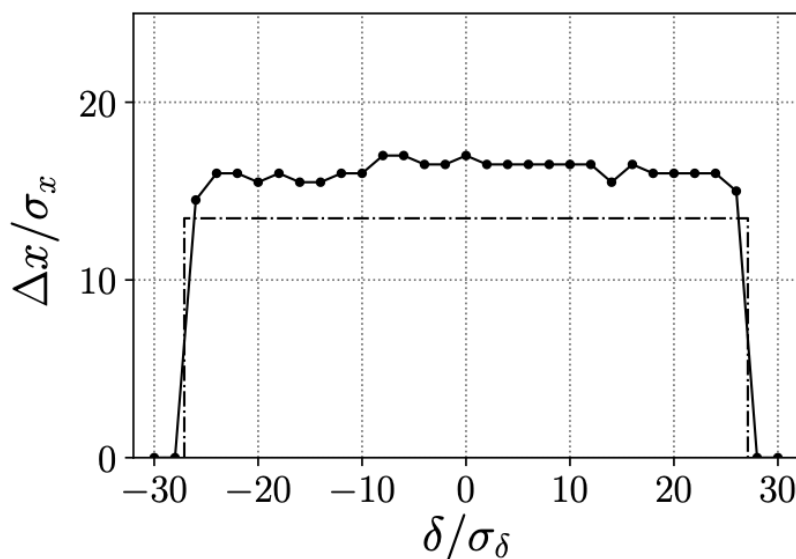
12.1.4 Dynamic aperture and acceptance

Figure 12.10: Acceptance of DR, where σ_x and σ_δ are equilibrium horizontal beam size and momentum spread, respectively. The broken line indicates the required acceptance.

Acceptance of the ring should be larger than the injected beam. We define the minimum acceptance as 3.3-sigma of the betatron beam-size, or equivalently 10 times the emittance of the injected beam, and $\pm$ 1.5 % in the momentum deviation. Dynamic aperture (DA) is optimized by the Down-hill simplex algorithm [2]. Available optimization knobs are field strength of sextupole magnets. Tune chromaticity is also important to avoid unexpected beam instability at high bunch current operation. The linear tune chromaticity is therefore considered during the DA optimization using method described in Ref. [3].

In the simulation a particle with an initial action, which is identical for the horizontal and vertical plane, is launched in the phase space and tracked until being lost or reaching given maximum turns, for each initial momentum deviation. Effects of radiation damping and quantum excitation are not included. A result of tracking simulation shown in Fig. 12.10, where a maximum amplitude Δx of particles that stays stable during 2000 turns is plotted as a function of the momentum deviation δ. Figure 12.10 shows that the acceptance of DR is larger than the injected beam. Although the maximum turns of 2000 is much less than that corresponding to the damping time ($\sim$25000 turns), the tracking result did not change so much because particles with large amplitude are immediately scraped by the physical aperture of the vacuum chamber. The acceptance with machine error is studied in the following subsection 12.1.5.

12.1.5 Error tolerance

Table 12.3: Machine errors assumed in the simulation

	Δx [mm]	Δy [mm]	$\Delta\theta$ [mrad]	$\Delta K/K$ [%]
Bending magnet	0.15	0.15	0.3	0
Quadrupole magnet	0.15	0.15	0.3	0.1
Sextupole magnet	0.15	0.15	0.3	0.2
BPM*	0.15	0.15	1	-

* Measurement error of 10 μm is assumed.

Numerical simulation on orbit correction is performed assuming realistic alignment errors and field errors of magnets. Misalignment and measurement error of Beam-Position-Monitor (BPM) are also taken into account. All machine errors are assumed to be Gaussian distributed whose standard deviation is summarized in Table 12.3. The horizontal orbit correction is performed mainly using back-leg windings of the B2 bending magnets. Skew dipole winding coils of all sextupole magnets are utilized in the vertical orbit correction.

A simulation result is shown in Fig. 12.11, where closed orbits after Fig. 12.11(a) and before Fig. 12.11(b) the orbit correction are plotted together with field strength of dipole correctors. The orbit correction effectively improves the vertical emittance from
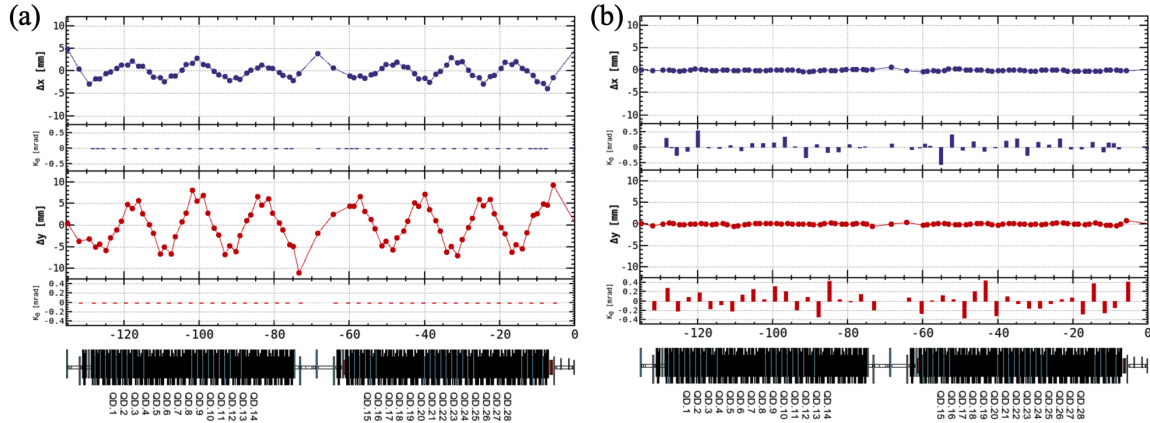

Figure 12.11: Simulation result of orbit correction, where closed orbits measured at BPMs after (a) and before (b) orbit correction are shown.

$\varepsilon_y = 7.2$ nm to 13 pm which satisfies the design value.

Two hundred of simulations are performed in different sets of random numbers used for the machine error. The distribution of horizontal and vertical emittances after orbit

correction are shown in Fig. 12.12. Figure 12.12 indicates that vertical emittance after orbit correction is well below its design value in all cases. DA after orbit correction is
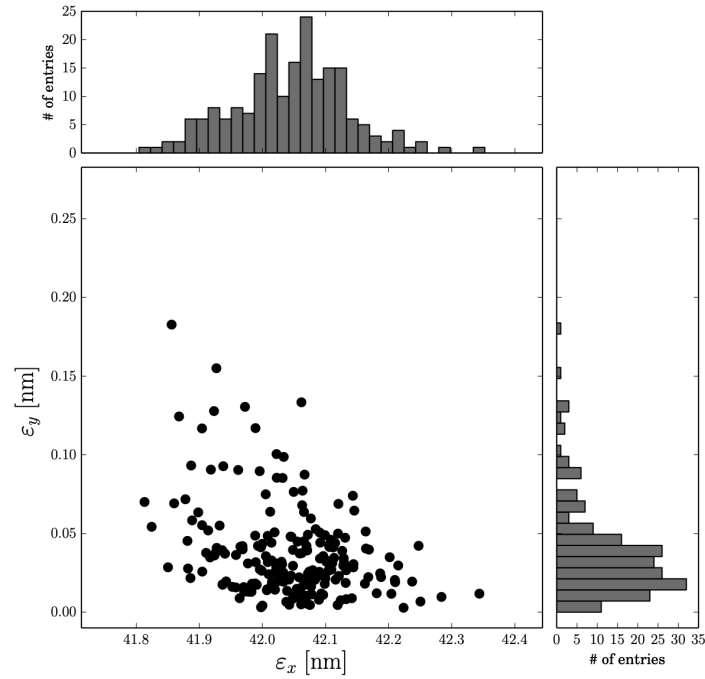

Figure 12.12: Distribution of horizontal and vertical emittances after orbit correction.

shown in Figure 12.13. The DR acceptance is comparable to its design value in the average sense even without correction of beam optical functions.

In a summary, horizontal and vertical orbit correction is sufficient to reach the machine performance required by the SuperKEKB main ring. It is also expected that correction of betatron and dispersion functions with quadrupole families further improves emittance and DA.
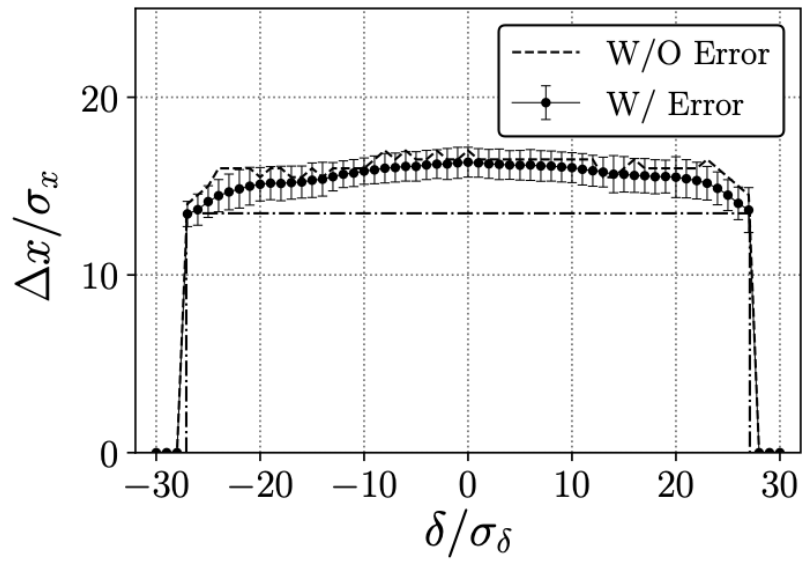
Figure 12.13: Acceptance of DR after orbit correction, where the dots and bars indicate the average and standard deviation of 200 samples, respectively.

12.1.6 Tunnel design

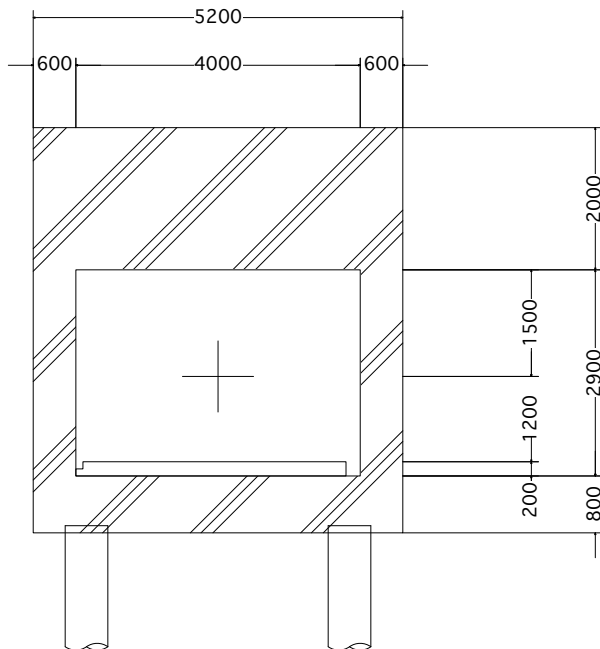The general layout of the cross section in the arc area is shown in Fig. 12.14.

Figure 12.14: Cross section of the arc tunnel

Since the DR tunnel is rather shallow from the ground (2.3 m from the ground to the ceiling of the tunnel) radiation-safety regulations on the beam loss in the DR are expected to be stringent. The energy tail in the linac being the most concern, energy collimators are placed in the first arc of the LTR, that truncate the tails and define a clear-cut energy band-width of the beam prior to injection to the DR (see section 12.8 for details). The beam loss in the collimator depends on the compression ratio and it amounts to 10 % and 25 %, for the energy band-width of ± 1.5 % and ± 0.8 %, respectively. These losses are acceptable owing to thick shield structure surrounding the collimators, as described as follows.

The extraction from the linac and re-injection to it are made at the existing Second Switch Yard (SY2). The first part of the LTR line passes through an existing small tunnel called the Catcher Section that connects the SY2 and newly built LTR tunnel. Though top slab of the tunnel of the SY2 is made partly of heavy concrete it is insufficient to shield the radiation from the beam losses there. Therefore a new concrete structure of 1.2 m depth and 2.7 m width, that includes 0.4 m iron block in depth, was added on the top slab of the SY2. We also added a new concrete of 2.8 m in depth on top slab of the Catcher Section whose top slab is only 0.5 m in depth.

The injection area of the DR is also expected to have relatively large beam losses of

1 %. Depth of the top slab in the injection area is 2.2 m including iron block of 0.4 m in depth.

12.2 Beam Instabilities

Beam instabilities are major concerns in the DR design because the design bunch-charge is relatively high. Since it was found that the instability due to the coherent synchrotron radiation (CSR) severely damages beam performance for shorter bunch-length and lower momentum compaction, we tried to find a good shape of the beam pipe and other parameters for suppression of the instability. The electron cloud effect has been also studied.

12.2.1 Coherent Synchrotron Radiation

In order to estimate the microwave instability, longitudinal wake potential per turn has been estimated for each vacuum component and RF cavity using GdfidL [49] with 0.5mm bunch length, which is less than 1/10 of the natural bunch length. The resistive-wall wake has been obtained by analytic formula. The number of vacuum components are listed in Table 12.4. We chose a design with antechamber for the DR beam pipe to reduce the instability caused by the wake field of vacuum components. Figure 12.15 shows the calculated wake potentials using numerical calculation by Oide's code [5]. The CSR wake is 100 times higher than the other components in this case. With this wake potential, we have made multiparticle tracking simulation for Gaussian beam to estimate the degradation of the beam quality through broadening the beam energy spread and lengthening the bunch length. In order to mitigate the instability, we decided to change the momentum compaction factor from 0.0019 to 0.0141 and the RF voltage from 0.261 MV to 1.4 MV.

Table 12.4: Number of vacuum components.

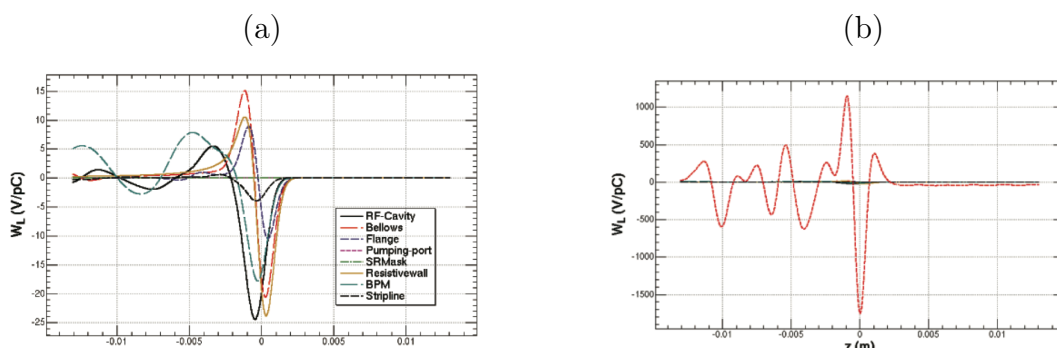| Component	No. of component
RF cavity	2
Bellows	88
Flange	176
SR mask	176
Resistive wall	135.5 [m]
BPM	82
Strip line	1

(a) (b)

Figure 12.15: Longitudinal wake potential caused by (a)vacuum components and (b)CSR.

The shape of cross section of the DR beam pipe was designed to mitigate the CSR instability. We calculated the wake potential of CSR for several shapes and made multiparticle tracking simulation using the potential [6]. The antechamber with smaller pipe height brings better situation due to the shielding effect of the beam pipe. The low frequency components of the wake fields are cut off by the shielding effect. We designed the actual cross section of the beam pipe also taking into account of easiness of the production as shown in Figure 12.16.
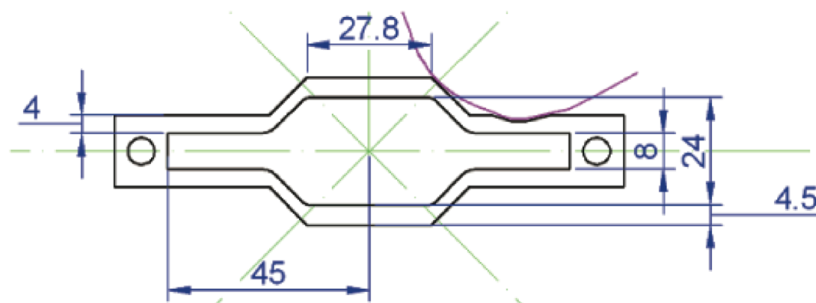

Figure 12.16: Proposed beam pipe cross section.

The wake potential by CSR is calculated by two independent codes; analytical formulae for steadystate CSR in uniform rectangular cross-section [7, 8] and Oides ' s code based on parabolic equations [9] . The results agree well for rectangular cross section chambers. Parameters of dipole magnets that were used for the wake potential calcuration are tabulated in Table 12.5.

In the multi-particle tracking simulation we assumed a damped beam with Gaussian distribution in the longitudinal phase space as well as the incoming beam from the linac as shown in the Fig. 12.17. We estimate the degradation of the beam quality through

Table 12.5: Bending magnet parameters of DR

Bend	Length[m]	Bending angle	No. of elements
B1	.74248	.27679	32
B2	.28654	.09687	38
B3	.39208	.12460	6
B4	.47935	.15218	2
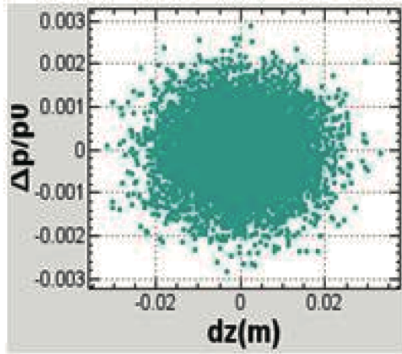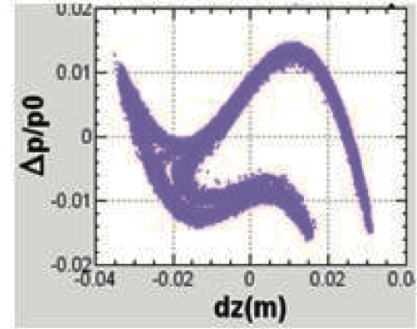
(a)   (b)

Figure 12.17: Longitudinal phase space for tracking simulation in DR: (a) Gaussian beam, (b) beam from the linac before damping..

broadening the beam energy spread and lengthening of the bunch length with the wake potential that was calcurated for designed cross section of the beam pipe. The both tracking result showed similar behaviour. Figure 12.18 show the tracking results using the beam from the linac. In the tracking we used up to 5,000,000 macro particles to confirm the convergence in the number of particles. In the case of 30 kicks per turn in tracking, the bunch length and energy spread become 10% and 14% larger, respectively than initial value at 5×10^{10} particles/bunch, which correspond to 8 nC per bunch. The importance of number of kick per turn N is related the longitudinal dilution through momentum compaction factor α, energy spread σ_δ, circumference of ring C and the wave length of instability $\lambda = 0.3$mm. When we calculate $\sigma_\delta \times \alpha \times C/N$ using a DR parameter and N=30, it becomes 0.035mm. Tracking results are unchanged if N >=30, which shows that the follwing condition, $\sigma_\delta \times \alpha \times C/N << \lambda$ is of greate importance. We expect that the increasing of the bunch length and the energy spread are acceptable in the actual operations.

The study using Vlasov-Fokker-Planck (VFP) code [10, 11] was also done. Figure 12.19 shows the growth of bunch length and energy spread as a function of bunch
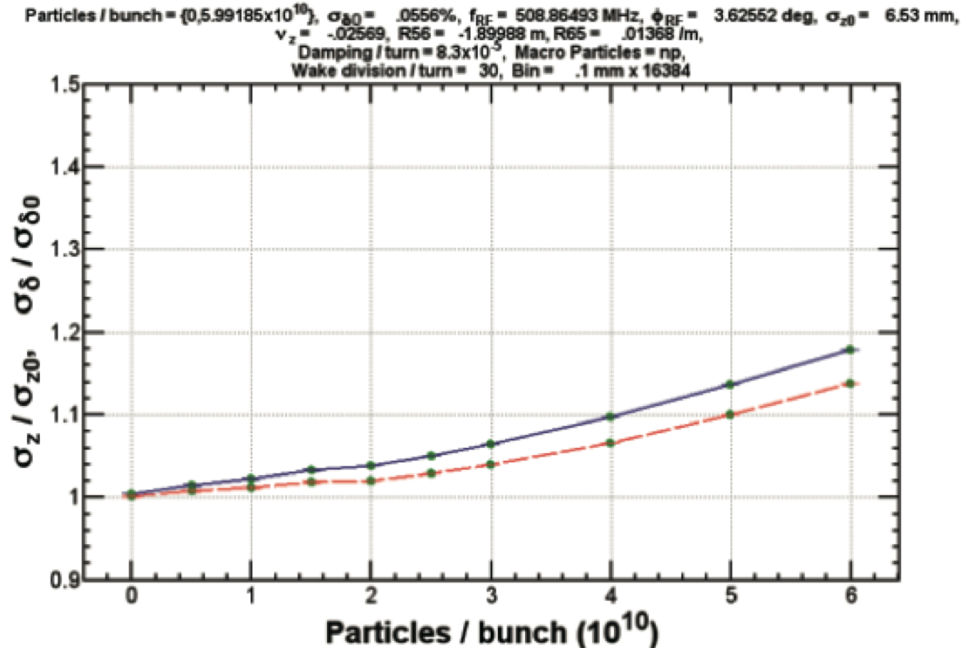
527

Figure 12.18: Bunch length and the energy spread as a function of the bunch intensity.

intensity [12]. At low bunch current, the CSR wake alone causes negligible growth in bunch length and energy spread. The geometric wake induces linear growth in bunch length due to potential well distortion when the bunch charge is below a critical value, under which no instability is observed. Comparing the results of different wake cases, it can be clearly seen that the bunch lengthening is mainly due to geometric wake when the current is below the critical value, while CSR effect is dominant if bunch current is higher than the critical current. The instability threshold is enough higher than the nominal bunch charge.

12.2.2 Electron Cloud Instability

A study with early design parameters showed that the threshold of the strong head-tail instability(SHTI) by the electron cloud was near the estimated electron density if no cares were taken. In order to keep an enough margin against the SHTI, TiN coating on the chamber wall to reduce the secondary emission yield(SEY) as well as increase of the synchrotron tune from 0.004 to 0.015 hass been proposed. The following is the result of the design study on the SHTI which takes into account of the TiN coating and the raised synchrotron tune.

The threshold of the electron density $\rho_{e,th}$ of the SHTI near the beam is given by
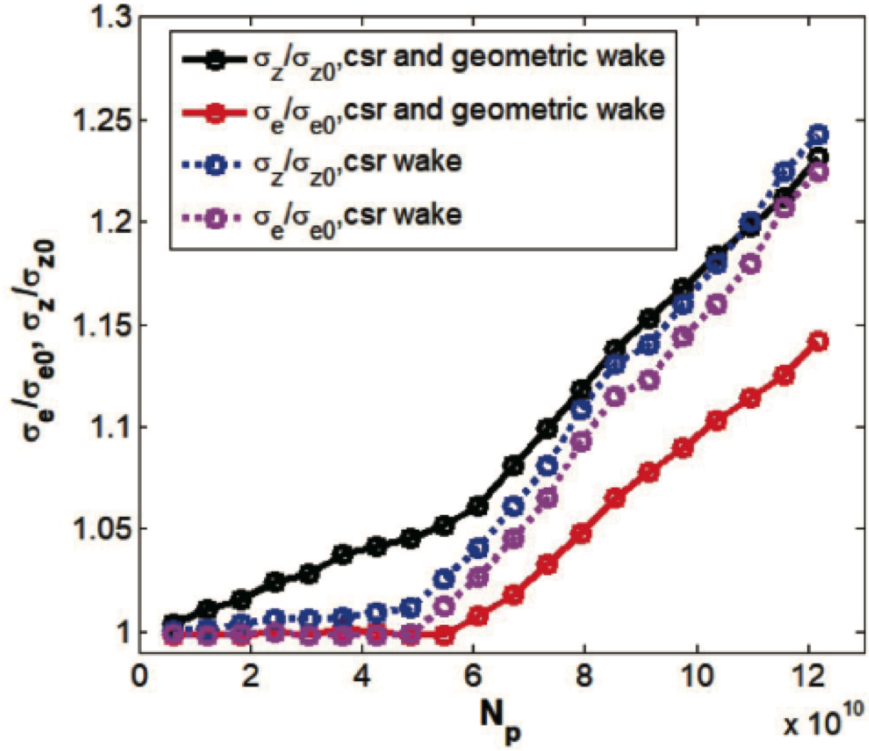
Figure 12.19: Bunch length and energy spread that were caluculated by VFP code at different bunch intensity with various types of wake.

[13]

$$\rho_{e,th} = \frac{2\gamma\nu_s\omega_e\sigma_z/c}{\sqrt{3}KQr_e\beta_y L} \tag{12.8}$$

where γ is the relativistic factor, ν_s the synchrotron tune, σ_z the bunch length, β_y the vertical beta function, L the circumference, r_e the classical electron radius and c the speed of light. K, the enhancement factor due to the cloud size, is taken as 3 here. Q=min[5, $\omega_e\sigma_z$/c] characterizes damping of electron coherent motion due to the nonlinear interaction with the beam. ω_e is the oscillation frequency of electrons in the beam potential given as

$$\omega_e = \sqrt{\frac{\lambda_+ r_e c^2}{\sigma_y(\sigma_x + \sigma_y)}}. \tag{12.9}$$

where σ_x and σ_y are horizontal and vertical beam size, respectively. $\lambda_+ = N_+/(2\sigma_z)$ is the line density of the bunch where N_+ is the number of positrons in the bunch.

Table 12.6 shows beam parameters for the evaluation of the threshold according to Eq. (12.8). The result is shown in Table 12.7.

Table 12.6: Beam parameters for the threshold evaluation of the strong head-tail instability due to the electron cloud

Energy		1.1		GeV
Circumference		135.5		m
Equilibrium emittance(x/y)		42.0/2.10		nm
Beta function(x/y)		4.0/4.4		m
Bunch population		5×10^{10}		
Cavity voltage	0.5	1.0	1.4	MV
Equilibrium bunch length	11.07	7.78	6.57	mm
Synchrotron tune	0.0152	0.0216	0.0256	

Table 12.7: Theoretical threshold of electron density of the strong head-tail instability due to the electron cloud

Cavity voltage(MV)	$\rho_{e,th}(10^{13}m^{-3})$	$\rho_{e,th}L$ $(10^{14}m^{-2})$
1.4	1.26	17.1
1.0	1.07	14.5
0.5	0.75	10.2

In a tracking simulation of the SHTI by a computer code PEHTS2 [15], a very small blowup of the vertical beam size was observed at the cloud density of 40 percent of the analytic estimate. In the case of the cloud density of 80 percent of the analytic estimate, the blowup was clearly observed.

The density of the electron cloud was calculated by a computer code CLOUDLAND [14] in various conditions. Table 12.8 shows parameters used in the simulation, where δ_{max} is a peak value of the SEY and E_{max} is the energy of the primary electron at δ_{max}. Several parameters in Table 12.6 are not the same as final design parameters because the simulation has been done during the phase of the design study.

The result of the electron density is shown in Table 12.9, where SR denotes a ratio of photon-flux to the design flux. We assume that $\delta_{max}=1$ will be achieved by TiN coating. In the case of SR=0.1, the photon flux is intentionally reduced to one-tenth of the design flux in order to simulate the effect of photon flux reduction by the antechamber.

Table 12.8: Parameters used to calculate the electron density by a computer simulation

Energy	1.0	GeV
Circumference	135.5	m
Equilibrium emittance(x/y)	12.6/0.63	nm
Beta function(x/y)	2.5/6.5	m
Bunch population	5×10^{10}	
Bunch length	5.0	mm
The number of bunch	4	
Bunch separation	98	nm
Pipe radius	16	mm
Dipole field	1.27	T
Quad gradient	7.78	T/m
SEY δ_{max}	2.0/1.0	
SEY E_{max}	250	eV

Table 12.9: Electron density obtained by a computer simulation

δ_{max}	SR	Drift($10^{12}m^{-3}$)	Bend($10^{12}m^{-3}$)	Quad and Sext($10^{12}m^{-3}$)
2	1	1.3	0.6	0.5
1	1	0.4	0.5	0.15
1	0.1	0.15	0.11	0.03

The integrated electron density along the ring was calculated as a product of the electron density and the length of each sections which are 73.2, 36 and 26.8m in drift, bend, and quad and sextupole sections, respectively. The result is shown in Table 12.10.

Table 12.10: Integrated electron density ρ_eL

δ_{max}	SR	ρ_eL($10^{14}m^{-2}$)
2	1	1.30
1	1	0.51
1	0.1	0.16

In the case of $\delta_{max}=1$ and SR=1, ρ_eL is $0.51\times10^{14}m^{-2}$. Comparing this value with the threshold of integrated electron density $\rho_{e,th}$L of the SHTI $4.1\times10^{14}m^{-2}$ for the cavity voltage of 0.5MV, which is 40 % of the threshold density by analytic formula, it

is concluded that the SHTI will be suppressed if the chambers are TiN-coated and the cavity voltage is greater than 0.5MV. Grooved surface on the wall of dipole chambers and ante-structure of the chambers, which is required in order to install photon masks, will also contribute to the reduction of the electron density.
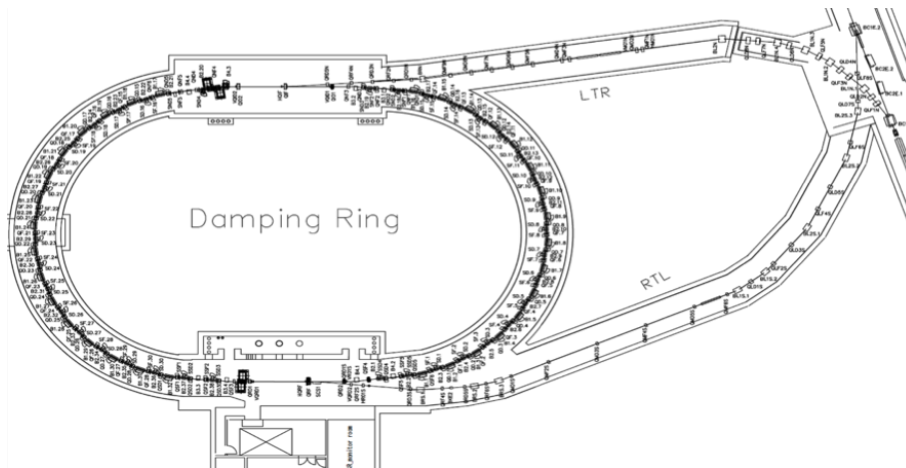
Figure 12.20: The lattice configuration of the damping ring with the beam transports.

12.3 Magnet system

12.3.1 Introduction

The magnets of the damping ring are shown in Table 12.11. The parameters of the coils are shown in Table 12.12. The lattice configuration is shown in Fig. 12.20. The straight sections are used for the RF, injection and extraction. In the arc cells, the correction coils of the B2 are used for the horizontal orbit corrector and those of SD the vertical ones. The independent steering magnets are only used at the straight section. Since the bore diameters of the arc normal cell magnets are 46mm, the larger bore magnets are adopted for the straight sections where the larger apertures are required for the injection and extraction system.

The power supplies are shown in Table 12.13. The MG-ST power supplies for the horizontal steering magnet are formerly used in old LER for solenoid against the electron cloud instability. The others are newly manufactured. The configuration of the power supplies in the power station is shown in Fig. 12.21. The power supplies for the main magnets have the phase shifting transformers to balance the power consumption between three phases of the mains AC.

12.3.2 Preparation of the magnets

Before installing the magnet to the accelerator tunnel, the magnetic field measurements are made for all magnets. Two measurement systems shown in Fig. 12.22 are manufactured; the system with the long flip coil for the dipole field measurements and that with the harmonic coil for the multipole field measurements. Parameters of the

533

Table 12.11: The magnets of the damping ring and beam transport.

No.	magnet type	Bore or Gap [mm]	length [mm]	weight [kg]	used	location	manufacturer
1	B1	46	690	1850	32	DR	SIGMA PHI
2	B2	46	230	750	38	DR	SIGMA PHI
3	B3	46	334	1000	4	DR	SIGMA PHI
4	B4	46	420	1200	4	DR	SIGMA PHI
5	QM(F)	46	200	210	37	DR	SIGMA PHI
6	QM(D)	46	200	210	37	DR	SIGMA PHI
7	QRF	110	369	1000	3	DR	TOKIN
8	QRD	60	287	400	7	DR	TOKIN
9	SX	70	75	135	75	DR	SIGMA PHI
10	STV_C	60	100	56	3	DR	TECNO
11	STH_H	120	100	82	1	DR	TECNO
12	STH_H1	60	100	101	1	DR	TECNO
13	STH_H2	124	100	110	1	DR	TECNO
14	BC1E	50	1000	4240	2	LTR/RTL	TOKIN
15	BC2E	25	1220	2800	2	LTR/RTL	MITSUBISHI
16	BLN	50	650	1410	5	LTR/RTL	TOKIN
17	BRN	50	500	620	1	LTR/RTL	TOKIN
18	BS	28	750	820	8	LTR/RTL	TOKIN
19	QLN1	98	400	1061	3	LTR/RTL	Beam Seiko
20	QLN2	98	400	1061	5	LTR/RTL	Beam Seiko
21	QLS	64	350	765	7	LTR/RTL	TIME.,Ltd
22	QMN	48	250	700	12	LTR/RTL	TAKANO GIKEN
23	QMS	30	200	300	13	LTR/RTL	TAKANO GIKEN
24	QRN	39	340	140	2	LTR/RTL	TAKANO GIKEN
25	SFS	84	100	180	2	LTR/RTL	TAKANO GIKEN
26	StH56	100	150	75	2	LTR/RTL	TOKIN
27	StHerH	80	283	-	12	LTR/RTL	Novosibirsk Russia
28	StHerV	80	283	-	14	LTR/RTL	Novosibirsk Russia
29	StV128	180	150	120	5	LTR/RTL	TOKIN
30	StV56	100	150	75	2	LTR/RTL	TOKIN

Table 12.12: The parameters of the coil of the magnets.

No	magnet type	main coil					Correction coil				
		peak voltage [V]	peak current [A]	Number of turns per coil [T]	Nominal Ampere Turns per coil [A T]	Number of coils per magnet	peak voltage [V]	peak current [A]	Number of turns per coil [T]	Nominal Ampere Turns per coil[A T]	Number of coils per magnet
1	B1	15.5	900	16	14400	2	4.6	7.7	39	300	2
2	B2	9.4	880	16	14080	2	2.6	7.7	39	300	2
3	B3	9.7	800	16	12800	2	3.2	7.7	39	300	2
4	B4	10.9	800	16	12800	2	3.4	7.7	39	300	2
5	QM(F)	5.2	330	16	5280	4	0.6	5.0	10	50	4
6	QM(D)	3.8	247.5	16	3960	4	0.6	5.0	10	50	4
7	QRF	11.3	500	25	12500	4	1.2	10.0	12	120	4
8	QRD	4.9	300	16	4800	4	0.7	10.0	10	100	4
9	SX	5.0	150	20	3000	6	2.5	10.0	50	500	6
10	STV_C	0.8	10	52	520	2	-	-	-	-	-
11	STH_H	2.2	10	86	860	2	-	-	-	-	-
12	STH_H1	1.6	10	52	520	2	-	-	-	-	-
13	STH_H2	3.4	10	137	1370	2	-	-	-	-	-
14	BC1E	23.0	498	54	26892	2	1.8	10.0	30	300	2
15	BC2E	25.3	450	80	36000	2	11.0	5.0	144	720	2
16	BLN	19.6	468	60	28080	2	2.4	10.0	30	300	2
17	BRN	10.2	468	44	20592	2	2.0	10.0	30	300	2
18	BS	7.8	468	28	13104	2	2.6	10.0	30	300	2
19	QLN1	-	80	110	8800	4	-	-	-	-	-
20	QLN2	-	80	110	8800	4	-	-	-	-	-
21	QLS	8.0	40	80	3200	4	-	-	-	-	-
22	QMN	8.0	37	110	4070	4	-	-	-	-	-
23	QMS	4.0	21	80	1680	4	-	-	-	-	-
24	QRN	4.4	25	70	1750	4	-	-	-	-	-
25	SFS	3.0	10	50	500	6	-	-	-	-	-
26	StH56	4.0	5	110	550	2	-	-	-	-	-
27	StHerH	25.0	5	648	3240	2	-	-	-	-	-
28	StHerV	25.0	5	648	3240	2	-	-	-	-	-
29	StV128	12.0	5	250	1250	2	-	-	-	-	-
30	StV56	4.0	5	110	550	2	-	-	-	-	-

Table 12.13: Power supplies for the damping ring and beam transports magnets.

PS TYPE	Number of power supplies	V [V]	I [A]	P [kW]	Load magnet Number	location	manufacturer
B1	1	700	900	630.0	B1-32	DR_1F	HITACHI
B2	1	500	880(850)	440.0	B2-38	DR_1F	HITACHI
B3	1	70	800	56.0	B3-4	DR_1F	NICHICON
B4	1	70	800	56.0	B4-4	DR_1F	NICHICON
QF	1	210	330	69.3	QM-28	DR_1F	NICHICON
QD	1	160	250	40.0	QM-28	DR_1F	NICHICON
QR	3	30	500	15.0	QRF	DR_1F	NICHICON
SF	1	200	150	30.0	SX-30	DR_1F	NICHICON
SD	1	200	150	30.0	SX-30	DR_1F	NICHICON
QS	18	15	330	5.0	QM	DR_M2F	NICHICON
BRN	1	20	310	6.2	BRN	DR_M2F	NICHICON
QM	7	15	300	4.5	QRD	DR_M2F	NICHICON
SFX	14	15	150	2.3	SX	DR_M2F	NICHICON
BC1E.1-2	1	70	480	33.6	BC1E-2	LINAC	NICHICON
BC2E.1-2	1	50	290	14.5	BC2E-2	LINAC	NICHICON
BL1N.1-4	1	120	490	58.8	BL1N-4	LINAC	NICHICON
BL2N	1	40	490	19.6	BL2N	DR_M2F	NICHICON
BRS.1-3	1	40	430	17.2	BRS-3	DR_M2F	NICHICON
BL1S.1-2	1	40	550	22.0	BL1S-2	DR_M2F	NICHICON
BL2S.1-3	1	50	550	27.5	BL2S-3	DR_M2F	NICHICON
LTR-Q	5	40	50	2.0	QMN	DR_M2F	IDX
LTR/RTL-Q	29	30	30	0.9	QMN,QLS,QMS	DR_M2F	IDX
QLN1	3	40	530	21.2	QLN1	LINAC	IDX
QLN2	4	80	90	7.2	QLN2	LINAC	IDX
QLD6N	1	40	50	2.0	QLN2	LINAC	IDX
MG-ST	44	± 50	± 10	0.5	ST , VSD	DR_M2F	CAEN
MG-ST	44	± 65	± 10	0.7	HB2 , HB3 , HB4	DR_M2F	IDX
BT-ST	12	± 50	± 10	0.5	HB , ST	LINAC/DR_M2F	CAEN
BT-ST	37	± 65	± 10	0.7	ST	LINAC/DR_M2F	IDX

(a) Damping ring power station

(b) the linac klystron gallery
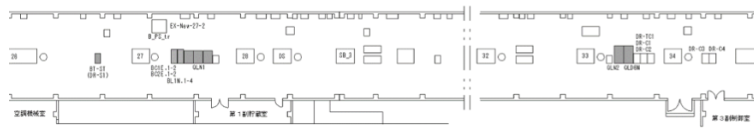
Figure 12.21: The configuration of the power supplies in the power station and the linac klystron gallery.

magnetic measurement systems are shown in Table 12.14 During the measurement, one B2 type and one QD type magnets are measured periodically as a reference to normalize the results against the slow environmental drifts. Since the long flip coil system has enough precision, the harmonic coil system needs the additional tuning to achieve the required performance [16]. To improve the stability, the air bearings are introduced to support the harmonic coil. But the axis of the coil was fixed by the joint of the metal cone structure at the end of the coil and taper hole on the support girder as shown in Fig. 12.23. With this joint, the coil was rigidly fixed with some uncertain random flexibility and this uncertain offset of the axis caused the large fluctuation of the measurement results. By removing this structure as shown in Fig. 12.24, the coil is fixed only by the air bearing support and the fluctuation was reduced by almost one order of magnitude as shown in Fig. 12.25. The fluctuation due to the machining error of the iron core is estimated to about 10^{-3} order and the measurement system has enough resolution to measure these errors.

12.3.3 Control system

As the MR, all the power supplies are controlled through the KEK arcnet interface board. Each power supplies have the location address that was identification of each power supply. The arcnet board has two connectors; one is for the cable from the up-

(a) Long flip coil system for the dipole measurement.

(b) Harmonic coil system for the multipole measurement.
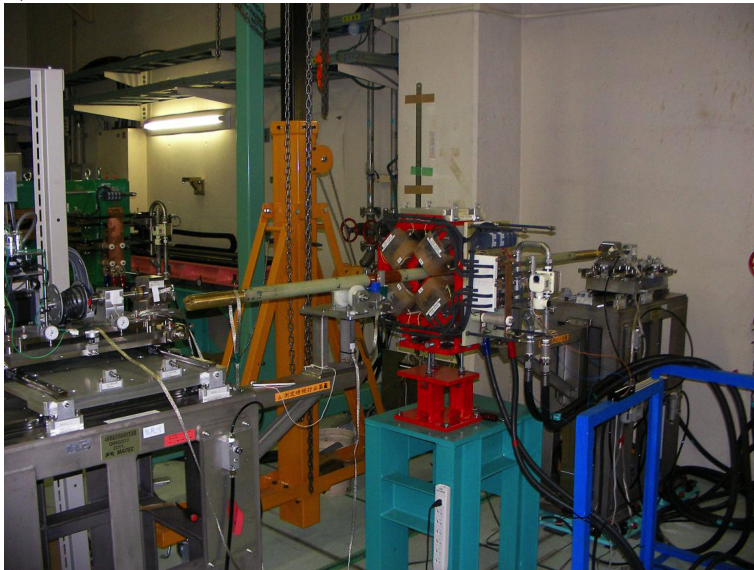
Figure 12.22: Magnet field measurement system.

Table 12.14: Parameters of the magnetic measurement coils.

	Coil Type	Coil turn numbers [Turns]	Coil Full Width [mm]	Coil Length [mm]
Long flip coil	diameter	4	19	1000
Short flip coil	diameter	4	18.1	20
Long harmonic coil 1	radius	1	19	1600
Short harmonic coil 1	radius	1	13	20
Long harmonic coil 2	radius	40	13.5	600
Short harmonic coil 2	radius	200	12	20

(a) Coil side.
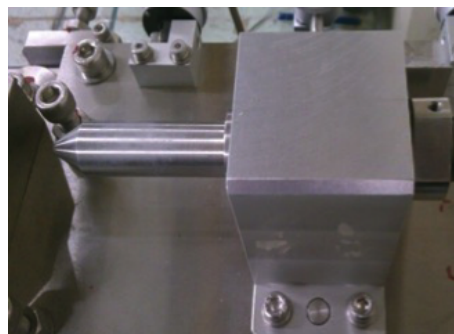
(b)Girder side.

Figure 12.23: Harmonic coil support before the improvement.

(a) Coil side.
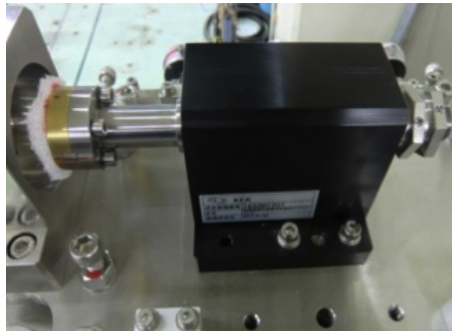
(b)Girder side.

Figure 12.24: Harmonic coil support after the improvement.

stream and the other to the downstream and power supplies are connected as the daisy chain from the VME-arcnet interface board to the small terminator. The arcnet board consists a bit-IO interface to control the power supplies as ON/OFF/RESET, current set and reading the interlock status. The multi-channel relay-switching data acquisition devices (34972A, Keysight) are used for the current monitor. The temperature and water-flow interlocks for the main magnets are read by the PLC (programmable logic controller, F3MA series, Yokogawa) modules. For the software, the EPICS are used.

12.3.4 Excitation curves

By the magnetic field measurement, the excitation curves were measured; the data are the integrated dipole field for the dipoles and the integrated field gradients for the quadrupoles and sextupoles. To calculate the magnetic current from the required field strength, the polynomial fit was introduced as existing KEKB-BT case. The excitation curve was divided into three regions; linear region with dominant iron permeability, saturating region, and almost saturated region with dominant air permeability. To join the polynomial, as well as the values itself, the gradient (first derivative) is made continuous by choosing polynomials as follows;
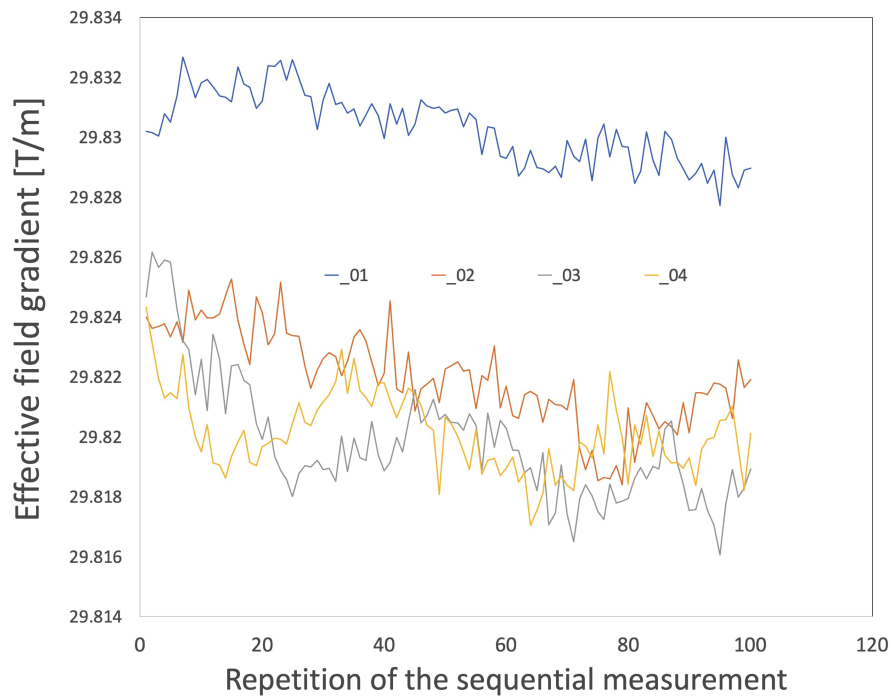
Figure 12.25: Precision of the measurement. The graph shows the effective magnetic field gradient of 400 times measurements with same condition. After every 100 times sequential measurement, the harmonic coil was once removed and fixed again. Before improvement, the fluctuation of these measurements is about 3×10^{-3}. After the improvement, the peak to peak fluctuations is 3.52×10^{-4} in this graph.
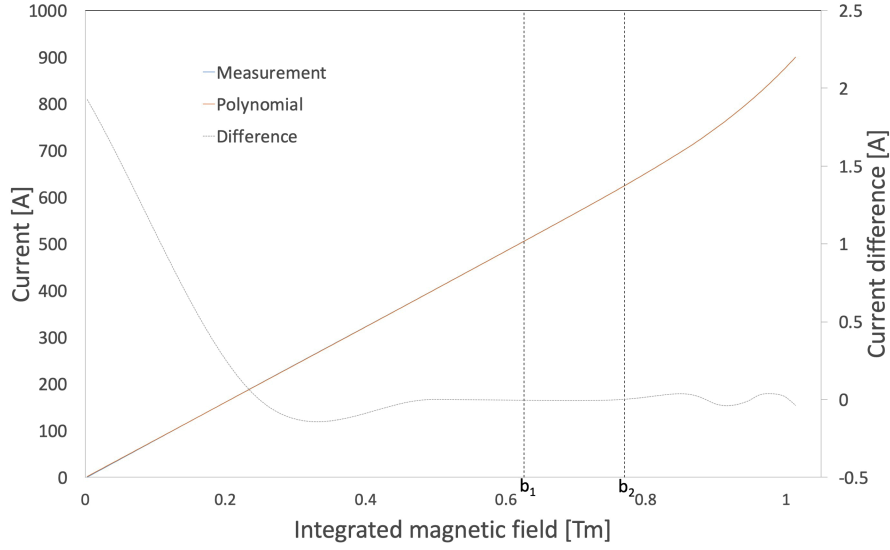
Figure 12.26: Precision of the measurement. Excitation curve of B1 magnet. The averaged measurement results of 33 B1 magnets are used. The coefficients are a_1=804.808, a_2=3.32836, a_3=166.056, a_4=3810.35, b_1=0.625946 and b_2=0.769218. The boundary b_1 and b_2 are shown in dotted vertical line. The operational current is about 802A.

$$\text{I} = a_1 + a_2 x + a_3 x^2 \text{ for } 0 < x < b_1,$$
$$\text{I} = a_1 + a_2 x + a_3 x^2 + a_4(x - b_1)^2 \text{ for } b_1 < x < b_2,$$
$$\text{I} = a_1 + a_2 x + a_3 x^2 + a_4(x - b_1)^2 + a_5(x - b_2)^3 \text{ for } b_2 < x.$$

Here, all a_i and b_i are free parameters. The example of the excitation curve for B1 is shown in Fig. 12.26.

12.4 Vacuum system

12.4.1 Overview

The vacuum system of the damping ring (DR) is divided into five sections (i.e., the east arc section, the west arc section, the north straight section, the south straight section, and the RF section) by gate valves as shown in Fig. 12.27. In the two arc sections, wall on both sides of the beam pipes are irradiated with synchrotron radiation (SR) because a reverse-bend FODO lattice [1] is utilized in the DR. To deal with the SR, beam pipes in the arc sections have antechambers [17] on both sides of the beam channel. The antechamber is effective in reducing the impedance of photon masks placed in the antechambers at the upstream-end of the RF-shielded bellows. The antechambers also play a key role as a countermeasure against electron cloud effects

(ECEs) [18]. To dissipate the heat caused by the SR irradiation, a water cooling system is also required in the arc sections. On the other hand, in the straight sections the antechamber structure and the water cooling system are not required because there is no SR irradiation.
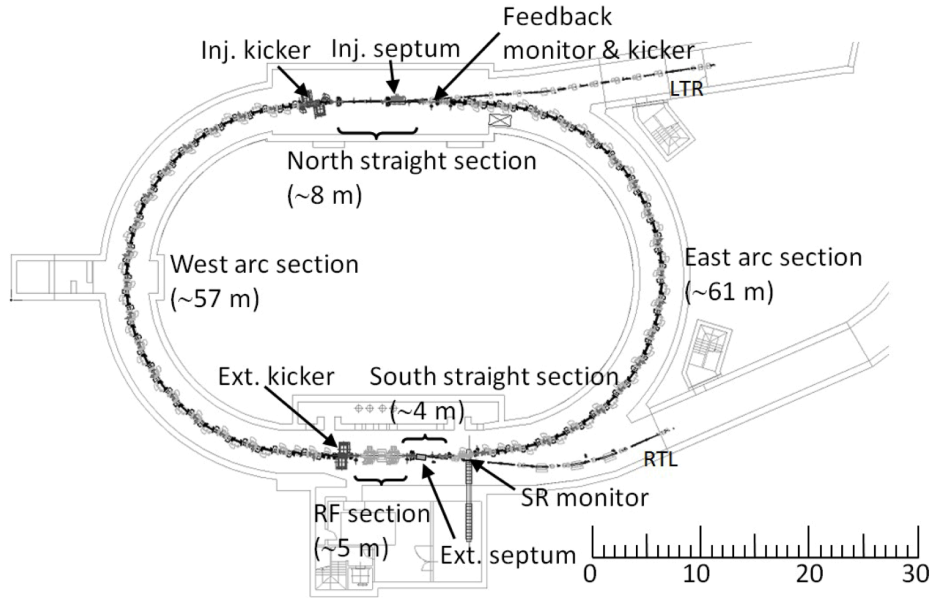
Figure 12.27: The vacuum system of racetrack-shaped positron DR is divided into 5 sections, i.e., the east and west arc sections, the north and south straight sections, and the RF section, by gate valves.

The material used for typical beam pipes is aluminum alloy (extrusion molded pipe: A6063-T6, flange: A2219-T815, pumping port: A5052, block structure for the beam position monitor ports: A5083) in both the arc and straight sections, which is preferred due to its high electrical and thermal conductivity. In addition, the usage of aluminum alloy makes it possible to construct the beam pipe with a grooved structure (see below) through extrusion. The material used for bellows is stainless steel (SUS316L), which has been used in KEKB B-factory for a long period. Non-evaporable getter (NEG) pumps (ST707, SAES Getters Co. Ltd.) are mainly used with auxiliary ion pumps (IPs). The number of beam pipes for the arc sections is 75 and they cover a total length of approximately 120 m. In the straight sections with a total length of approximately 15 m, special components such as RF cavities, septum magnets for beam injection and extraction, are installed. Since a large fraction of the straight sections is occupied by these components, the total length of the regions where simple straight beam pipes are installed is only about 7 m. At transitional regions between the arc and the straight sections, and between certain segments which have a different profile, a few

special beam pipes are installed such that the cross-section of the beam pipe changes smoothly. The cross-sections of main vacuum components are listed in Table 12.15.

A chemical polishing procedure is applied to the beam pipes to remove the first oxide layer (1 μm) and form new oxide layer with much less carbon on the inner surface to reduce the photon stimulated desorption (PSD) rate of carbon oxide and hydrocarbon. To reduce the secondary electron yield (SEY) of the inner surfaces of the beam pipes, the beam pipes are coated with titanium nitride (TiN) film.

Table 12.15: Cross-sections of main vacuum components.

Vacuum component	Cross-section		Location
Beam pipes for RF section	Circular	ϕ150 mm	RF section
Feedback kicker	Octagonal	62.8 mm (face-to-face)	East arc section
Feedback monitor	Octagonal	46 mm (face-to-face)	East arc section
Inj. and Ext. kicker	Rectangular	42 mm(H) ×37 mm(V)	West arc section
Inj. and Ext. septum	Circular	ϕ41.2 mm	North (Inj.) and South (Ext.) straight sections
Beam pipes for injection	Rectangular	46 mm(V) ×104 mm(H) ∼46 mm(V) × 46 mm(H)	North straight sections
Beam pipes for adjacent area of the east arc section, etc.	Octagonal	46 mm (face-to-face)	East arc, North and South straight sections
Beam pipes for the arc sections	Octagonal with antechambers	height 24 mm, width 90 mm	East and West arc sections

12.4.2   Beam Pipes

Beam pipes for arc sections

Structures

Each cell of the reversed-bend FODO lattice in the arc sections consists of six magnets (2 dipole, 2 quadrupole, and 2 sextupole). Further, there are two types of dipole magnets with different lengths, bending directions and curvatures, and two types of beam pipes (Type I and Type II) corresponding to each dipole magnet. Each beam pipe covers one dipole, one quadrupole, and one sextupole magnet. Figure 12.28 and 12.29 respectively show the beam pipes of the arc sections and the layout of the beam pipes in one cell. The area available for the beam pipes is very less owing to the closely located magnets, and hence, the beam pipes are designed to fit the narrow spaces. Each beam pipe consists of a bent part placed in the dipole magnet and a straight part. The curvature radius of the bent part (Type I: 2684 mm, Type II: 2966 mm) is the same as that of the corresponding dipole magnet. The material of the beam pipe is aluminum alloy, except for the bellows, which are stainless steel, as described before. The profile of the beam pipe is formed by extrusion. To construct the bent part, the extrusion-molded pipe was bent with the curvature radius of the dipole magnet by using a three-point bending method at room temperature.

Since a beam position monitor (BPM) and pumps are coupled to the beam pipes, the beam pipes have block-like structure for the BPM ports (BPM block) and pumping ports. The RF-shielded bellows [19] are connected to the beam pipe by welding, because there is no room for the installation of isolated bellows chambers. Space saving can be achieved when special ConFlat (CF) flanges (ICF152) are used with RF contacts for connecting each other. The BMP block, the pumping port, the RF shielded bellows, and the special connection flanges are described in detail in following sections.

Cross-section

Typical cross-section of the beam pipes in the arc sections is shown in Fig. 12.30. In the arc sections, the beam pipes have antechambers on both sides of the beam channel because SR is irradiated on both side surfaces of the beam pipe. The antechamber can reduce the impedance of the SR masks by keeping them away from the beam. It also prevents the invasion of photoelectrons, which can cause electron clouds, into the beam channel. The height of the beam channel is set to 24 mm in order to suppress the coherent synchrotron radiation effects [20].

Figure 12.31 shows the photon-reduction rate of the beam pipes as a function of antechamber height, for each instant of storage time. It is estimated by the following
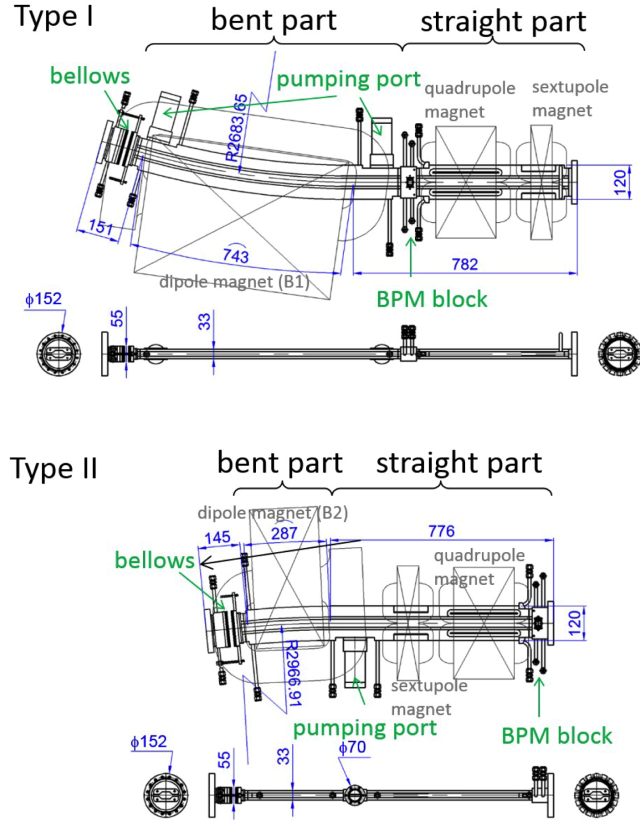
Figure 12.28: Two types of beam pipes (Type I and Type II) for the arc sections.

formula,

$$1 - \left(1 - \frac{N_{E\min}}{N_{\text{total}}}\right) \times \left(1 - \frac{N_{\text{ante}}}{N_{\text{total}}}\right) \tag{12.10}$$

where N_{total} [s^{-1}] is the number of photons emitted in the ring per second, $N_{E\min}$ [s^{-1}] the number of emitted photons with an energy level less than $E_{\min}$ [eV], and N_{ante} [s^{-1}] is the number of photons irradiating the antechamber. $E_{\min}$ is the minimum photon energy required to produce photoelectrons, which cause electron clouds. Since (1 - $N_{\text{ante}}/N_{\text{total}}$) is the ratio of the number of photons which irradiate the antechamber exterior and (1 - $N_{E\min}/N_{\text{total}}$) is the ratio of the number of photons which energies higher than $E_{\min}$, the photon-reduction rate indicates the ratio of number of photons irradiated into the antechamber or irradiated to the antechamber exterior with insufficient energy to produce photoelectrons to the total number of photons. N_{total} can be given by

$$N_{\text{total}} = 8.08 \times 10^{20} E I \frac{\Theta}{2\pi} \tag{12.11}$$
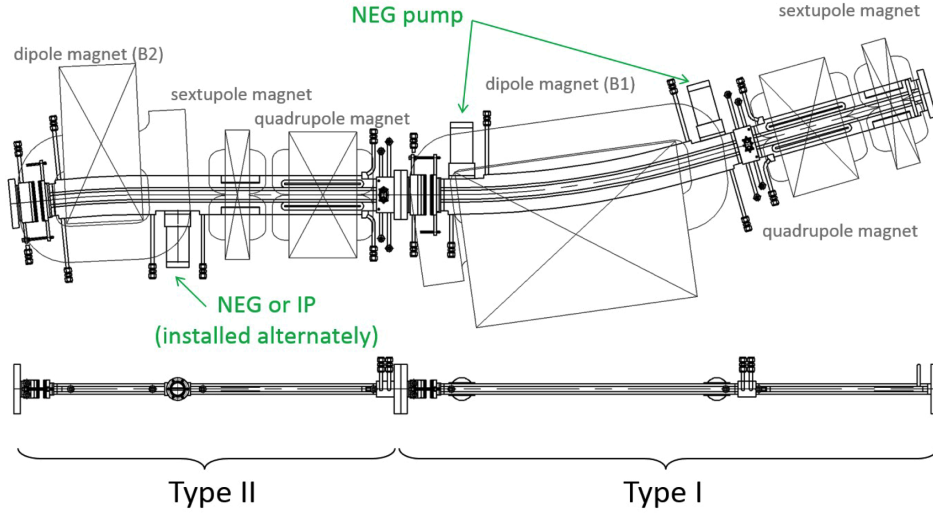
Figure 12.29: Two beam pipes installed in one cell which consists of 6 magnets.

where E [GeV] is the beam energy, I [A] is the beam current, and Θ [rad] is the total bending angle of the ring [21]. $N_{E\text{min}}$ is given by

$$N_{E\text{min}} = 0.19 N_{\text{total}} \int_0^{E\text{min}} \int_{\varepsilon/\varepsilon_c}^{\infty} K_{5/3}(\eta) d\eta d\varepsilon \tag{12.12}$$

where $K_{5/3}$ is the modified Bessel function, ε [eV] is the photon energy, and ε_c [eV] is the critical energy of the SR [21], which is the energy at which half of the total power has been emitted. To calculate N_{ante} the distribution of photons in the vertical angle $dN(\theta)$ [s^{-1}] is given by

$$dN(\theta) = \frac{3}{5\pi} N_{\text{total}} \frac{1 + \frac{3}{2}x^2}{(1 + x^2)^2} dx \tag{12.13}$$

where

$$x = \gamma\theta \tag{12.14}$$

where γ is Lorentz factor and θ [rad] is the vertical angle [22]. In this work, it was assumed that E_{min} is 5 eV ($N_{E\text{min}}/N_{\text{total}} \approx 0.16$) and the shape of a bunch of beams is Gaussian in the vertical direction. Irradiation distance is assumed to be 1 m because approximately 90 % of photons enter the antechamber within 1 m, and therefore, N_{ante} is can be given by
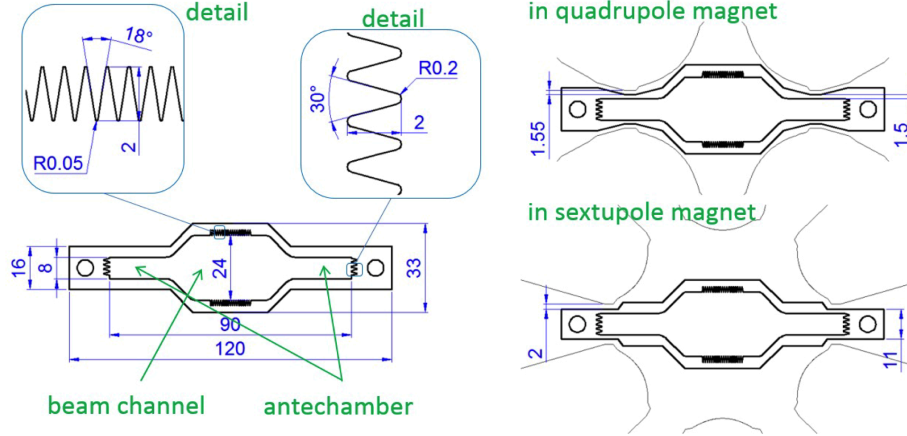
Figure 12.30: Typical cross-section of the beam pipes in the arc sections. The beam pipes have antechambers with height 8 mm on both sides of the beam channel. They have grooved structures at the top and bottom of the beam channel to reduce the secondary electron yield, and at the side wall of the antechambers for the antireflections of the SR.

$$N_{\text{ante}} = \int_{-\theta_{\text{ante}}}^{\theta_{\text{ante}}} dN(\theta) \tag{12.15}$$

where

$$\tan\theta_{\text{ante}} = \frac{h}{1000\,\text{mm}}. \tag{12.16}$$

Here, h [mm] is the height of the antechamber. The vertical size of the bunch σ_y [mm] decreases with increasing storage time, and therefore, the photon-reduction rate increases with the storage time. If the height of the antechamber is 8 mm, which is the maximum value in this case due to the gap between the magnetic pole faces, over 90 % of the photons are irradiated in the antechamber after 20 ms of beam storage. This result shows that an antechamber with a height of 8 mm is enough to reduce the effect of photoelectrons, and this value is adopted in the arc sections. In the quadrupole and sextupole magnets, the outer part of the beam pipe is trimmed to avoid interference in the magnetic poles, as shown in Fig. 12.30.

The inner width of the beam pipe, including the antechambers, is 90 mm, which is also limited by the aperture of the magnets. The side wall of the antechamber has a grooved structure (of depth 2 mm, and angle 30°, and roundness of the top and valley
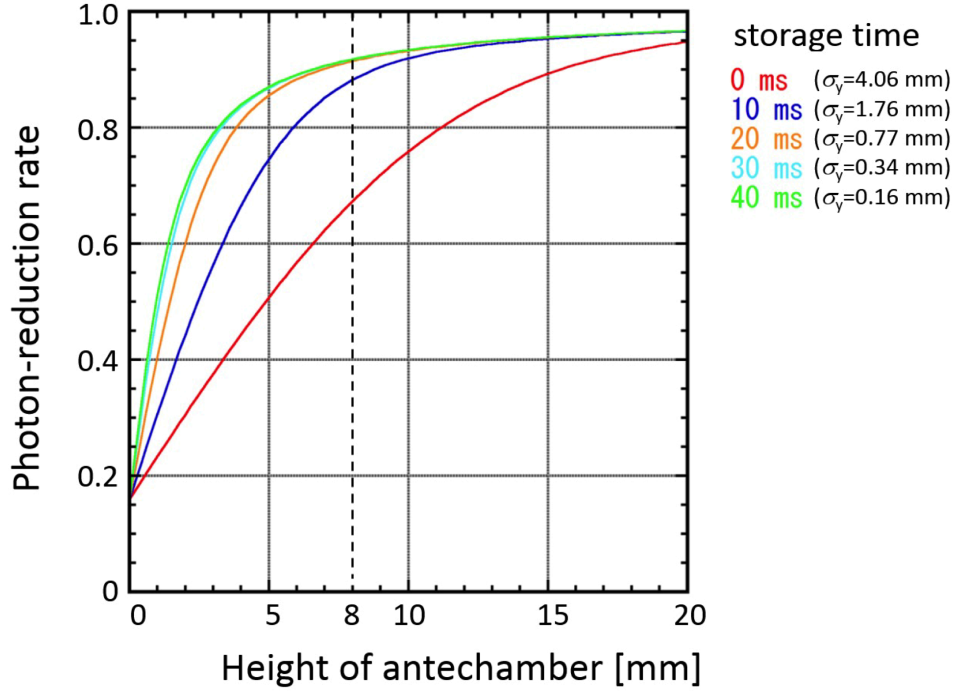
Figure 12.31: Variation of photon-reduction rate with antechamber height for different vertical beam size at different durations of storage time.

0.2) to ensure antireflection of the SR. To check the effect of the antireflection of this grooved structure, the distributions of the reflected photons were roughly estimated by using Synrad3D simulation code [23] with a simplified model of the beam pipe. Compared to the antechamber without grooved structure, the ratio of the number of reflected photons that irradiate the beam channel to the total number of photons reflected on the side wall is expected to reduce to about 1/8 by adopting this grooved structure. As an additional countermeasure against ECEs, the beam pipes in the arc sections have a grooved structure at the top and bottom of the beam channel to reduce the SEY [24]. Though the grooved structure is effective mainly in a dipole field [24] and is required only in the bent part, it is also present in the straight part. This is because the grooved structure is formed by the aluminum extrusion of the pipe profile. The depth of this groove is 2 mm and the roundness of the top and valley is 0.05. the angle of the groove is 18°, while the width of the grooved area is approximately 15 mm.

Connection flange

In the arc sections, the coils of the magnets are very close to the flanges for connecting the beam pipes to each other and the space around the flange is very tight. Since it

is impossible to achieve enough room for bolt installation in the normal fashion, special CF flanges (ICF152) with an RF contact are used for the beam-pipe connection to save some space. The connection flanges in the arc section are shown in Fig. 12.32. The material of the flange is aluminum alloy (A2219-T851). The knife-edge for vacuum sealing is hardened by the CrN film coated by an ion-plating method, and aluminum CF gaskets are used for vacuum sealing. To make shorter bolts available for the flange connection, one flange (Type B) has tapped holes and the other flange paired with it (Type A) has horseshoe-shaped bolt holes to install the bolts from the side.
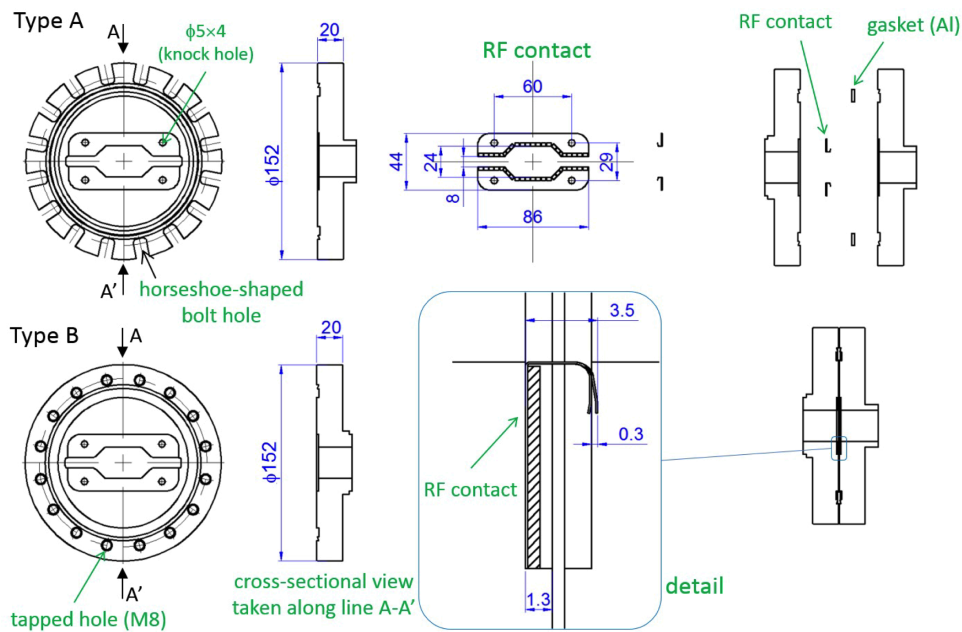
Figure 12.32: One set of spacial ConFlat flanges used for beam pipe connection in the arc sections for space saving.

To hide gap between the flanges from the beam, the RF contacts are installed on all flange connections. Figure 12.32 also shows the RF contact in the arc section. This RF contact is made of beryllium-copper and is fixed on the flange through knock-pins.

BPM block

There are two types of BPM blocks in the arc sections: one (Type A), integrated with the connection flange for space conservation for the Type II beam pipe and the other (Type B), a stand-alone type for the Type I beam pipe. Figure 12.33 shows the schematic drawing of two types of BPM blocks. A BPM block has four holes for button electrodes, two of which are on the top and two of which are at the undersides of the beam channel. Two button electrodes mounted on one racetrack-shaped flange [25]

are assembled on each side. Helicoflex Delta is used for the vacuum seal of the flange-mounted button electrode. The depth of the groove for the vacuum seal is optimized to obtain an accurate position of the electrode with minimum bolt-tightening torque for the protection of tapped holes on the aluminum body. To establish the position of the BPMs relative to the quadrupole magnets, the underside of the BPM block is bolted onto a support, which is fixed to the quadrupole magnet as shown in Fig. 12.34. On the top side, there are knock-pin holes for mounting measurement devices such as inclinometers.
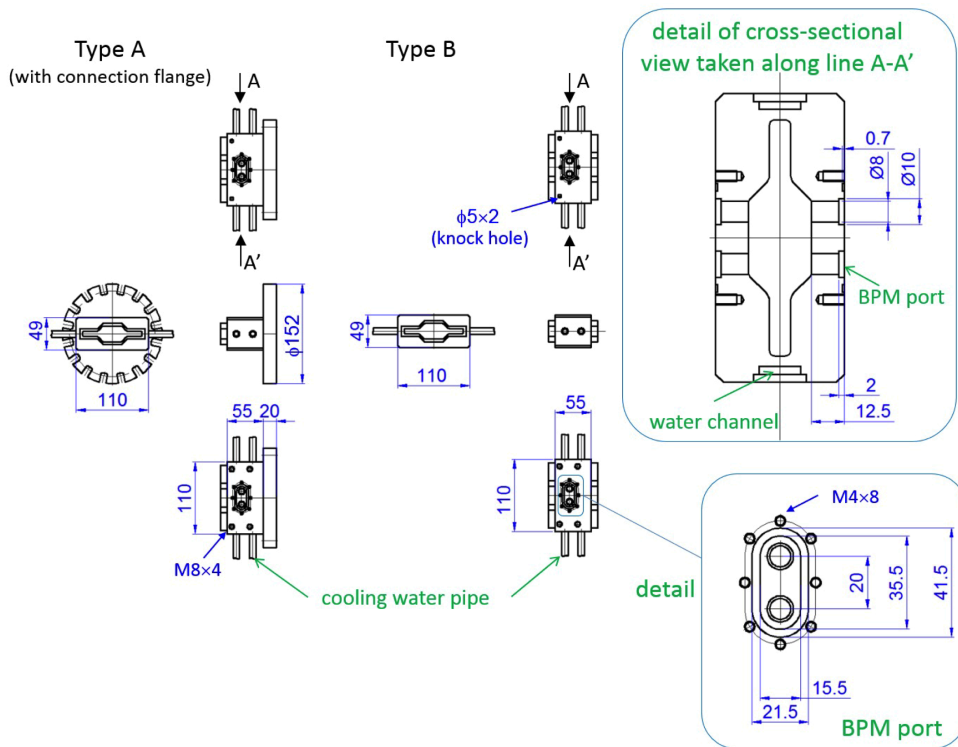
Figure 12.33: Two types of the BPM blocks for the arc sections.

The BPM block is made of aluminum alloy material (A5083), and it is connected to the beam pipe or connection flange through TIG or electron beam welding, respectively.

Bellows

The beam pipes in the arc sections have bellows structures at one end. The bellows in the arc sections are shown in Fig. 12.35. Because the bellows are located in the gap of the dipole magnet coils for space saving and their height is limited to less than 56 mm, a racetrack-shaped bellows structure with a height of 55 mm is adopted. The bellows have a finger-type RF shield that consists of contact fingers, spring fingers, and an inner tube[4]. The strength of the contact force is approximately 1 N/finger, and
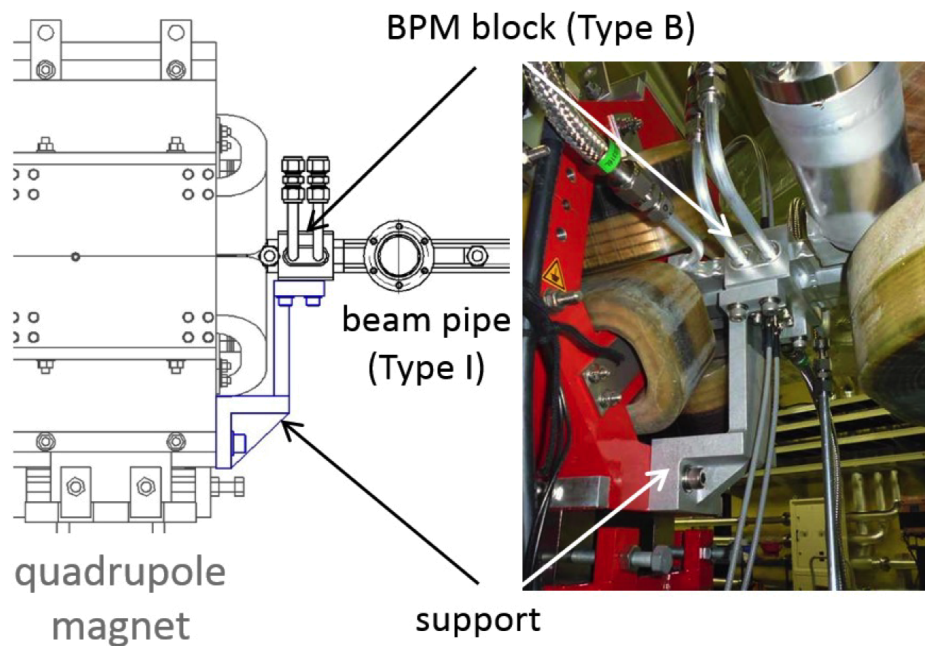
Figure 12.34: The BPM blocks are bolted onto a support fiexed to the quadrupole magnets.

the stroke width of the bellows is 4 mm. To protect the RF shield against direct SR irradiation, SR masks with a height of about 8 mm are located in the antechambers, at the upstream-end of the RF shield.

The contact finger, spring finger, and the inner tube are made of beryllium-copper (C1720), silver-plated Inconel, and silver-plated stainless steel (SUS316L), respectively; while the bellows are made of stainless steel (SUS316L). A bimetallic joint, produced via hot isostatic pressing (HIP), is used between the bellows and the aluminum alloy beam pipe and flange.

Pumping port

The beam pipes in the arc sections have pumping ports on the sides of the antechambers. There is no RF shield between the beam pipes (antechambers) and pumping ports because the pumping ports are located in the depths of the antechambers far from the beam. The pumping ports have CF flanges (ICF70) for mounting the pumps. NEG pumps (C50-ST707 with GP 50 MK2-C, SAES Getters) with pumping speed just after activation approximately equal to 0.20 m^3s^{-1} for H_2, and 0.10 m^3s^{-1} for CO, and IPs with a pumping speed of 0.035 m^3s^{-1} for both H_2 and CO are mounted on it as main and sub-pumps, respectively. A roughing pump unit consisting of a turbomolecular pump and a dry scroll pump is also connected to this pumping port, via a manifold
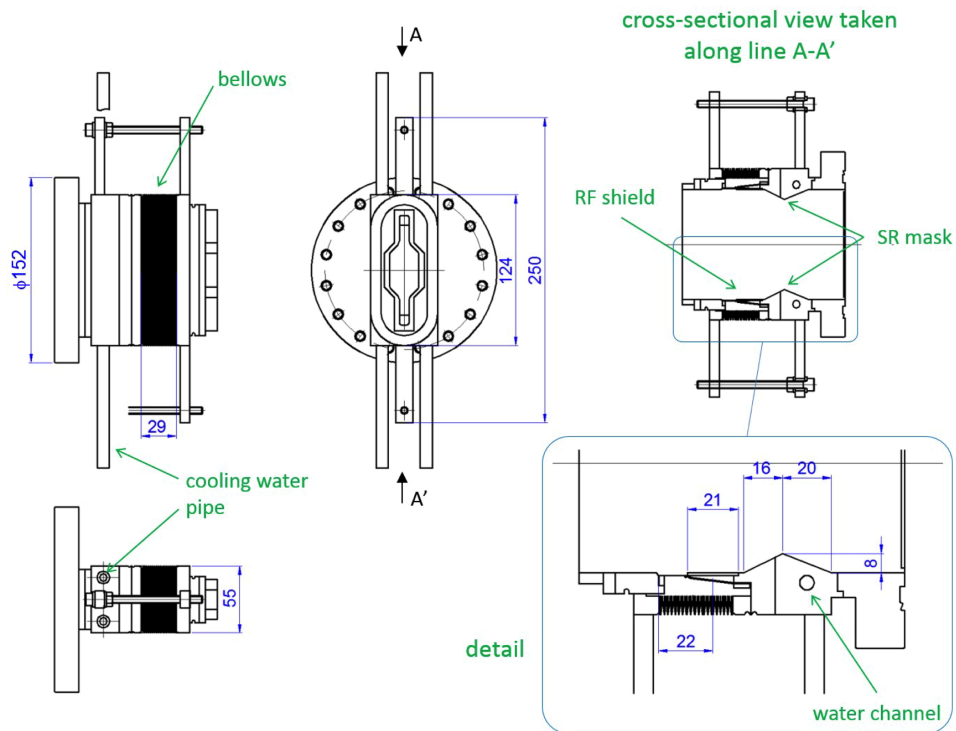
Figure 12.35: The RF-shielded bellows at one end of the beam pipe. A racetrack-shaped bellows is adopted since the bellows is located in the gap of the dipole magnet coils.

and an angle valve.

The conductance of the pumping port for the NEG pump is estimated to be 0.016 m^3s^{-1} and the effective pumping speed of the NEG pump just after activation for CO is 0.014 m^3s^{-1}. Since the IP is connected to the pumping port via the manifold, the conductance of the pumping port for the IP is less than that for the NEG pump (0.012 m^3s^{-1}). The effective pumping speed of the IP is 0.008 m^3s^{-1}.

In the arc sections, five NEG pumps and one IP are installed in two cells. Two NEG pumps are installed in the Type I beam pipe, and one NEG pump or IP is installed alternately in the Type II beam pipe as shown in Fig. 12.29. The average distance between the pumps is approximately 1 m. The average effective pumping speed S_{eff_avg} [m^3s^{-1}] therefore becomes 0.013 m^3s^{-1} (= (5 × 0.014 m^3s^{-1} + 1 × 0.008 m^3s^{-1}) / 6), immediately after NEG activation. A 50% reduction in the pumping speed of the NEG pump (to 0.05 m^3s^{-1}) will have a negligible effect on the average effective pumping speed, which will then be approximately 0.012 m^3s^{-1}.

Beam pipes for straight sections

Structures

In the straight sections of length 15 m, special components such as RF cavities, and beam pipes for the beam injection and extraction, are installed. The cross-sections of these special components are of circular, rectangular, and square shapes. In other regions in the straight sections (7 m), simple straight beam pipes are installed. In these straight sections, it is not necessary to have the antechamber and water cooling. The beam pipes are made of the same type of aluminum alloy as that of the arc sections. Figure 12.36 shows an example of a beam pipe for the straight sections. The beam pipes installed in a quadrupole magnet have BPM ports (BPM block).
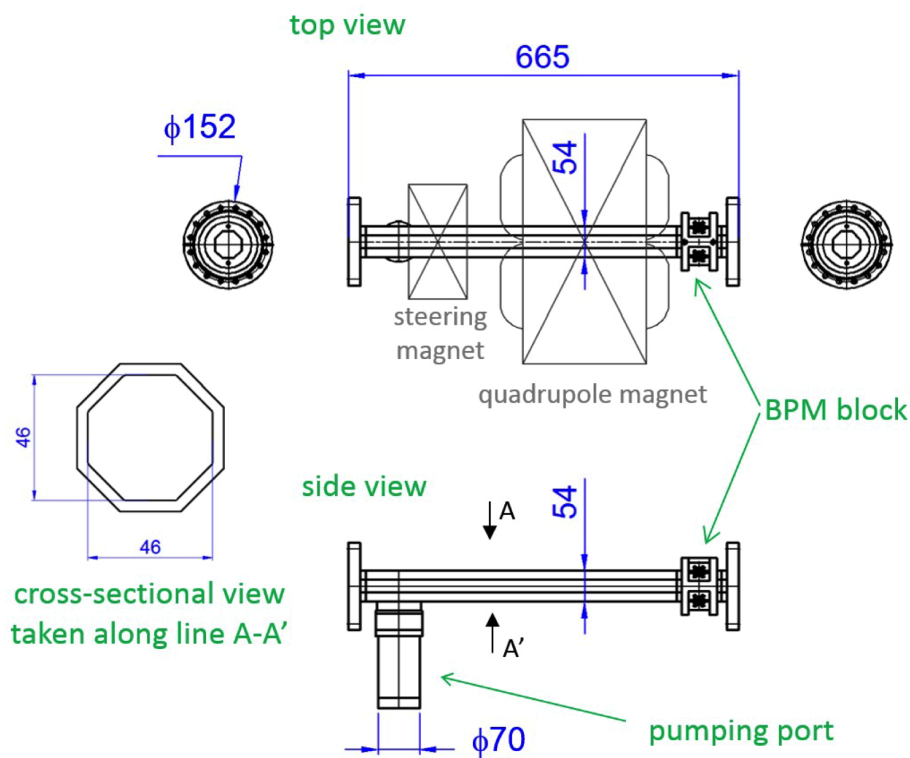
Figure 12.36: Octagonal beam pipe for the straight sections. The distance between the two faces of the cross-section is 46 mm in this case. The beam pipes in the straight sections are simpler than those in the arc sections.

Cross-section

The standard cross-section used in the straight sections is depicted in Fig. 12.36. In addition to a simple octagonal cross-section, there are several cross-sectional shapes in the straight section as listed in Table 12.15. In the transition regions between

components with different cross-sections, special beam pipes are installed in order to change the cross-sections smoothly.

Connection flange

In the straight sections, aluminum CF flanges (ICF152 and ICF114) are adopted. They do not have horseshoe-shaped bolt holes as in the arc sections, because there is enough room for bolt installation in the normal fashion. To hide the gap between the flanges from the beam, RF contacts are installed on all the flange connections.

BPM block

A typical BPM block for the straight sections with an octagonal cross-section is shown in Fig. 12.37. The aperture of the BPM block is same as that of the beam pipe to be connected. Four flange-mounted button electrodes, which are same as those used in the SuperKEKB LER [26], are assembled on it. The BPM block is TIG welded to the beam pipes and is mounted on a support fixed to the quadrupole magnet.
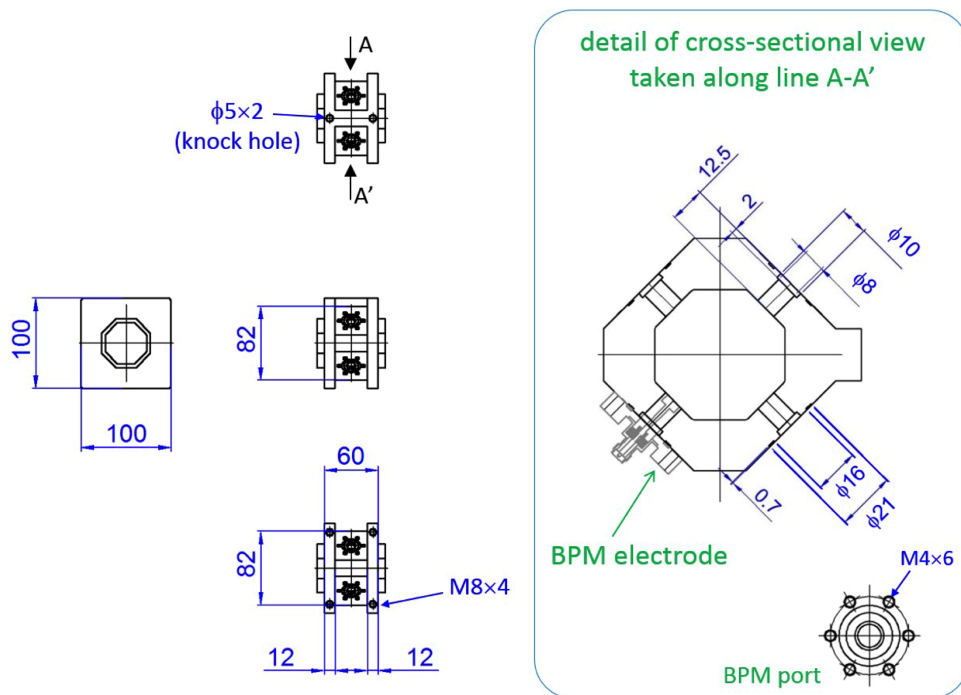
Figure 12.37: The BPM block for the straight sections. Four flange-mounted button electrodes are assembled on it.

Bellows

There is enough room for the installation of isolated bellows chamber that is connected to the beam pipe via flanges. Therefore, the isolated bellows chamber is used

in the straight sections and no bellows is connected to the beam pipe by welding. A typical bellows chamber for the straight sections is shown in Fig. 12.38. The bellows is circular and has a finger-type RF shield. Since they are installed in locations where intense SR does not hit the RF shield directly, they have no SR masks in it. The bellows and flanges are both made of stainless steel (SUS316L), and hence, a bimetallic joint used in the arc sections is not necessary. The cross-sections of the bellows chambers in the straight sections are of octagonal, rectangular, and square shapes, which are made to conform to the adjoining beam pipes.
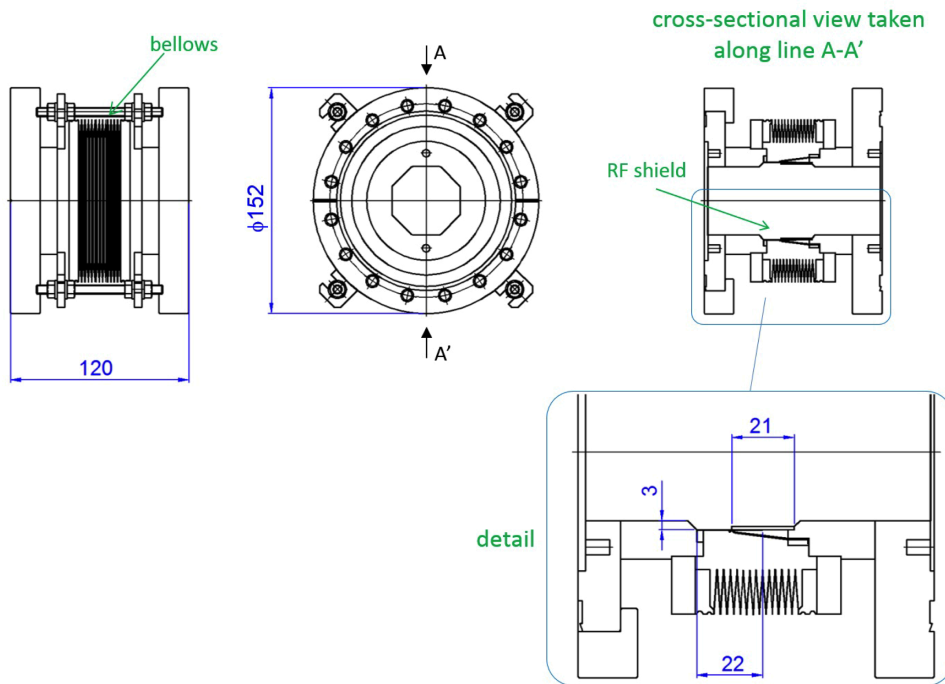
Figure 12.38: Isolated bellows chambers with circular bellows are used in the straight sections. They also have finger-type RF shield in it.

Pumping port

In the straight sections, the pumping ports are placed at the bottom or sides of the beam channel, as shown in Fig. 12.36. There is a screen with many holes for the RF shield between the beam pipe and the pumping port. The typical diameter of the hole is 3 mm, which is equal to the thickness of the screen. The conductance of the RF screen is designed to be at least 0.02 m^3s^{-1}. Hence, the effective pumping speed immediately after activation is estimated to be higher than 0.016 m^3s^{-1} (for CO).

12.4.3 Beam Lifetime

The beam lifetime in the DR mainly determined by the beam-residual gas interactions such as (i) an elastic scattering on nuclei of the residual gas (Rutherford scattering), (ii) an elastic scattering on electrons of the residual gas (Møller), and (iii) an inelastic scattering on nuclei of the residual gas (Bremsstrahlung). The total lifetime determined by the beam-residual gas interactions can be obtained by

$$1/\tau = 1/\tau_R + 1/\tau_M + 1/\tau_B = Nv(\sigma_R + \sigma_M + \sigma_B) \tag{12.17}$$

where τ_R, τ_M and τ_B are beam lifetime determined by Rutherford scattering, Møller scattering, and Bremsstrahlung, respectively, N the density of the residual gas, v the velocity of the positron, σ_R, σ_M and σ_B the cross sections for Rutherford scattering, Møller scattering, and Bremsstrahlung, respectively. Each cross section is calculated using following equations [27]:

$$\sigma_R = \frac{4r_e^2 Z^2}{\gamma^2} \frac{\pi}{2} \left(\frac{<\beta>}{a} \right)^2, \tag{12.18}$$

$$\sigma_M = \frac{2\pi r_e^2 Z}{\gamma} \frac{1}{\varepsilon_{RF}}, \tag{12.19}$$

$$\sigma_B = \frac{4r_e^2 Z^2}{137} \frac{4}{3} \ln \frac{183}{Z^{1/3}} \left(\ln \frac{1}{\varepsilon_{RF}} - \frac{5}{8} \right), \tag{12.20}$$

where r_e is the classical electron radius, γ the relativistic γ-factor, Z the atomic number for residual gas components, $<\beta>$ the average β-function, a the half chamber aperture, the longitudinal acceptance (i.e., RF bucket height). For the DR, $<\beta>$ and a for the arc sections are 6 m and 12 mm, respectively, and ε_{RF} is 0.015.

Figure 12.39 shows the theoretical expectation of τ, τ_R, τ_M and τ_B obtained by Eqs. 12.17-12.20 as a function of the pressure. Here, the residual gas is assumed to be composed of only CO. Since the beam lifetime determined by interactions with H_2 is much longer than that with CO, the contribution to the beam lifetime by H_2 is negligible small in the DR. The greatest contribution to the beam lifetime is Bremsstrahlung, and second one is Rutherford scattering. There is extremely small contribution of Møller scattering.

The required beam lifetime due to residual gas scattering is to be longer than 1000 s. As mentioned below, PSD by the SR is the major dynamic gas load during beam
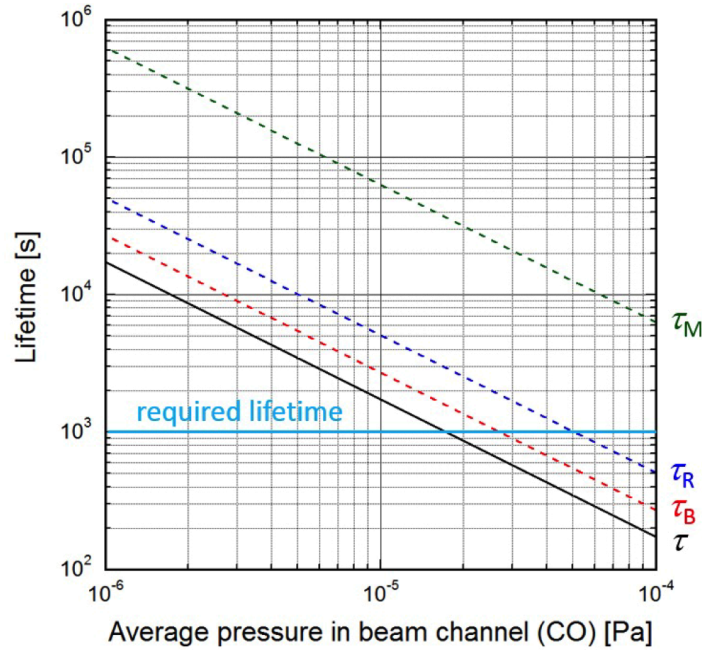
Figure 12.39: Expected beam lifetime as a function of the average pressure of CO in the beam channel, calculated by theoretical equations. τ_R, τ_M and τ_B are beam lifetime determined by Rutherford scattering, Møller scattering, and Bremsstrahlung, respectively, and τ is total beam lifetime.

operation, and the main outgassing components is expected to be H_2, CO and CH_4 during beam operation. The most important component among them is CO, because the beam lifetime is determined mainly by scattering with CO due to its heavy Z.

From the theoretical expectation of the beam lifetime shown in Fig. 12.39, CO pressure in the beam channel should be less than $\sim 1.7 \times 10^{-5}$ Pa to obtain a beam lifetime longer than target value (1000 s).

12.4.4 Average Pressure Estimation

Simulation model for pressure distribution calculation

The pressure distribution along the beam pipe and the average pressure in the arc sections are estimated by using the Molflow+ [28] varying PSD rate η [molecules photon^{-1}], pumping speed, and stored beam current I [mA] (i.e., bunch charge and number of bunches). The three-dimensional model of the beam pipe used for Molflow+ analysis is shown in Fig. 12.40. It consists of one Type I beam pipe and one Type II beam pipe with three pumping ports and one manifold. It has no bellows parts, no BPM blocks,

and no grooved structure. Bent parts are modeled as straight parts for simplicity. In the following calculation, it is assumed that only one kind of gas (H_2 or CO) desorbs from the wall. For H_2, pumping speed of the NEG pumps (S_{NEG}) for the Type I is 0.200 m^3s^{-1}, or 0.100 m^3s^{-1} as reference, and pumping speed of the IP (S_{IP}) at the manifold connected to the Type II is 0.035 m^3s^{-1}. On the other hand, For CO, S_{NEG} is 0.100 m^3s^{-1}, which is pumping speed of NEG immediately after the activation, or 0.050 m^3s^{-1} considering saturation of NEG, and S_{IP} is 0.035 m^3s^{-1}. Temperature is 25°C for both gases.
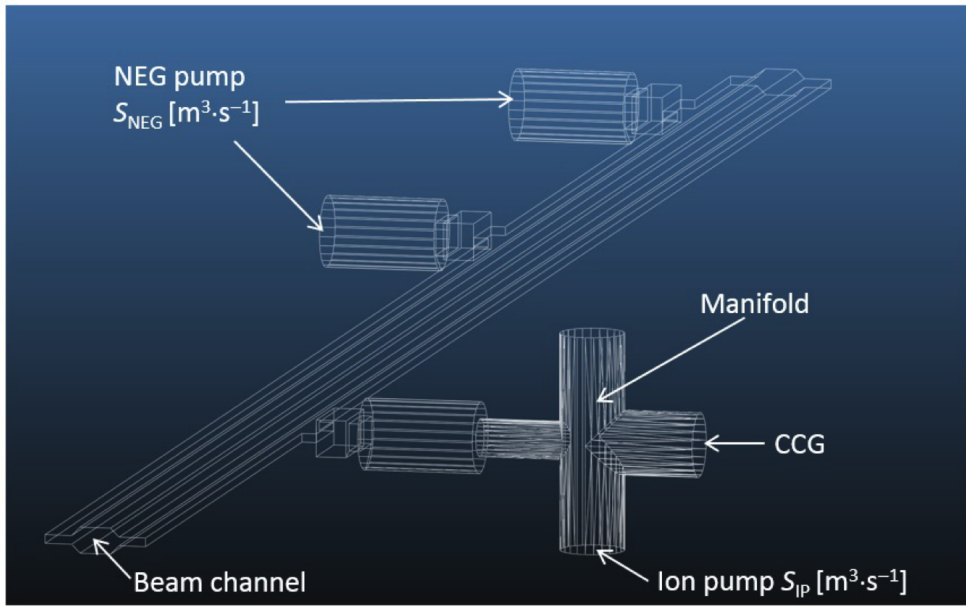
Figure 12.40: 3D model of the beam pipe for the arc sections used for Molflow+ analysis.

For the calculation of the pressure distribution with beam, it is assumed that the SR irradiates both sides of the antechambers evenly. Average linear photon density per unit stored beam current is approximately 1.5×10^{16} photons $s^{-1}m^{-1}mA^{-1}$. By assuming both η and stored beam current I, outgassing rate per unit length from the SR irradiated surface Q [$Pa\,m^3s^{-1}m^{-1}$] is obtained by $Q = 1.5 \times 10^{16} \times I \times \eta \times k \times T$, where k [JK^{-1}] is Boltzmann constant and T [K] is temperature. For the calculation of the base pressure without beam, no SR irradiates the beam chamber (i.e., $\eta = 0$).

Base pressure estimation

In order to estimate the base pressure without beam, the pressure distribution in the beam pipe was calculated varying the thermal gas desorption rate. Since the main

residual gas component without stored beam is expected to be H_2, the pressure of gas composed only of H_2 was calculated here.

The pressure at the CCG ($p_{CCG}(H_2)$) and the average pressure in the beam channel ($p_{BC}(H_2)$) calculated by Molflow+ are summarized in Table 12.16. In this table, N_2-equivalent value of $p_{CCG}(H_2)$, which is obtained by multiplying $p_{CCG}(H_2)$ by the relative sensitivity for H_2 of the N_2-calibrated CCG ($S_{H2}/S_{N2} = 0.44$), are also listed. Even if S_{NEG} dropped to half, the amount of pressure increase in the beam pipes and manifold is small. This is because the conductance between the NEG port and the beam channel is so small (0.02 m^3s^{-1}) that the effective pumping speed of the NEG hardly changes even if S_{NEG} drops to half. The $p_{BC}(H_2)$ values are slightly higher than the $p_{CCG}(H_2)$ values, which is 1.1~1.3 times.

Since it is expected that the thermal gas desorption rate of H_2 decreases to less than 5×10^{-8} Pa $m^3s^{-1}m^{-2}$ before the commence of the first commissioning, the base pressure in the beam channel without the beam will be less than 3×10^{-7} Pa. On the other hand, since CO partial pressure is expected to be much lower than H_2 partial pressure in typical beam pipes without beam, its value will be less than $\sim 1\times10^{-8}$ Pa. Meanwhile, the reading value of the CCG, which is in N_2 equivalent, will be less than 1.3×10^{-7} Pa.

Pressure estimation with beam

The pressure distribution for CO in the beam pipes was also calculated varying η of the SR irradiated surfaces, which can be easily converted to the outgassing rate Q if the beam current was determined. Figure 12.41 shows average CO pressure in the beam channel calculated by Molflow+ ($p_{BC}(CO)$) for the stored beam currents of 5.0 mA, 10.0 mA, 40.0 mA, and 70.0 mA, respectively, as a function of assumed η. When the stored beam current is 5.0 mA, the slope of $p_{BC}(CO)$ slightly decreases at low η. This is because the contribution of thermal gas desorption is not negligible small at low pressure region. In other cases, thermal gas desorption has only a little effect on the pressure during beam operation and the PSD by the SR is the major dynamic gas load during beam operation.

Vacuum scrubbing strategy

At the early stage of commissioning, the number of bunch and bunch charge will be less than 4 and 2 nC, respectively, and hence the stored beam current will less than 17.7 mA. Although the DR will be operated with a small stored beam current, it is expected
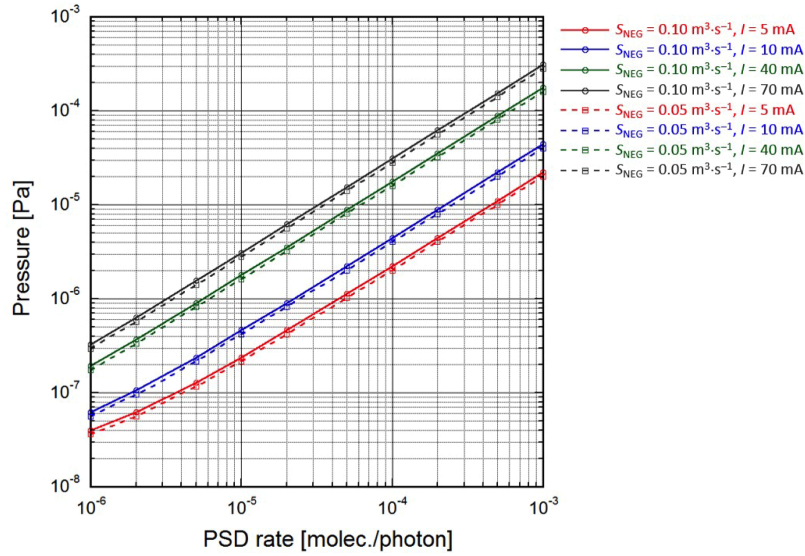
Figure 12.41: Average pressure of CO in the beam channel calculated by Molflow+ for different stored beam currents (5.0 mA, 10.0 mA, 40.0 mA, and 70.0 mA) as a function of assumed PSD rate η.

that it will be difficult to obtain a sufficiently long beam lifetime at the early stage. For example, when the stored beam current is 10.0 mA and η is 1×10^{-3} molecules photon^{-1}, the average CO pressure in the beam channel is approximately 4×10^{-5} Pa, which is higher than the pressure required for target beam lifetime (1.7×10^{-5} Pa). However, if η is reduced to 1×10^{-4} molecules photon^{-1} by SR irradiation (i.e., vacuum scrubbing), the average pressure will approach 4×10^{-6} Pa even after the average pumping speed reduced to 0.05 m^{3}s^{-1}. In order to obtain the target beam lifetime with design beam current ($\sim$70 mA), it is expected that the vacuum scrubbing have to further proceed until η decreases to approximately 4×10^{-5} molecules photon^{-1}.

If the pressure is 1×10^{-5} Pa, the average effective pumping speed will reduce to 0.01 m^{3}s^{-1} after about 10-days of beam operation, due to the saturation of the NEG pumps. At early stage of the commissioning, therefore, a frequent activation of the NEG pumps will be required. However, as the scrubbing process progresses, the required pumping speed to maintain low pressure will reduce, and the intervals between the activations of the NEG pumps can be made longer. To avoid frequent NEG activations, the stored beam current must be increased gradually by increasing the scrubbing time. If η reaches 1×10^{-5} molecules photon^{-1}, which is expected to require $\sim$15 Ah, and the stored beam current is 10 mA, the average effective pumping speed needed to achieve the average pressure of 1×10^{-5} Pa is 0.004 m^{3}s^{-1}. In this case, the interval of the activation of the NEG pump is about 300 days, and NEG activation can be performed during the long

shutdown times scheduled in summer.

Meanwhile, in the straight sections, the pressure will be lower than that in the arc sections. In the adjacent regions of the RF section, additional pumps are installed in order to achieve pressures in the order of 10^{-6} Pa as required from the RF cavity.

12.4.5   Water Cooling System

The beam pipes at the arc sections have cooling channels on both sides (outside the antechambers) in order to dissipate the heat caused by SR irradiation. The total SR power with design current (70.8 mA) is 7.2 kW. In order to maintain the average temperature rise of the beam pipe below 10 °C, the required flow rate of the cooling water is approximately 10 L min^{-1}.

The water chiller and the water pump are placed at the ground level. The water flow is divided into two flows corresponding to each arc sections, with each flow having five branches. Each branch is further divided into two channels that cool the beam pipe from both sides. Consequently, the water flow is divided into 20 channels, and the required flow rate of each cooling channel is 0.5 L min^{-1}. Since the inner diameter of the cooling channel of the beam pipe is 6 mm, the required flow speed is 0.29 m s^{-1}. The main pressure loss occurs in the cooling channel, which is less than 0.2 MPa.

12.4.6   Control System

As mentioned earlier, the vacuum system of the DR is divided into five sections by the gate valves, with each section controlled independently. The control system of the vacuum components is based on EPICS (Experimental Physics and Industrial Control System) and is almost same as that of the SuperKEKB main ring. The number of control data items of the DR, however, is much lower than that of the main ring.

In the DR, instead of using a vacuum gauge, pressure is estimated from the discharge current of the IPs, which are installed every 6 m. In each section, however, one cold cathode gauge is installed at the manifold between the beam pipe and the IP for calibration. One residual gas analyzer (RGA) is also installed in the manifold only in the east arc section.

The number of pressure gauges (i.e., the number of the IPs), thermometers, and water flowmeters used in the DR are approximately 30, 30, and 10, respectively. The pressure, the mass spectra of the residual gas, the temperatures of few vacuum components, and flow rates of the cooling water are continuously monitored during the beam operation.

12.4.7 Countermeasures against Electron Clouds

In order to suppress the ECE, some countermeasures are adopted mainly in the arc sections. As mentioned earlier, the beam pipes in the arc sections have antechambers in order to prevent the invasion of photoelectrons (which can cause the electron clouds) into the beam channel. Additionally, the side walls of the antechamber have a grooved structure for antireflection of the SR.

The SEY of the inner surfaces of the beam pipes is reduced by applying a thin TiN films of thickness 200 nm [29], not only for the arc sections but also for the straight sections. Figure 12.42 shows an inside view of the beam pipe for an arc section. The color of the inner surface of the beam channel changes to black due to TiN coating. The coating is performed in the coating facility in KEK, which also coated the beam pipes of the SuperKEKB LER [30][31].
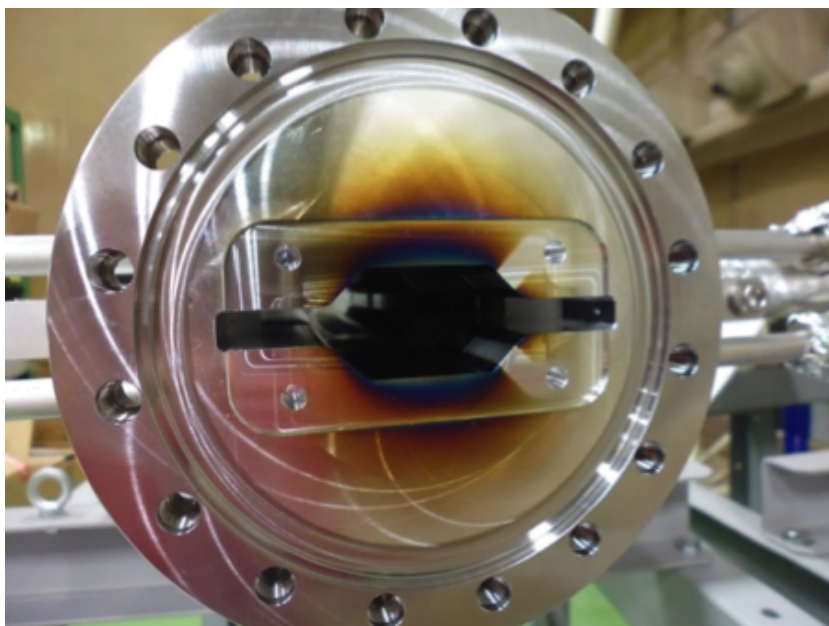
Figure 12.42: Almost all beam pipes are coated with TiN film with a thickness of 200 nm to reduce the secondary electron yield. The color of the inner surface of the beam channel changes to black due to TiN coating.

As an additional measure, the beam pipes in the arc sections have grooved surfaces on the upper and lower sides of the beam channel. In the presence of a dipole magnetic field, i.e., in the bending magnets, this structure reduces the SEY.

By these countermeasures, it is expected that the electron cloud density integrated over the ring can be suppressed to about 0.13×10^{14} m^{-2}, which is significantly smaller than the threshold of the electron cloud instability (1.4×10^{14} m^{-2}).

12.4.8   Construction and Evacuation

Almost all the beam pipes are pre-baked (150 °C, 24 hours) and coated with TiN films in the laboratory before their installation into the DR tunnel. No in-situ baking is performed after the installation.

After the installation, each section is evacuated using the rough pumping units from atmospheric pressure. During the evacuation and NEG activation, the pressure is monitored using vacuum gauges installed in the rough pumping units, and also by IPs after they are turned on. The evacuation with the IPs is initiated when the pressure decreased to less than $\sim 1 \times 10^{-4}$ Pa. When the pressure is further decreased to $\sim 1 \times 10^{-5}$ Pa, NEG activation is initiated. After NEG activation, the rough pumping units are isolated by angle valves and removed before beam operation. The heating power of NEG activation is controlled so that the monitored pressure does not exceed $\sim 2 \times 10^{-4}$ Pa during NEG activation concerning a possibility of degradation of NEG. Maximum activation temperature is approximately 380 °C, and activation time with maximum temperature is 1 hour. Though the hold time with maximum temperature is short, it is expected that almost 100 % activation will be obtained if it takes an enough long time to reach the maximum temperature.

12.5   DR Cavity

Introduction

We have proposed an RF accelerating structure for the positron damping ring (DR) as shown in Fig. 12.43 [32], and developed an RF cavity for the DR (hereinafter simply referred to as "the DR cavity") as shown in Fig. 12.44 [33]. We designed the DR cavity based on the higher-order-mode (HOM) damped structure of the normal-conducting accelerating cavity system ARES [34] (hereinafter simply referred to as "the ARES") used for the KEKB and SuperKEKB main rings (MRs).

Since the RF operation frequency is the same as used for the MRs, which is 508.887 MHz, the basic structure of the DR cavity is the same as that of the accelerating cavity in the ARES. However, no coupling or energy-storage cavities are used, just an accelerating cavity (single cell). The accelerating voltage per cavity (cavity voltage) in the ARES is 0.5 MV in specification. Previously, the required total voltage in the initial DR design was 0.26 MV, meaning that one cavity was enough for DR operation. However, it was shown theoretically that single-bunch instabilities caused by coherent synchrotron radiation would significantly affect the DR operation if such a total voltage was used. Now, a total voltage of 1.4 MV is required [35] but the theo-

Table 12.16: Average pressures of H_2 at the CCG ($p_{CCG}(H_2)$) and in the beam channel ($p_{BC}(H_2)$) without the stored beam calculated by Molflow+ varying the thermal gas desorption rate and the pumping speed of NEG (S_{NEG}). The N_2-equivalent values of $p_{CCG}(H_2)$ are also listed here.

Thermal gas desorption rate [$Pa\,m^3s^{-1}m^{-2}$]	S_{NEG} [m^3s^{-1}]	$p_{CCG}(H_2)$ [Pa]	$p_{BC}(H_2)$ [Pa]	$p_{BC}(H_2)/p_{CCG}(H_2)$	$p_{CCG}(H_2)$ in N_2 equivalent
1×10^{-8}	0.200	5.5×10^{-8}	6.1×10^{-8}	1.1	2.5×10^{-8}
	0.100	6.1×10^{-8}	7.4×10^{-8}	1.3	2.7×10^{-8}
2×10^{-8}	0.200	1.0×10^{-7}	1.1×10^{-7}	1.1	4.4×10^{-8}
	0.100	1.2×10^{-7}	1.5×10^{-7}	1.3	5.2×10^{-8}
3×10^{-8}	0.200	1.6×10^{-7}	1.8×10^{-7}	1.1	7.2×10^{-8}
	0.100	1.8×10^{-7}	2.2×10^{-7}	1.2	7.9×10^{-8}
4×10^{-8}	0.200	2.2×10^{-7}	2.4×10^{-7}	1.1	9.6×10^{-8}
	0.100	2.4×10^{-7}	2.9×10^{-7}	1.2	1.1×10^{-7}
5×10^{-8}	0.200	2.7×10^{-7}	3.1×10^{-7}	1.2	1.2×10^{-7}
	0.100	3.0×10^{-7}	3.6×10^{-7}	1.3	1.3×10^{-7}

retical uncertainty is still large. It should be noted that 1.4 MV is required as per the DR design specifications, and the hardware (cavity) performance should exceed this requirement. In order to supply a voltage higher than 1.4 MV to the DR in a space originally designed for one cavity, we have proposed and developed such RF accelerating structure that can accommodate up to three cavities (upstream, downstream, and middle ones). In this structure, each cavity body (shown in Fig. 12.44) is mounted with a high-power input coupler (used one from KEKB [36]), a movable tuner, HOM waveguide loads, and a vacuum evacuation system. In the DR tunnel, we assemble the cavities, separating them with grooved beam pipes (GBPs) [37], similar to LEGO blocks. We chose the cavity voltage in specification of the DR cavity to be 0.8 MV, higher than that of the ARES cavity (0.5 MV), guaranteeing a supply of 1.6 MV to the DR with two cavities (higher than the requirement of 1.4 MV), or 2.4 MV with three cavities. At the beginning of the commissioning of the DR, the accelerating structure is to have a two-cavity configuration as shown in Fig. 12.45, where a dummy duct is used in place of the middle cavity.

Apart from the coupling and energy-storage cavities, the DR cavity has the following space saving features that are not included in the ARES:

- The HOM absorbers are all compact tile-shaped silicon carbide ceramics [38] (hereinafter referred to as "SiC ceramic tiles"), as shown in Fig. 12.46 (whereas large bullet-shaped SiC ceramics were used for the HOM waveguide loads in the ARES).

- The neighboring cavities share a GBP in-between, extracting and damping horizontally polarized dipole modes out of harmful HOMs generated in the neighboring cavities when charged particles pass through them.

- The cavity is connected directly to GBPs with lip welding for vacuum sealing at the outer periphery (technically known as a "weld ring gasket"). It also includes RF shielding fingers and a centering location structure, as shown in Fig. 12.47.

In this accelerating structure, all of the related HOMs are damped, including those moving between the cavities, so that the electromagnetic field in each cavity has high independence. Furthermore, the number of cavities used in this accelerating structure is variable, yet it can still be considered a single mechanical structure with solid connections between the components (cavities, GBPs, etc.). This "multi single cell" design is the most significant characteristic of this structure.
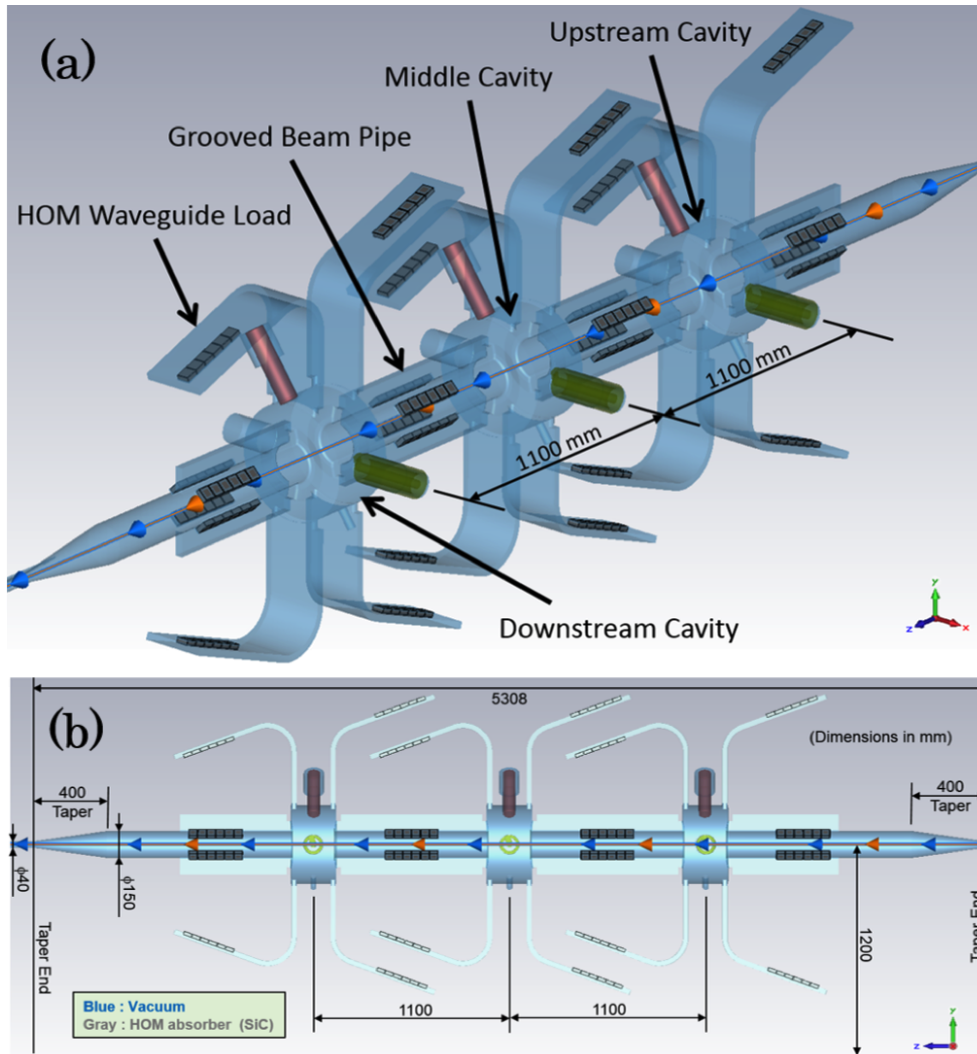
Figure 12.43: Overview of the RF accelerating structure for the SuperKEKB positron damping ring. (a) Perspective view. (b) Side view. The colored arrows indicate the direction of the positron beam.
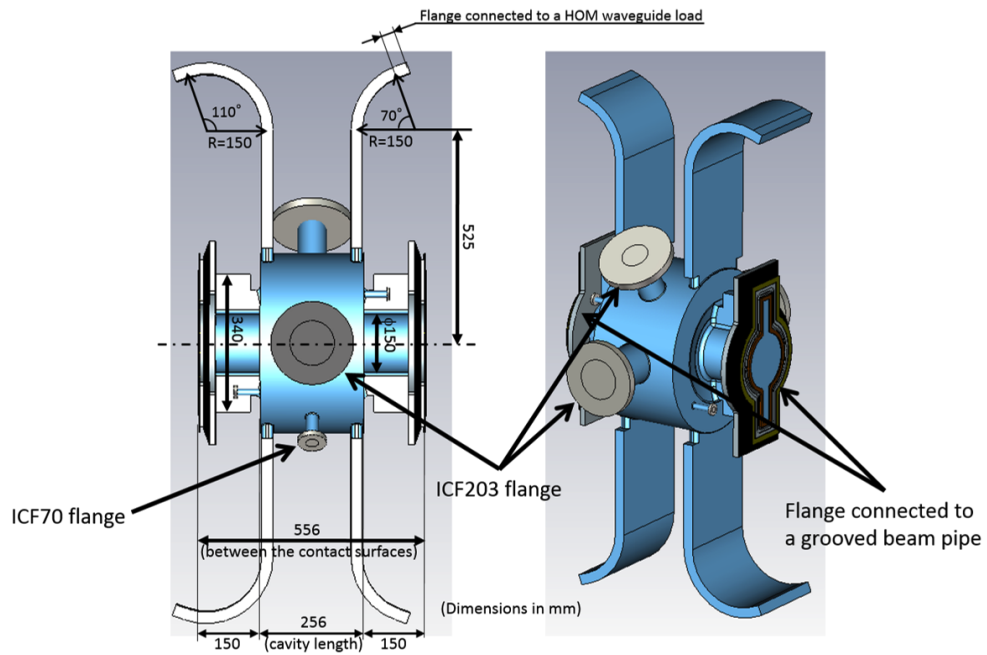
Figure 12.44: Conceptual diagram of the main body of the DR cavity (single cell). The blue region indicates the vacuum.
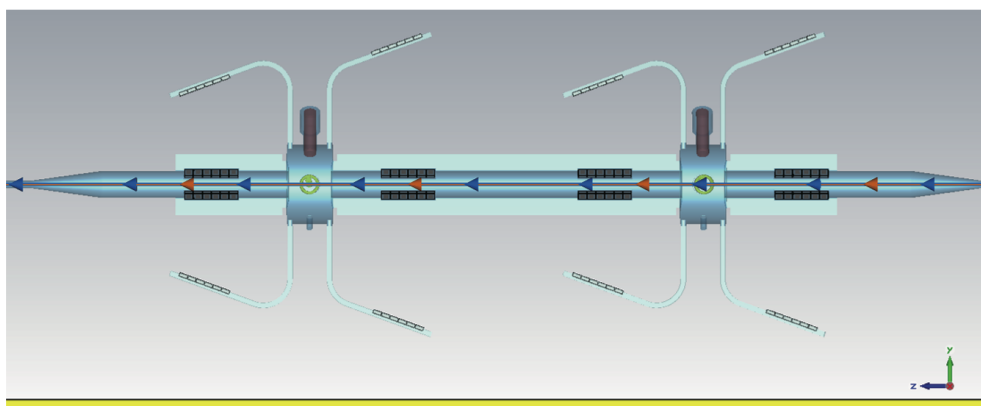
Figure 12.45: Two-cavity configuration.

Figure 12.46: The left photograph shows a unit of the HOM-absorbing structure; six SiC ceramic tiles are brazed on a water-cooled copper plate, and a stainless-steel frame is also brazed on the perimeter of such plate for TIG welding. The right photograph shows an inside of a GBP with four rectangular openings, in each of which such unit is fitted, and this GBP is hermetically sealed by TIG welding.
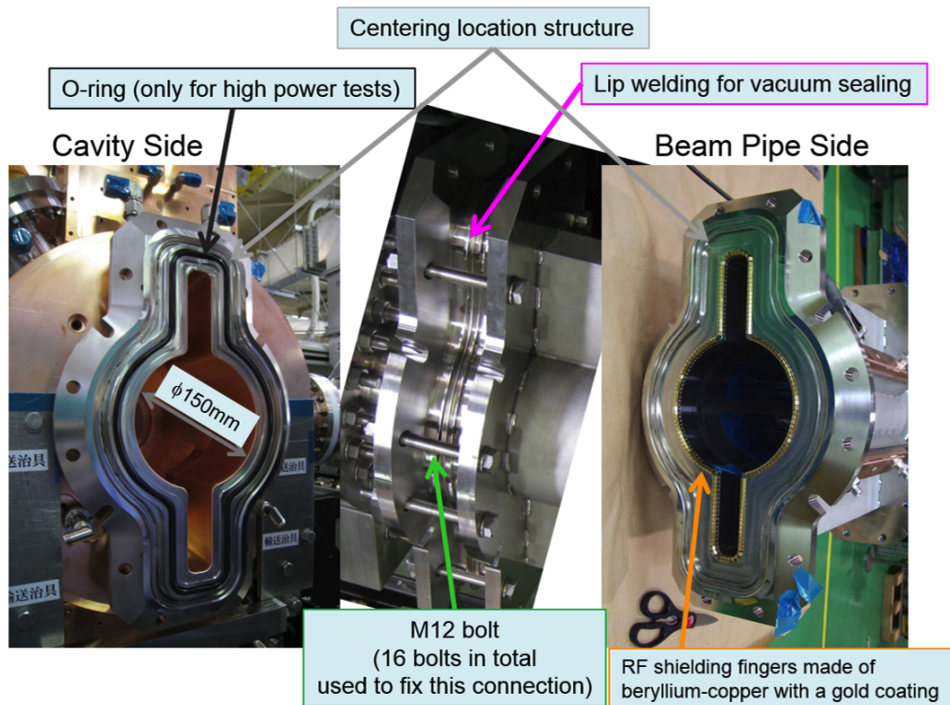
Figure 12.47: Connection between the DR cavity and GBP.
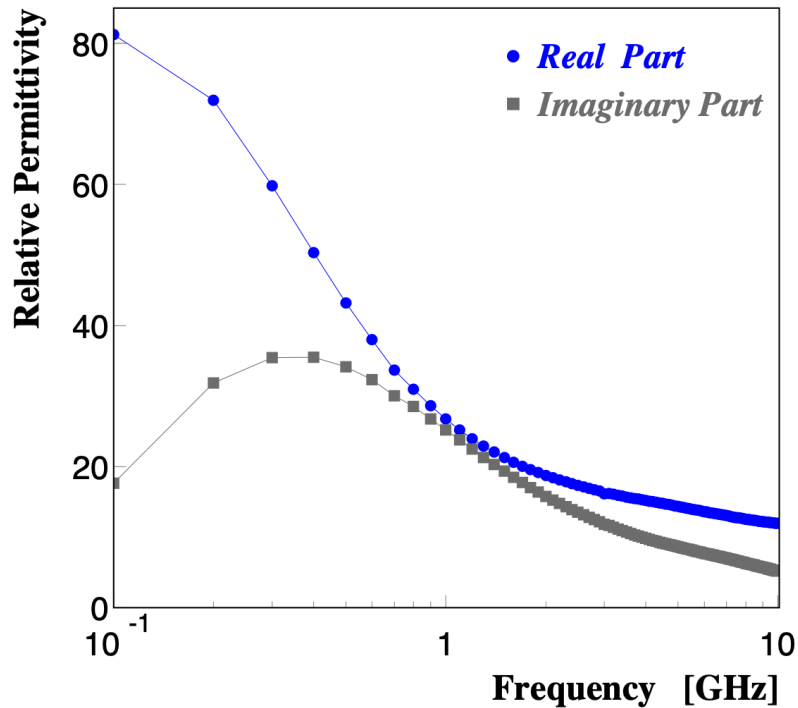
Figure 12.48: Relative permittivity of the SiC ceramics (CERASIC-B), as a function of frequency, used in designing this accelerating structure. These permittivity values are typical measurements on the SiC ceramic tiles used for the GBPs of the ARES.

Permittivity of the SiC ceramic tiles

In this HOM-damped structure, 168 SiC ceramic tiles in total are to be used for the three-cavity configuration (Fig. 12.43). We used the same technologies as used for the ARES on the sintering of SiC ceramic tiles and the brazing of them on water-cooled copper plates. However, permittivity of SiC ceramics largely depends on source SiC powders and sintering conditions. Because of this, we aggressively controlled the permittivity by changing the amount of aluminium contained in the SiC powder [39] so that the permittivity should be close to that used in designing this accelerating structure (Fig. 12.48).

Coupled bunch instabilities (CBIs)

We performed time-domain numerical simulations using a 3D electromagnetic field simulator GdfidL [49] to calculate wakepotentials for the whole accelerating structure including the taper sections with the inner diameter changing from 150 mm to 40 mm.
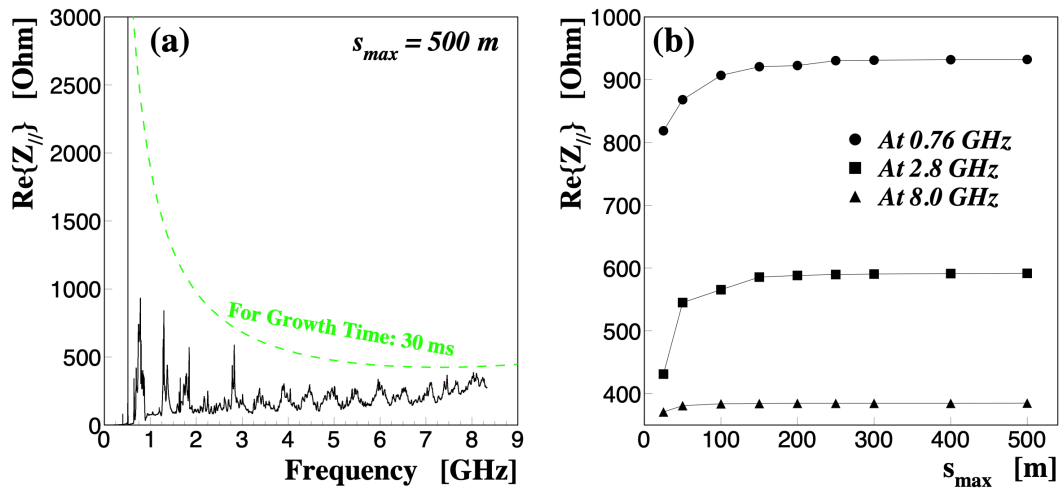
Figure 12.49: (a) Longitudinal impedance from the wakepotentials calculated up to
500 m ($s_\mathrm{max} = 500$ m). The green dashed line indicates a threshold of the CBI with
a growth time of 30 ms. (b) Longitudinal impedances at the peaks (0.76 GHz and
2.8 GHz) and maximum frequency of 8 GHz as a function of the length of the wakepo-
tentials calculated (s_max).

The loss factor is calculated from the short-range wakepotentials to be 2.3 V/pC for a
bunch length of 6.0 mm. The coupling impedances are obtained as Fourier transforms
of the wakepotentials, and compared with thresholds of the CBIs due to the HOM
impedance of this structure, as shown in Fig. 12.49 and Fig. 12.50. The growth time
of the longitudinal (transverse) CBI is long enough compared with the longitudinal
(transverse) radiation damping time of 5 ms (10 ms).

Coupled oscillation of the fundamental mode through the GBP

The cutoff frequency of the TM_{01} mode in the circular ϕ150mm duct is 1.5 GHz, which
is high enough compared with the accelerating-mode frequency (f_acc). However, the
geometrical symmetry of the cavity in the horizontal direction is broken by the movable
tuner and input coupler, leading to an excitation of a component of the horizontally-
polarized dipole mode (TM_{110}) in the cavities at f_acc, which is coupled to the TE
modes in the GBPs. Since the lowest cutoff frequency of the TE modes in the GBPs
is 575 MHz, which is close to f_acc, the accelerating mode (fundamental mode) in the
cavities could be coupled, via the TE mode, not via the TM mode, and therefore
coupled oscillation could be non-negligible.

This effect is estimated by two types of numerical simulations of eigenmode analyses

571
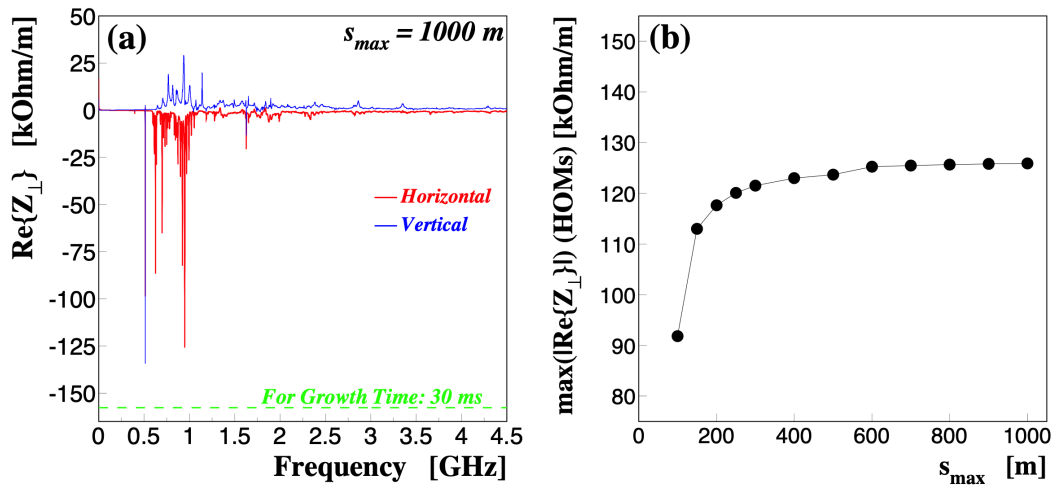
Figure 12.50: (a) Transverse impedances from the wakepotentials calculated up to 1000 m ($s_{\max} = 1000$ m). The beam offset in this simulation is $x = -4$ mm and $y = 4$ mm, where Cartesian coordinates (x, y, z) are defined as shown in Fig. 12.43. The green dashed line indicate a threshold of the CBI with a growth time of 30 ms. The horizontal impedance is significantly larger than the vertical one because horizontally (vertically) polarized dipole modes are damped by the GBPs (HOM waveguides). (b) Largest transverse HOM impedance as a function of the length of the wakepotentials calculated ($s_{\max}$).
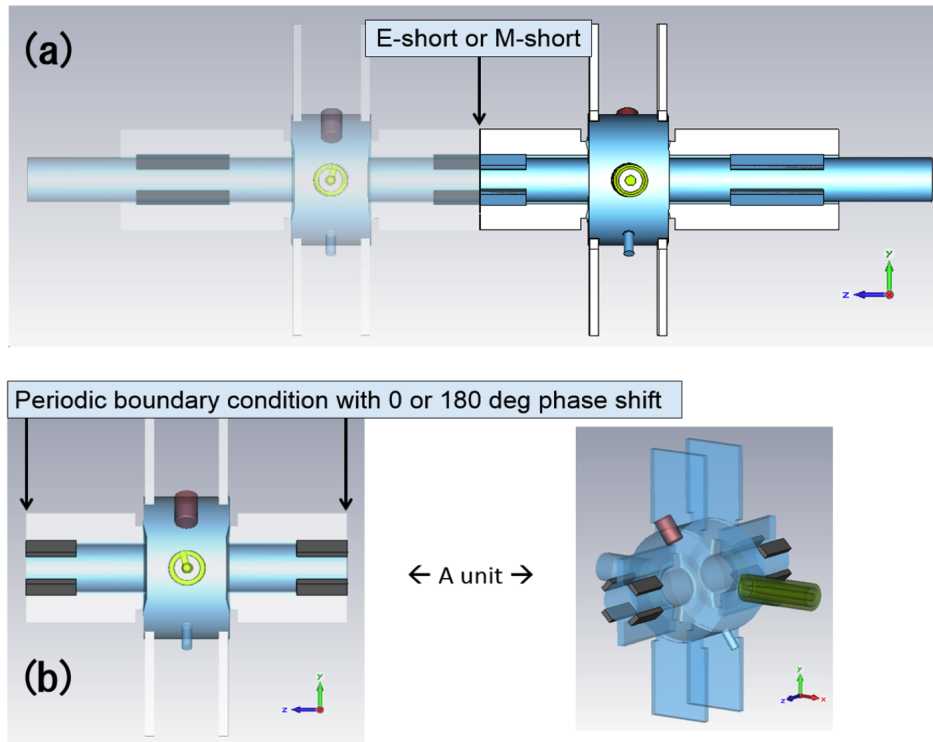
Figure 12.51: Solid models to estimate the coupled oscillation effects. (a) Two-cavity system. (b) Periodic structure.

with solid models shown in Fig. 12.51. For the model in Fig. 12.51-(a), a boundary condition of electric short (E-short) or magnetic short (M-short) is applied at the middle of the two cavities, while a periodic boundary condition with a phase shift of 0 or 180 degrees is applied in Fig. 12.51-(b). We used two different simulation codes, GdfidL and CST MICROWAVE STUDIO [41] (CST-MWS) to calculate the accelerating mode. These two codes use different algorithms not only in meshing but also in eigenmode calculations. The simulation results on the difference between the mode frequencies with the different boundary conditions are shown in Fig. 12.52, where the frequency differences, which are proportional to the coupling strength between the normal modes in the cavities, are of the order of 10 Hz, much lower than the width of Q_0: $f_{acc}/Q_0 \cong$ 20 kHz. In addition, there are good agreements between the results using CST-MWS and GdfidL. From the above results, it can be concluded that the calculated frequency differences are physical (not numerical noises), and the coupled oscillation effects for the three-cavity system, which should be between the two-cavity system and periodic structure, should be negligible.
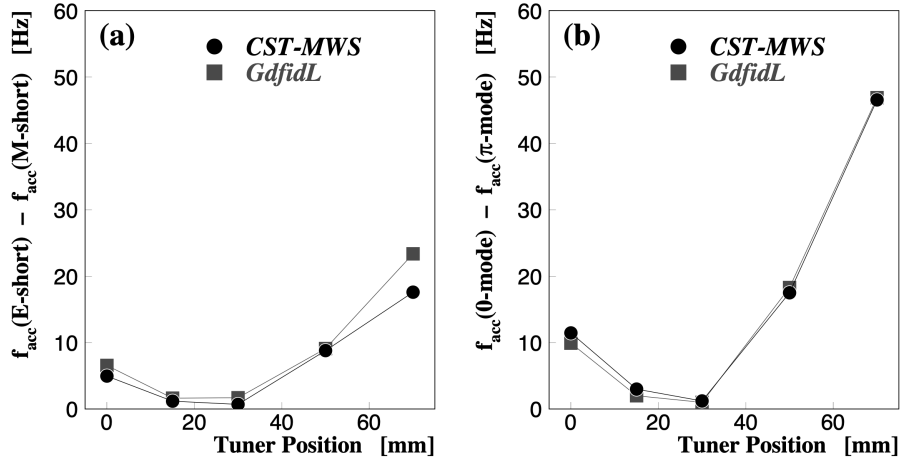
Figure 12.52: Differences of the mode frequencies with the different boundary conditions for the (a) two-cavity system, and (b) periodic structure. The home position of the movable tuner is 15 mm inside the cavity [43].

12.5.1   Main Body of the DR Cavity

The main body of the DR cavity is made of high-purity oxygen-free copper (class1), and consists of a barrel and two endplates, brazed into a cavity. Its conceptual diagram and design parameters are shown in Fig. 12.44 and Tab. 12.17, respectively. The DR cavity has twelve ports in addition to the beam ports: two ICF203 ports in the horizontal direction for an input coupler and vacuum evacuation, one ICF203 port for a movable tuner (tuner port), one ICF70 port to view the tuner, four ICF34 ports on the endplates for pickup antennas (monitor ports), and four HOM rectangular waveguides. The geometry of the vacuum region is symmetric with respect to both the horizontal and vertical planes including the beam axis except for the tuner and monitor ports, and also symmetric with respect to the vertical plane including the cavity center perpendicular to the beam axis (i.e. symmetric between the upstream and downstream half parts) except for the monitor ports and HOM waveguides.

Table 12.17: Design parameters of the DR cavity

Frequency	508.887	MHz
R_{sh}/Q_0	150	Ω
Q_0	~ 30000	
Cavity Voltage	0.8	MV

The vacuum evacuation system is attached directly to the DR cavity, and consists of two vacuum pumps located in the vicinity of the DR cavity: a turbo-molecular pump

574

(300L/s) and an ion-sputter pump (400L/s), leading to an expected vacuum pressure of 10^{-6} Pa during high power operation. Its mechanical support, as well as the support of the main body of the DR cavity, is put on a common baseplate. This baseplate has a complete alignment mechanism to be used in the alignment of the cavities in the DR tunnel.

Low power test

Accelerating-mode frequency f_{acc} is one of the most important quantities for RF cavities. Figure 12.53 shows the history of the measured frequency of the first production version of the DR cavity (cavity No.1). We have achieved 0.02 % accuracy in the frequency.

Unloaded quality factor (Q_0) is also an important quantity for RF cavities. Figure 12.54 shows Q_0 measurements as a function of the coupling loop angle of the input coupler. Fitting the measurements with a constant, the Q_0 value is estimated to be 92.9 %IACS for the prototype cavity (hereinafter simply referred to as "the prototype"), and 97.1 %IACS for cavity No. 1. This difference in Q_0 can be attributed to a difference of the surface protection process for the surfaces of the endplates to be exposed to high RF fields; acid cleaning followed by chromating applied to the prototype, while electro-polishing (EP) applied to cavity No.1 instead as shown in Fig. 12.55. This Q_0 improvement is consistent with the improvement of the surface roughness on the endplates by EP.

We also measured the external quality factor on the input coupler (Q_{ext}) as a function of the coupling-loop angle, and adjusted the coupling loop so that the input coupler was slightly over-coupled. The typical coupling factor with low RF power is 1.3 for a cavity temperature of 30 degC.

High power test [42]

The setup is shown in Fig. 12.56, where we used a 1 MW CW klystron as an RF high-power source. Figure 12.57-(b) shows the conditioning history of cavity No.1. The cavity voltage (V_c) reached 0.9 MV without any problems, exceeding the cavity voltage required by the specifications (0.8 MV). In this test, V_c is calculated according to the following formula,

$$V_c = \sqrt{R_{\mathrm{sh}}^{(\mathrm{HP})} \times P_{\mathrm{wall}}} \,, \tag{12.21}$$

where P_{wall} is a wall-loss power calculated from the input RF power to the cavity (P_{inp}) and the reflected RF power from the cavity (P_{refl}), both of which are measured with
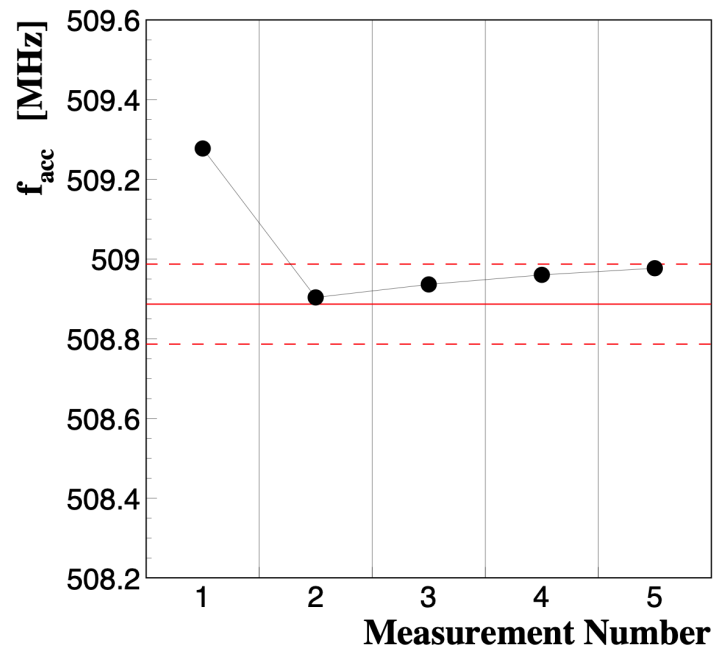
Figure 12.53: Measurements of the accelerating-mode frequency (f_{acc}), converted to those for a cavity temperature of 30 degC and vacuum inside the cavity, with the movable tuner at its home position (15mm inside). The horizontal solid and dashed lines indicate a target frequency and its range ($\pm 100\,\mathrm{kHz}$), respectively. The measurement number indicates each step in the production process: 1. before the frequency tuning (with air inside), 2. after the frequency tuning and before the brazing of the cavity main body (with air inside), 3. after the brazing and before the delivery (with air inside), 4. during the preparation for the high power test at the test stand (with nitrogen inside), and 5. just before the start of the high power test (with vacuum inside).
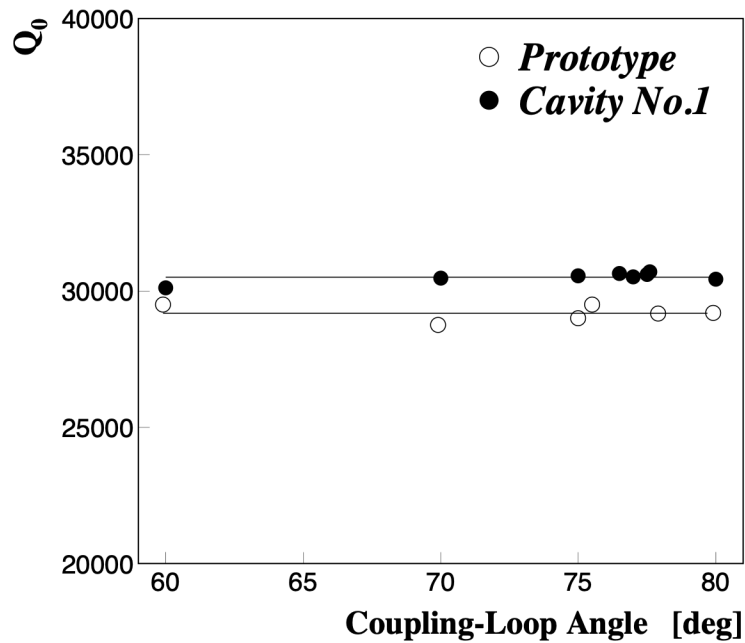
Figure 12.54: Measurements of Q_0 for the prototype cavity (open circles) and cavity No.1 (closed circles), converted to those with a cavity temperature of 20 degC. Fitting these measurements with a constant, the Q_0 values are estimated to be 29186 for the prototype, and 30506 for cavity No.1. Reduced χ^2 values in the fittings, assuming 1 % error for Q_0, are all smaller than one.
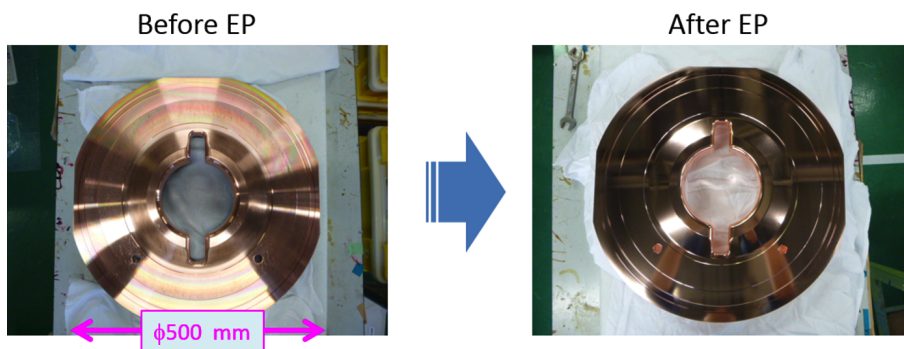
Figure 12.55: Photographs of the endplate of cavity No.1 before (left) and after (right) electro-polishing (EP) with about 40 μm of etching. Through EP, the average surface roughness (usually denoted by "R_a") was improved from about 1.5 μm to about 0.2 μm.

power meters and sensors directly connected to the directional coupler near the cavity:

$$P_{\text{wall}} = P_{\text{inp}} - P_{\text{refl}} \,, \tag{12.22}$$

and $R_{\text{sh}}^{(\text{HP})}$ is a shunt impedance with high RF power calculated as

$$
\begin{aligned}
R_{\text{sh}}^{(\text{HP})} &= (R_{\text{sh}}^{(\text{HP})}/Q_0^{(\text{HP})}) \times Q_0^{(\text{HP})} \tag{12.23} \\
&= (R_{\text{sh}}^{(\text{cold})}/Q_0^{(\text{cold})}) \times Q_0^{(\text{HP})} \tag{12.24} \\
&= 150\,\Omega \times Q_0^{(\text{HP})} \,, \tag{12.25}
\end{aligned}
$$

where $Q_0^{(\text{HP})}$ is an unloaded quality factor with high RF power, and the ratio of the shunt impedance and unloaded quality factor without RF power $(R_{\text{sh}}^{(\text{cold})}/Q_0^{(\text{cold})})$ is calculated from the simulation to be $150\,\Omega$. In the above Eq. (12.25), $Q_0^{(\text{HP})}$ is calculated according to the following formula,

$$Q_0^{(\text{HP})} = \beta^{(\text{HP})} \times Q_{\text{ext}} \,, \tag{12.26}$$

where Q_{ext} is a result of low power measurement, and $\beta^{(\text{HP})}$ is a coupling factor of the input coupler with high RF power calculated as

$$\beta^{(\text{HP})} = \frac{1 + \sqrt{P_{\text{refl}}/P_{\text{inp}}}}{1 - \sqrt{P_{\text{refl}}/P_{\text{inp}}}} \,. \tag{12.27}$$

Also shown in Fig. 12.57-(a) is the conditioning history of the prototype for comparison, revealing that cavity No.1 has the following advantages:

(a) Lower vacuum pressure (i.e. better vacuum), and

(b) Lower trip rate.

In addition, as shown in Fig. 12.58,

(c) Lower radiation dose rate (about one fifth), meaning that there were fewer field-emitted electrons with the same cavity voltage.

It should be emphasized that all of the above advantages, the higher value of Q_0 and (a)-(c), are a result of EP because the surface protection process (EP or acid cleaning followed by chromating) is the only significant difference, between the prototype and cavity No.1, related to the high-power RF performance. It should also be noted that we could not make a simple comparison between the times taken to reach $0.9\,\text{MV}$ because of the different conditioning parameters in the automatic computer controls.

Table 12.18 shows results of a stability test for cavity No.1 while maintaining a constant V_c, performed after reaching $0.9\,\text{MV}$ in the conditioning, where cavity trip was
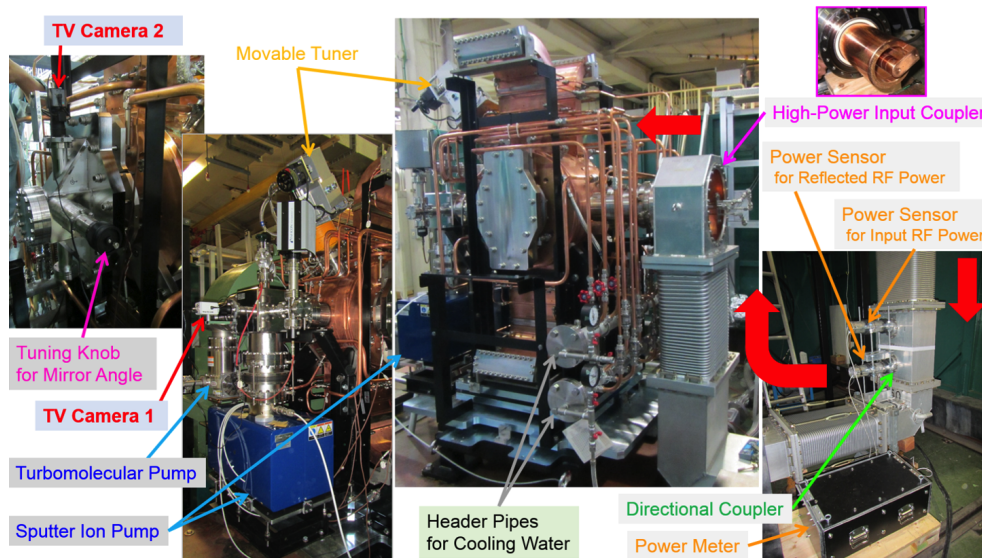
Figure 12.56: Setup of the high power test for cavity No.1.
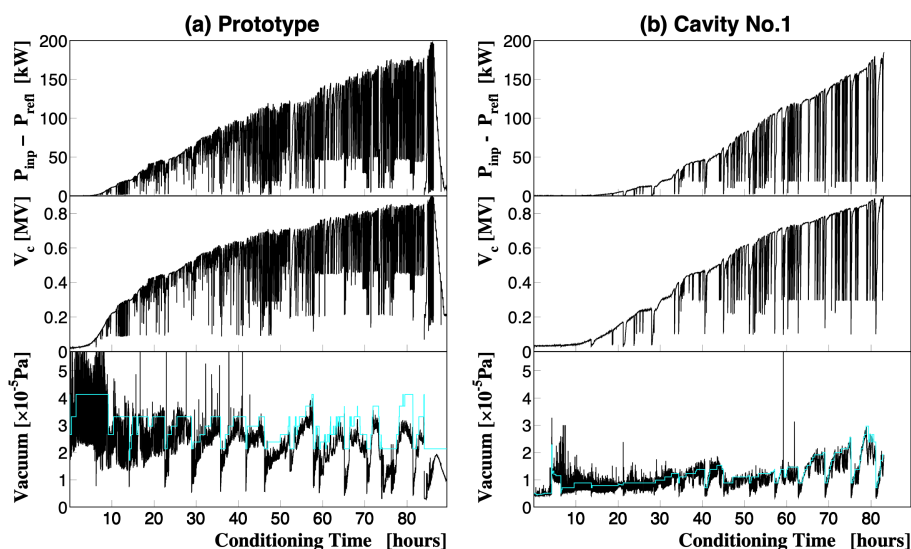
Figure 12.57: Conditioning histories until V_c reached $0.9\,\mathrm{MV}$ with data points recorded every ten seconds plotted. Data with holding the input RF power and data for tuning the control system or klystron are excluded here. The light blue lines indicate the reference vacuum pressure specified in the automatic conditioning by computer control. If the vacuum pressure is higher than the reference, the power is slightly stepped down until the vacuum pressure becomes lower than the reference, and then the power is slightly stepped up as long as the vacuum pressure is lower than the reference.
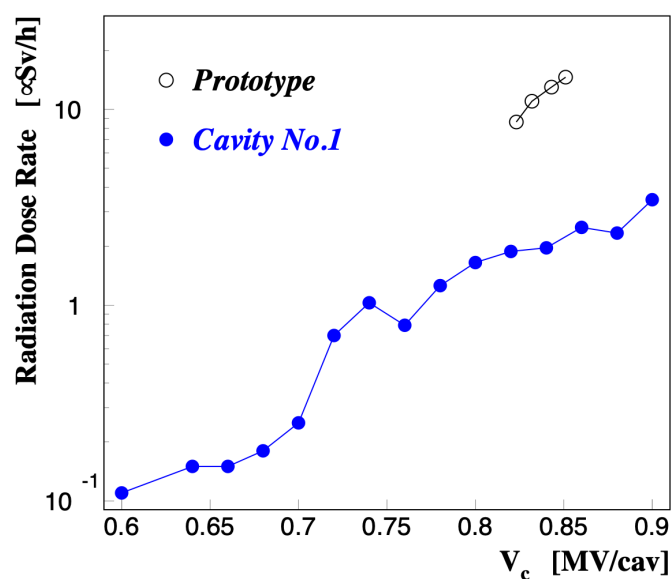
Figure 12.58: Radiation dose rates, on the way to $V_c = 0.9\mathrm{MV/cav}$, measured at about $2\,\mathrm{m}$ away from the cavities in the radiation controlled area. The radiation dose rates exceed the background levels (about $0.1\,\mu\mathrm{Sv/h}$) because of the X-rays generated when field-emitted electrons from the inner surface of the cavity accelerate and impact on opposite inner surface.

identified with interlock by P_{refl} and decay time of the cavity pickup signal. The results indicate that cavity No.1 can operate stably with $V_c = 0.8\,\text{MV/cav}$ in specification. Furthermore, to examine the performance limit, we performed an endurance test by raising the cavity voltage up to $0.95\,\text{MV/cav}$, and observed no limit related to the thermal or high-field RF performance. The cavity voltage of $0.95\,\text{MV/cav}$ was the highest voltage permitted by the radiation regulation for the test stand.

12.5.2   Grooved Beam Pipe (GBP)

The GBP, shown in Fig. 12.59, is a stainless-steel duct with grooves. The basic structure is similar to that of the ARES. However, there is one significant difference that the GBP for the DR cavity has SiC ceramic tiles attached on the circular part, not on the grooves. This difference enables the GBP for the DR cavity to absorb not only TE modes but also TM HOMs moving between the cavities. However, such SiC ceramic tiles are seen from a positron beam although the maximum beam current stored in the DR is low (70.8 mA). We have confirmed the total HOM power absorbed in the SiC ceramic tiles is small enough, smaller than $200\,\text{W / GBP}$ for the DR design, by performing a time-domain numerical simulation with a beam using GdfidL. We have also confirmed that the maximum power of the accelerating mode absorbed in the SiC ceramic tiles is small enough, smaller than $100\,\text{W / GBP}$ for $P_{\text{wall}} = 200\,\text{kW}$ and movable tuner positions between 0 and 40 mm [43], by performing an eigenmode analysis with the SiC ceramic tiles on the GBP using CST-MWS. Therefore, the total absorbed RF power during DR operation is estimated to be smaller than $300\,\text{W / GBP}$, which is lower than the power capability of the GBP: $480\,\text{W / GBP}$, demonstrated at a test stand (see below).

V_c [MV/cav]	P_{wall} [kW]	Total Holding Time [hours]	Number of Cavity Trips
0.80	144	30.5	1
0.85	164	18	0
0.90	186	14.5	3
0.95	210	8	1

Table 12.18: Results of the stability test for cavity No.1.
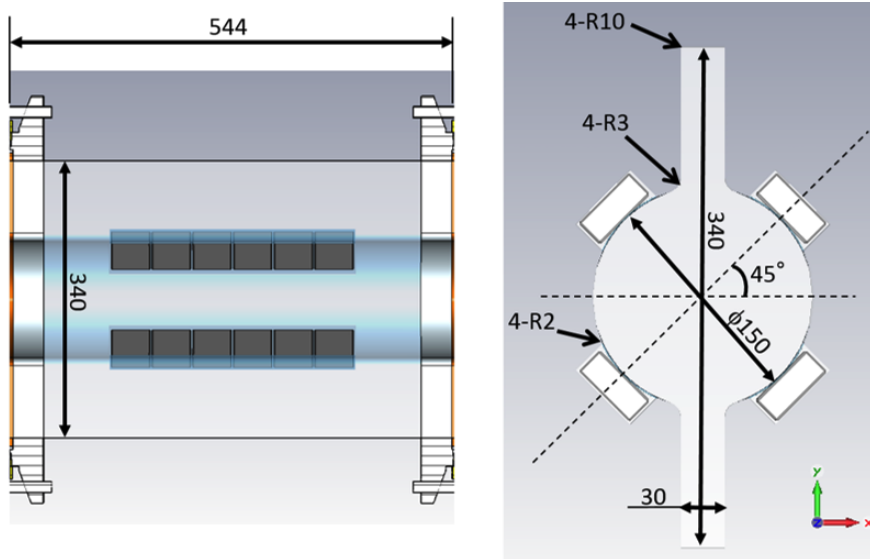
Figure 12.59: Conceptual diagram of the GBP with four units of the HOM absorbers (SiC ceramic tiles).

Connection to the cavity

The structure of the connection to the cavity is shown in Fig. 12.47, where the RF fingers fill a 1.9 mm gap between the GBP and cavity. Heating of this connection structure by the wake field is estimated by making a solid model including the RF fingers as shown in Fig. 12.60. We performed a time-domain numerical simulation with a beam using GdfidL, where the mesh size was 0.1 mm. The calculation results are shown in Fig. 12.61; the wake field is strongly suppressed by the RF fingers (Fig. 12.61-(a)) , and no resonant modes are excited (Fig. 12.61-(b)). From this simulation, the loss factor for this structure is also estimated to be 0.00048 V/pC, which corresponds to a loss power of 0.27 W at this connection structure for the DR design. Therefore, such heading due to the wake field is negligible.

High power test

We performed a high power test for the GBP prototype with a setup shown in Fig. 12.62, where we used a 1.25 GHz L-band klystron as an RF high-power source, and a winged chamber prototype loaded with bullet-shaped SiC ceramics [44] as a load. The results are shown in Fig. 12.63; there is no vacuum-pressure spike as well as no abnormal temperature increase. Furthermore, no discharge in the GBP was observed with the TV camera. Finally, we visually inspected the inside of the GBP prototype after this high power test, and found no damages on the SiC ceramic tiles and RF fingers, as
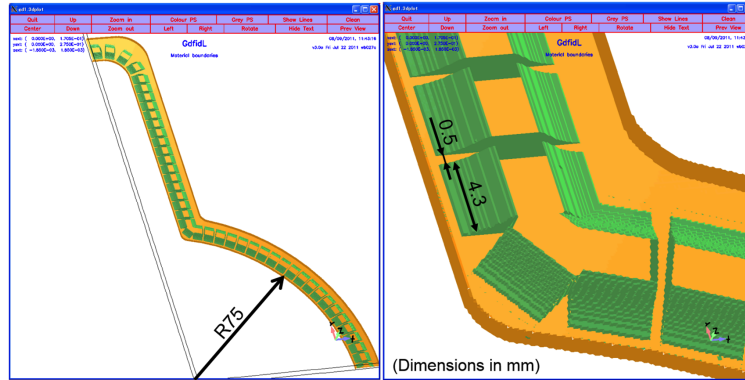
Figure 12.60: Solid model of the connection structure between the GBP and cavity with RF fingers (green), which is used in the wakefield simulation.
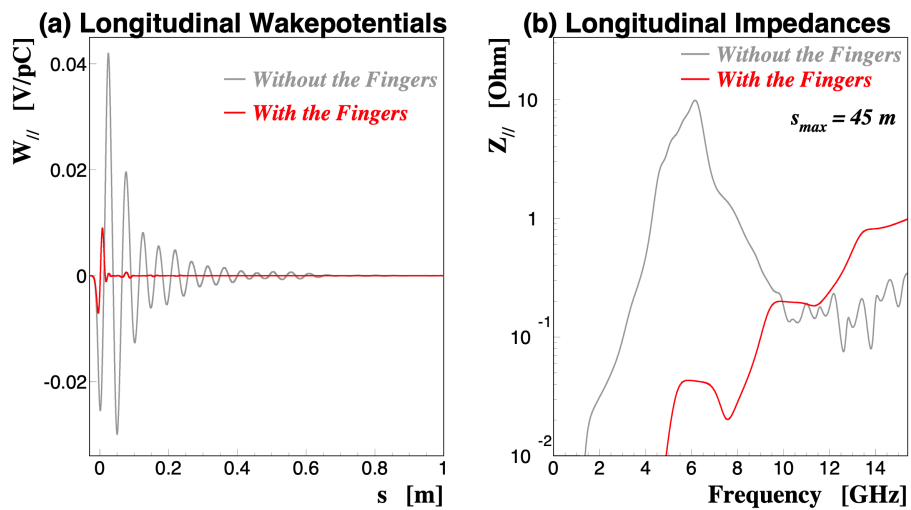
Figure 12.61: Simulation results of the longitudinal (a) wakefields and (b) impedances for the connection structure between the GBP and cavity. Results without the RF fingers are also shown for comparison.
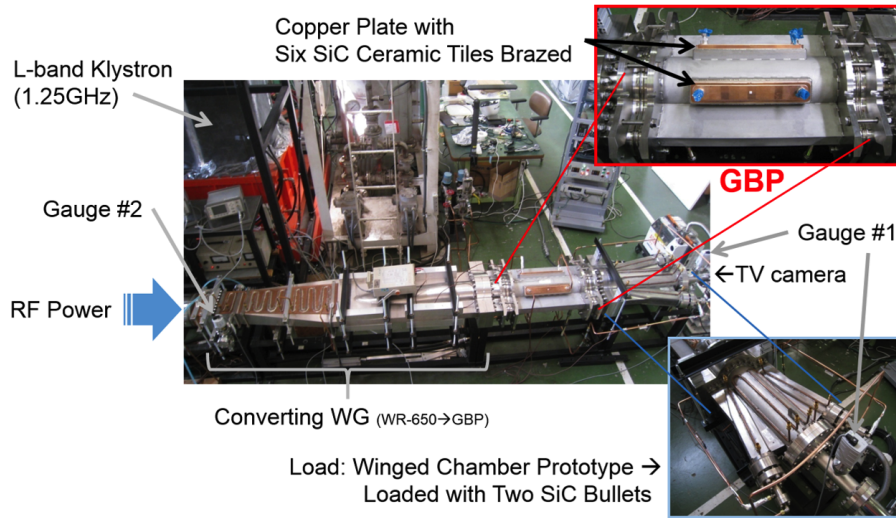
Figure 12.62: Setup of the high power test for the GBP prototype, where high RF power of the TE_{10} mode comes from the left through the rectangular waveguide (WG).

shown in Fig. 12.64.

12.5.3 HOM Waveguide Load

The HOM waveguide load, shown in Fig. 12.65, is a rectangular stainless-steel waveguide with one unit of the HOM absorbers (SiC ceramic tiles) attached at the center of the E-plane. This unit has the same structure as that for the GBP, shown in Fig. 12.46, however, we have adjusted the position of the unit, Δ defined in Fig. 12.65, so that HOMs of TM_{011}, TM_{012} and TM_{013}, as seen in Fig. 12.49-(a) as impedance peaks, are effectively absorbed, keeping a good broadband performance up to the cutoff frequency of the TM_{01} mode in the $\phi 40$mm circular ducts upstream and downstream the RF section (5.7 GHz). Based on the simulation results on the reflection coefficient ($|S_{11}|$) shown in Fig. 12.66, the Δ value is optimized to be 12 mm, where $|S_{11}|$ with Δ = 12 mm has the best performance to absorb the TM_{011} mode.

From a time-domain numerical simulation with a beam using GdfidL, the total HOM power absorbed in the SiC ceramic tiles during DR operation is estimated to be smaller than 30 W / load for the DR design, and from an eigenmode numerical calculation with the SiC ceramic tiles, the power of the accelerating mode absorbed in the SiC ceramic tiles is estimated to be smaller than 130 W / load for $P_{\text{wall}} = 200$ kW. Therefore, the total absorbed RF power is estimated to be smaller than 160 W / load, which is much lower than the power capability of this load: 1.8 kW / load, demonstrated at a test stand (see below).
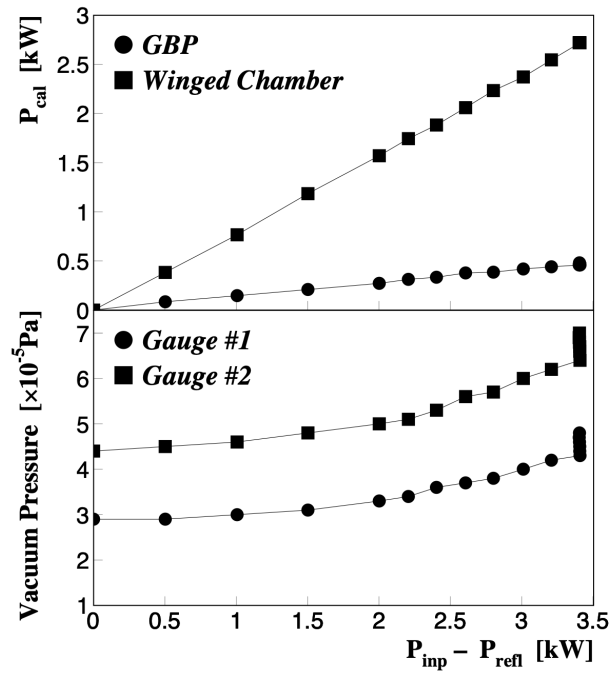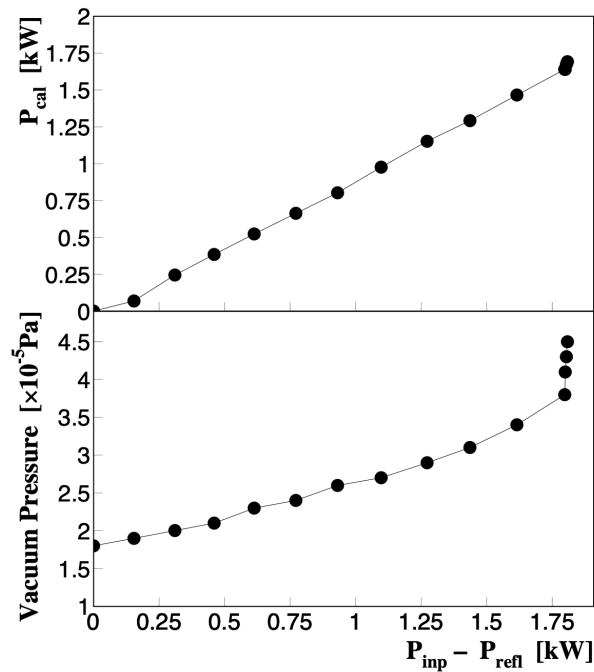
Figure 12.63: Results of the high power test of the GBP prototype: (top) absorbed powers calorimetrically calculated from the temperatures of the cooling water for the SiC ceramics (P_{cal}), and (bottom) vacuum pressures measured with the gauge #1 and #2 shown in Fig. 12.62. The input RF power to the GBP and load (P_{inp}) was gradually stepped up, about $0.5\,kW$ per ten minutes, up to $P_{inp} = 3.4\,kW$, and then kept for one hour with $P_{inp} = 3.4\,kW$ and $P_{cal}(GBP) = 480\,W$. The vacuum pressure increase at $P_{inp} - P_{refl} = 3.4\,kW$ is due to the temperature increase of the GBP and load. The reflected power from the GBP and load (P_{refl}) is smaller than $10\,W$ for $P_{inp} = 3.4\,kW$.
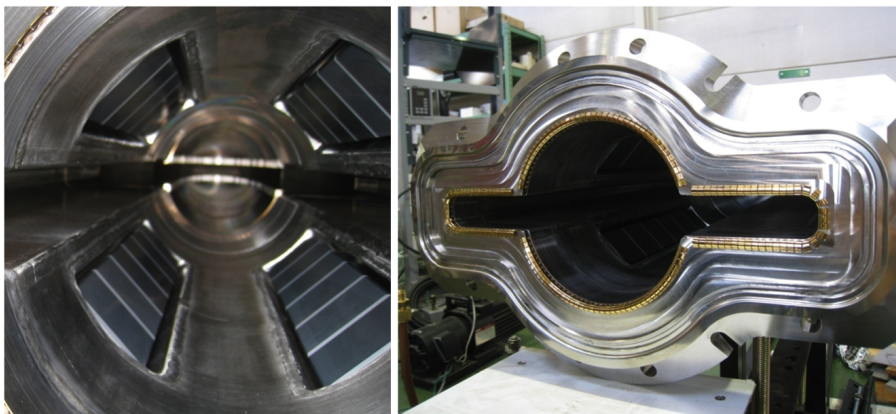
Figure 12.64: Inside of the GBP prototype (left) and its connection structure (right) under the inspection after the high power test.
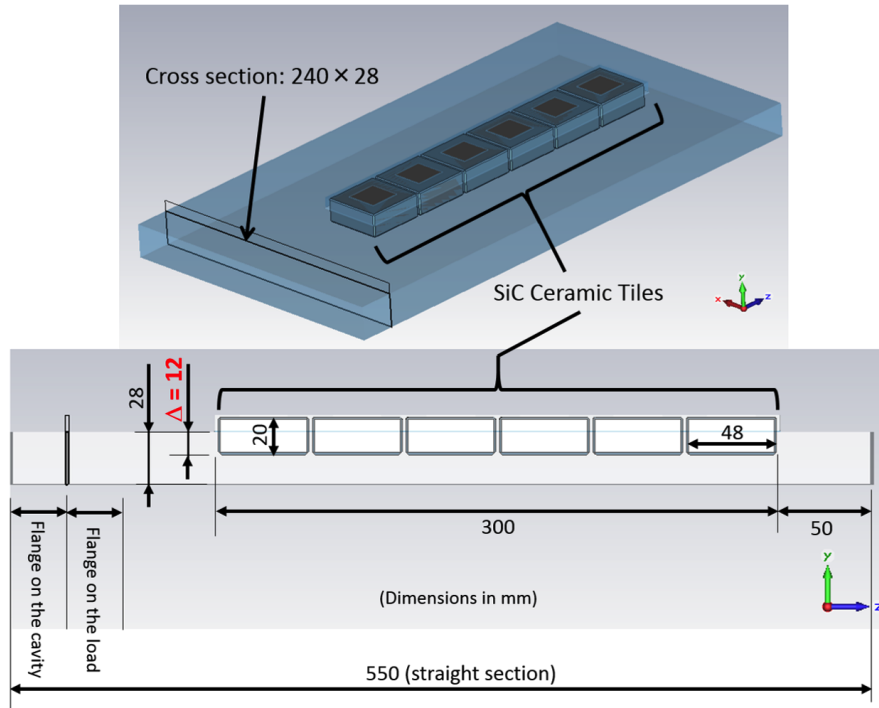
Figure 12.65: Conceptual diagram of the HOM waveguide load with one unit of the HOM absorbers (SiC ceramic tiles).

High power test

We performed a high power test for the HOM waveguide load prototype with a setup shown in Fig. 12.67, where we used the same L-band klystron (1.25GHz) as used in the high power test of the GBP prototype. The results are shown in Fig. 12.68; there is no vacuum-pressure spike as well as no abnormal temperature increase. Furthermore, no discharge in this HOM waveguide load prototype was observed with the TV camera. Finally, we visually inspected the inside after this high power test, and found no damage on the SiC ceramic tiles.

12.5.4 Assembly Test

As shown in Fig. 12.69, we performed an overall assembly test with the four HOM waveguide loads and two GBPs mounted on to the cavity No.1, where the vacuum sealing was successful.
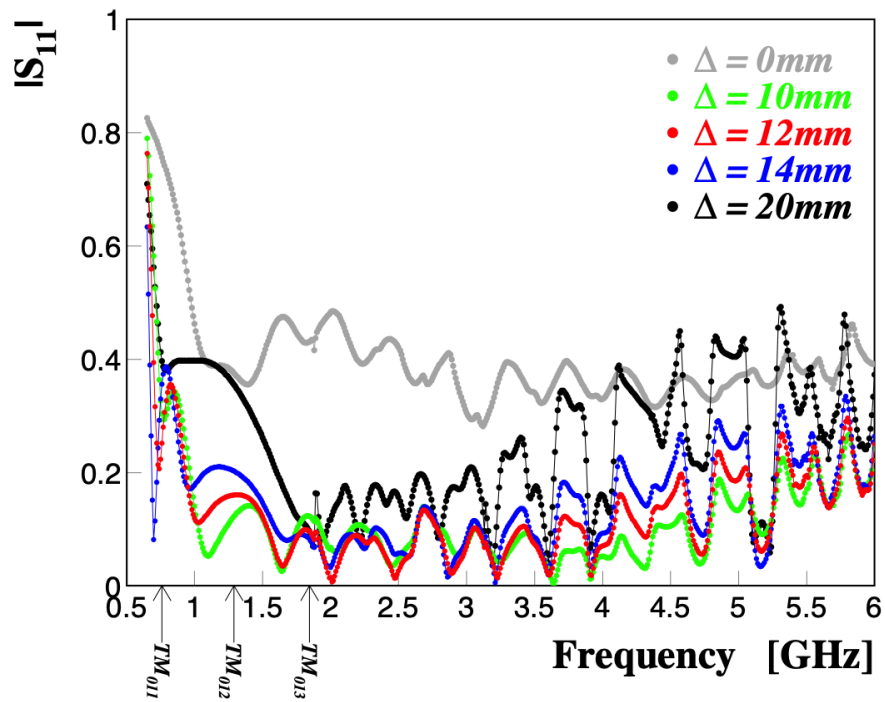
Figure 12.66: Simulation results on the reflection coefficient ($|S_{11}|$) of the HOM waveguide load. Using CST-MWS, we performed frequency-domain calculations with an input RF wave of the TE_{10} mode at 536 equidistant frequency points in a range from 0.65 GHz up to 6 GHz, where the solid model shown in Fig. 12.65 was used.
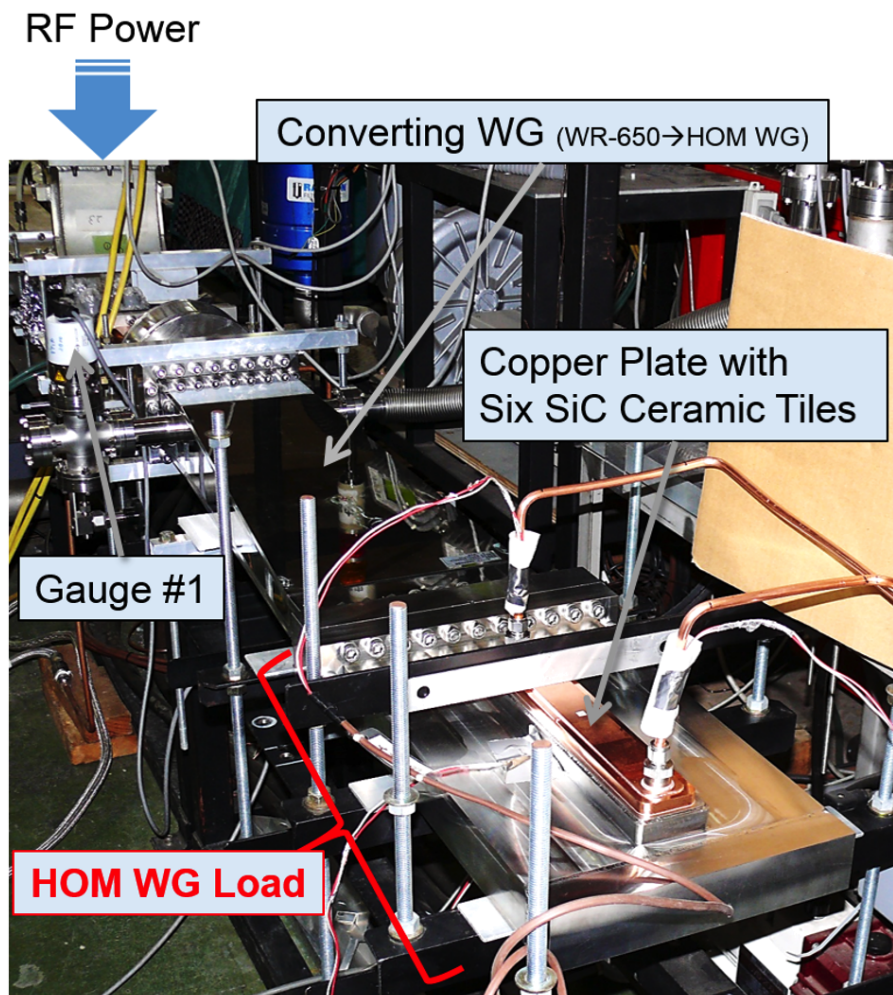
Figure 12.67: Setup of the high power test of the HOM waveguide load prototype, where high RF power of the TE_{10} mode comes from the upper left through the rectangular waveguide (WG).

Figure 12.68: Results of the high power test of the HOM waveguide load prototype: (top) absorbed power calorimetrically calculated from the temperatures of the cooling water for the SiC ceramic tiles (P_{cal}), (bottom) vacuum pressure measured with the gauge #1 shown in Fig. 12.67. The input RF power to the load (P_{inp}) was gradually stepped up, about $0.2\,\mathrm{kW}$ per ten minutes, up to $P_{\mathrm{inp}} = 2.2\,\mathrm{kW}$ ($P_{\mathrm{inp}} - P_{\mathrm{refl}} = 1.8\,\mathrm{kW}$), and then kept for forty minutes with $P_{\mathrm{inp}} - P_{\mathrm{refl}} = 1.8\,\mathrm{kW}$ and $P_{\mathrm{cal}} = 1.7\,\mathrm{kW}$. The vacuum pressure increase at $P_{\mathrm{inp}} - P_{\mathrm{refl}} = 1.8\,\mathrm{kW}$ is due to the temperature increase of the load.
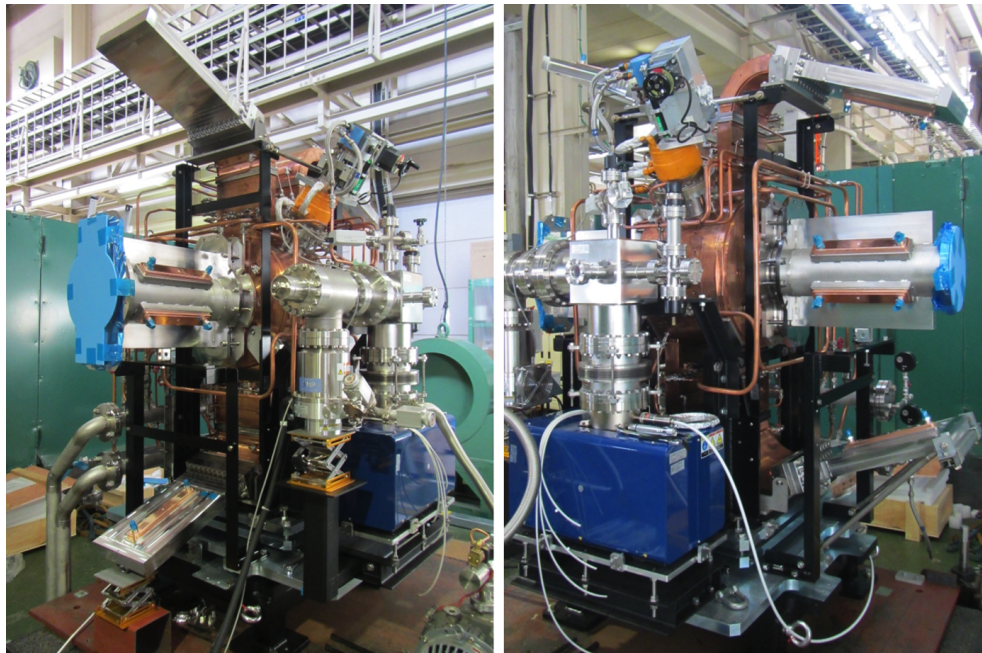
Figure 12.69: Cavity No.1 with the HOM waveguide loads and GBPs mounted

12.5.5 Summary

We have developed the accelerating structure for the DR based on the HOM-damped structure of the successful ARES cavity system. High power tests were done for all of the high-power components of the structure: the cavities, GBP prototype, and HOM waveguide load prototype. The performances of the components (cavity voltage and power capabilities) have been demonstrated to be over the specifications required for the DR design.

12.6   RF Driving System

Figure 12.70 shows schematic draw of RF system composition for the DR and monitor signals to be treated by the LLRF control system (DR-LLRF) in the complete configuration. Hardware components and control technique are almost the same as that of the MR. However three cavities, which are the upper (U-), middle (M-) and down (D-) stream cavity, respectively, are driven by one klystron as shown in Fig. 12.70. Then the waveguide system needs two dividers of a Magic-T (MT) type. The first divider of the two divides the driving power in 1:2-ratio for equipartition to the three cavities. Required klystron output power is ~800 kW for the three cavities. The klystron and the DC high-voltage power supply system are the same as that used in the MR.

The DR-LLRF architecture is the same as that of MR, except vector sum of the three cavity fields should be controlled concurrently with respective cavity-tuning controls of the three. The vector sum is calculated in an FPGA from sampled I/Q components of the cavity pick-up signals and then feedback control is applied to I/Q modulation for the klystron driving. Since number of monitor signals to be treated in this system is larger than that of the MR, additional FPGA boards will be needed for the three-cavity driving. Beam loading and coupled bunch instability might be negligible small in comparison with that of MR.

RF source (reference) signal of 508.887 MHz is common with the MR. It is provided from the central control room of MR through an optical link to the DR-LLRF system for synchronisation with the MR RF acceleration.

For bucket selection of injection to the MR, it is required that injection timing can be changed in pulse-by-pulse. In order to shift the timing to meet the arbitrary bucket of the MR, RF phase shifting of the DR is considered as one candidate of the method for the bunch selection [45]. This method requires arbitrary phase rotation of the cavities at synchronised timing with the positron injection of 25-Hz repetition. For this phase rotation to be possible, the DR-LLRF has to be coordinated with the event timing system of the linac[46] to receive the event trigger with the request information.

12.7   Instrumentation

12.7.1   Overview

The beam instrumentations of DR are based on those of the main rings [47]. Some of the KEKB instrumentations are re-used for DR. The system of the DR bean instrumentations is shown in Table 12.19 and the layout is shown in Fig. 12.71. There are 4 monitor stations near the cable holes from the tunnel to a DR power supply
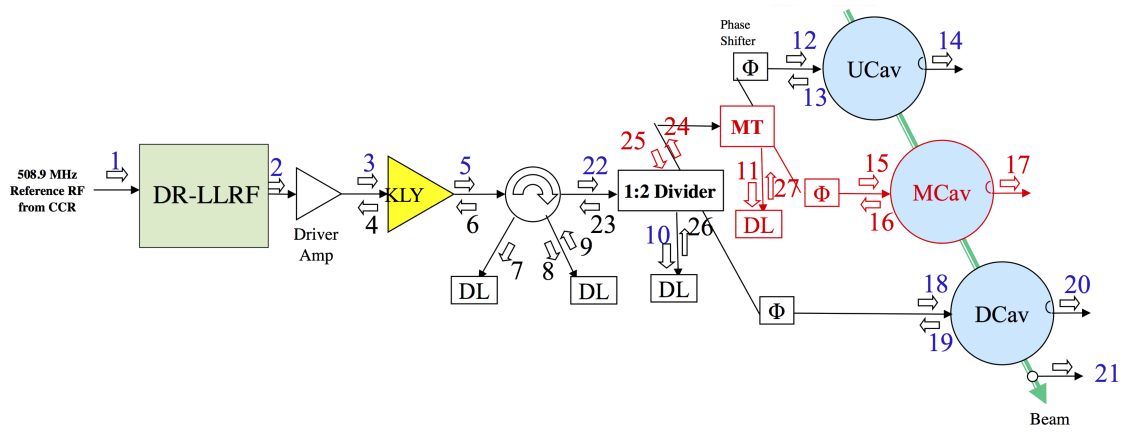
Figure 12.70: Schematic draw of RF system for DR and signal flows to be treated by the DR-LLRF control system.
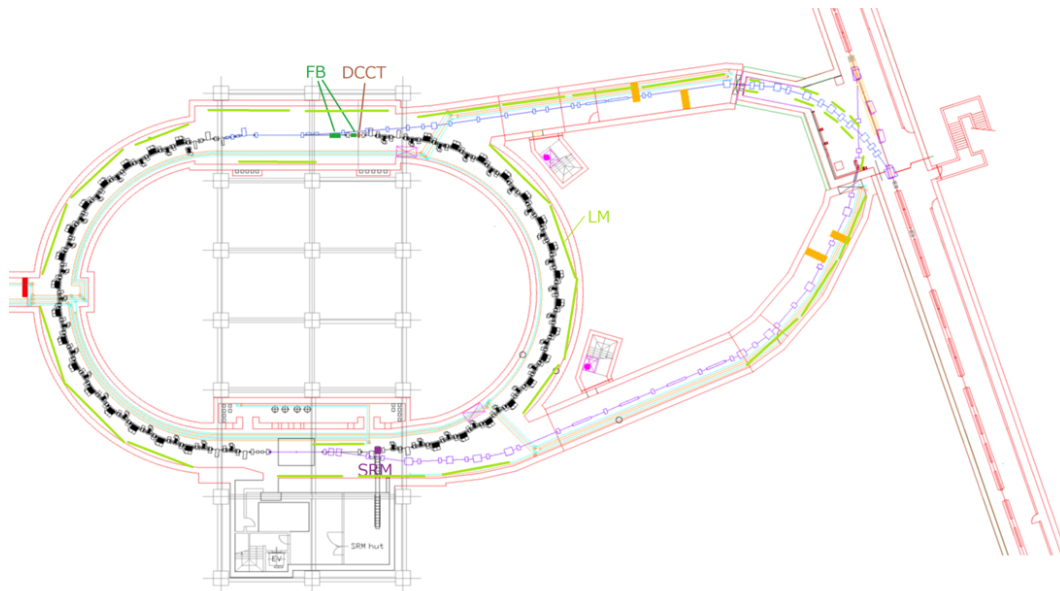

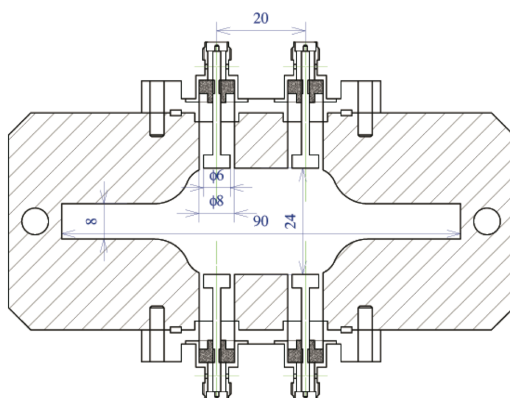Figure 12.71: Layout of the SuperKEKB DR.

Figure 12.72: Drawing of the normal BPM chamber for SuperKEKB Damping Ring.

building. A few VME racks and NIM BINs for beam position monitor (BPM) signals are located there. Each station is connected through network and supplied with the RF (508.887MHz), revolution and bunch timing signals. Beam feedback system (FB) signals are sent to one of the stations. Beam loss monitor (LM) and current monitor (DCCT) signals are collected at the control room. The synchrotron radiation monitor (SRM) signal is collected and analysed in the SRM hut which is constructed in the same level with DR tunnel.

Table 12.19: Number of Beam Instrumentation in DR.

System	Quantity
Beam position monitor (BPM)	83
Transverse bunch by bunch feedback (FB)	1
Synchrotron radiation monitor (SRM)	1
Loss Monitor	34
DCCT	1
Bunch current monitor	1

12.7.2 Beam position monitors

BPM chamber and electrodes

The shape of the normal BPM chamber is shown in Fig. 12.72.

The lowest cut-off frequency of the monitor chamber is 2.18 GHz. Since the usable space for the BPM block is extremely tight, we employed two-in-one type BPM electrode as shown in Fig. 12.73.

Figure 12.73: Photo of the BPM feedthrough.
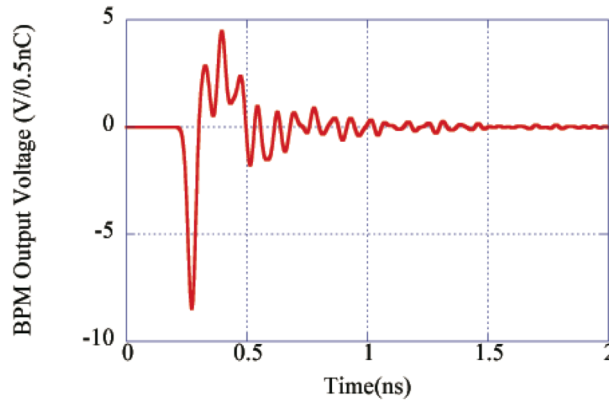
Figure 12.74: Simulated BPM output for 0.5 nC bunch charge beam using GdfidL.

The chamber will be tightly connected to the quadrupole magnet through the thick support. On the top of the BPM chamber, we prepare reference surface and a lock hole to mount the sub-reference to measure the position and the tilt of the block after the installation.

The structure of one electrode is the same as used for SuperKEKB-LER[48]. Figure 12.74 shows the simulated BPM output for the charge of 0.5 nC using GdfidL. The longitudinal and transverse coupling impedance of a BPM block (real and imaginary part) is estimated using GdfidL[49]. Most significant longitudinal impedance is about 18Ω at 14.7 GHz with $Q \sim 47$, as shown in Fig. 12.75. Though the coupling impedance is much higher than that of for SuperKEKB-LER, due to small size of the vacuum chamber, the effect to the beam will not be significant for the realistic bunch spacing and maximum beam current. Longitudinal loss factor and the transverse kick factors are summarized in Table 12.20.
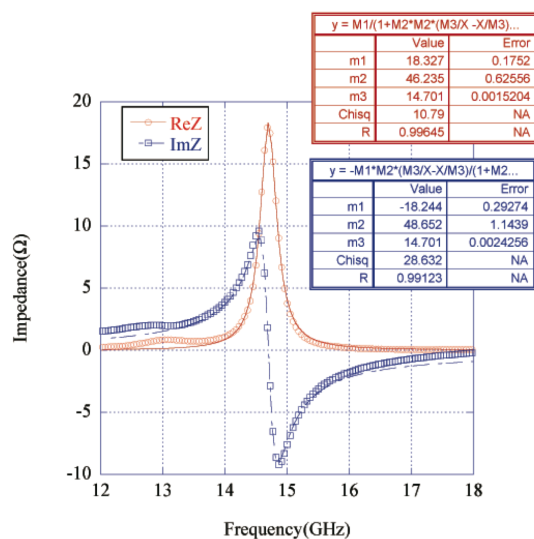
Figure 12.75: Simulated longitudinal coupling impedance of a BPM block using GdfidL.

Table 12.20: Longitudinal loss factor and transverse kick factor for the BPM block.

Name		unit
Loss factor	2.9	mV/pC
Transverse kick factor (H)	1.1	V/pC/m
Transverse kick factor (V)	0.04	V/pC/m

Position detector

As the nominal storage time of the damping ring is 40 ms, and it is desirable to distinguish the position signal between the two bunch sets that have been injected before 20 ms or will be injected after 20 ms of the bunch of interest, we have developed the wide-band turn-by-turn BPM detector based on log-ratio detection method with the center frequency of 508.9 MHz (Digitex 18K11). The form factor of the 18K11 is single-slot, double height VME64. Figure 12.76 shows the block diagram of the 18K11.

The time response of the BPF and the log-ratio amplifier has been measured using a single-bunched beam from PF-AR as shown in Fig. 12.77.

With this condition, the width of the flat-top was about 8 ns. Therefore, it is definitely needed to adjust the length of the cable within 4 ns. We plan to measure the length of the cables using TDR and calculate pre-set delays for each BPMs. The ADC timing of the boards also needs to be tuned within 4 ns. This will be done with the special digital delay system synchronized to the injected beam as shown in the latter sub-section.
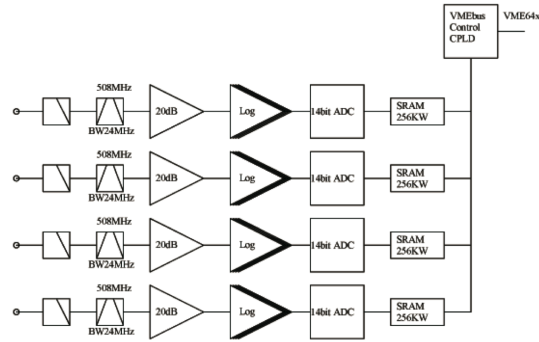
Figure 12.76: Block diagram of the turn-by-turn BPM detector based on log-ratio detection method (Digitex 18K11).
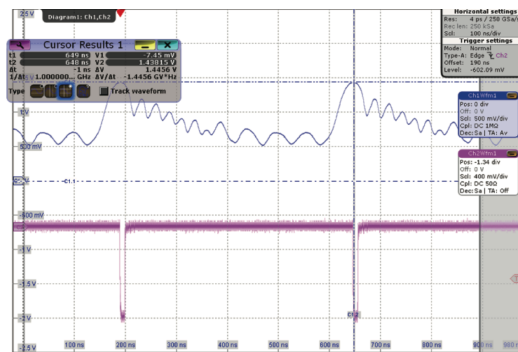
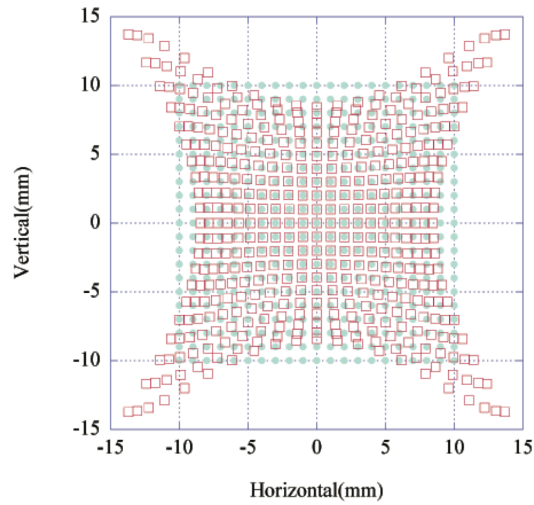Figure 12.77: Time response of the Log-amplifier using PF-AR single-bunched beam.

Figure 12.78: Result of the beam position mapping using the L/R method by the 2D-boundary element method where solid circles represent the original beam position and the hollow squares are the calculated beam positions using simple log-ratio calculation.

The calculated BPM mapping using boundary element method[51] is shown in Fig. 12.78. Even with the simple first order calculation, we will have enough linear region in the area within ±5 mm in both horizontal and vertical plane.

We will have four BPM sub-stations in the damping ring power supply building. As the total number of the BPMs are 83, each sub-station needs to handle 21 to 22 BPMs. As the nominal capacity of one VME64x sub rack is less than 21 slots, including bus master, we will use two VME64x sub rack for the BPM systems. Figure 12.79 shows the photo of twelve 18K11's in a VME64x sub rack.

We have calibrated all the channels of all the detectors using a calibrated signal

Figure 12.79: 18K11 L/R detectors in a VME64x sub rack.
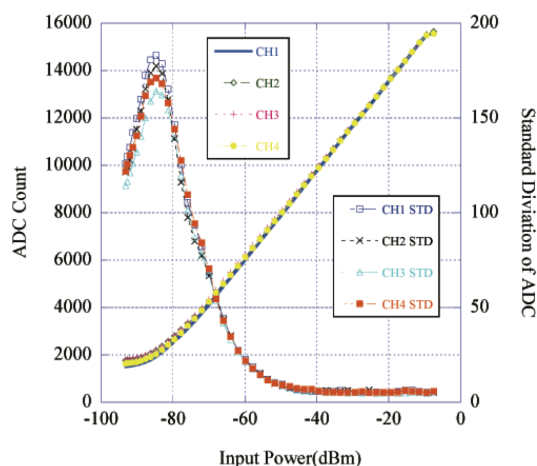
Figure 12.80: Example of the calibration of the 18K11 (SN 320).

generator and obtained the fitting curve to convert the ADC count to input power. Figure 12.80 shows an example of the result of the calibration for serial number (SN) 320.

The rough usable range of the detector is from -70dBm to -10dBm. With the charge of 4 nC of the DR, we will have the margin about 10dB. For full power operation, we will add 10dB attenuator for all the input, if needed. The jitter of the BPM output in the nominal operation will be around 10μm in horizontal plane, around 20μm in vertical plane.

To get the 2k turns or 4k turns data within 1 s for all 12 18K11s, we have implemented MBLT (Multiplexed Block Transfer) function[52] in both 18K11 and EPICS IOC. The stable data transfer within 1 s for 12 18K11s with 2k data size have been confirmed using MVME5500 IOC.

BPM timing system

Figure 12.81 shows the block diagram of the timing system for DR. It consists of mainly three parts; start trigger generation system, frequency divider with external synchronizer, and 32-channel clock delay per each station.

In the normal operation, we want to get the position data in the similar timing slot, starting with the same delay after the injection. The start-trigger also needed to be disabled during the processing time of the beam position monitor system. On the other hand, manual or continuously repeating trigger will be needed during the long storage timing mainly on the machine development time.

To realize the requirements, we have constructed a start trigger generation system
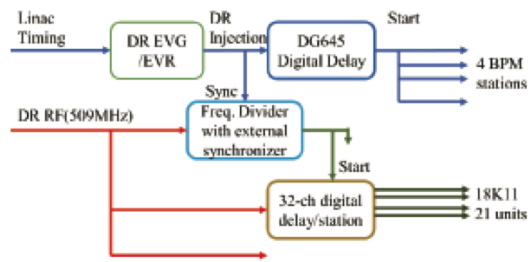
Figure 12.81: Block diagram of DR bpm timing system.

using digital delay with external trigger (SRS DG645)[50] controlled by EPICS software sequencer. We have prepared three operation modes as:

- Normal operation mode. If the status of the end node of 18K11 is ready, the sequencer enables the single shot external trigger input. Start trigger (Single Shot pulse) is initiated by the injection timing signal with pre-set delay. EPICS sequencer waits for the ready status of 18K11 and automatically re-initiate the trigger.

- Storage mode. It is similar to the normal mode but start trigger is initiated by the software timing without injection timing.

- Manual mode. Start trigger is controlled by the software. The mode will be used mainly on the special optics measurements such as dispersion measurement or chromaticity measurement where optics tool will govern all the measurement timing.

We have tested the start trigger system with the storage mode more than 6 month and had no difficulties up to now. Typical cycling time of the measurement is about 4 s where we have inserted extra 1 second of sleeping time of data acquisition to enable enough communication timing for EPICS channel access.

As the injection timing signal supplied by the linac / DR event system has enough precision with the typical timing jitter less than 10 ps, we generate the DR revolution timing synchronized to a injected bucket by re-synchronizing the frequency divider (1/230) with the injection timing. We have developed a 32-bit universal frequency divider with 32-bit clock delay and re-synchronized function (SKI-16115). Figure 12.82 shows the block diagram of SKI-16115.

It consists of a Xilinx ZC706 evaluation board and a daughter card connected with FMC connector and installed in EIA-1U case. All the functions of the board such as the set/read the frequency divide ratio, digital delay setting, enable/disable
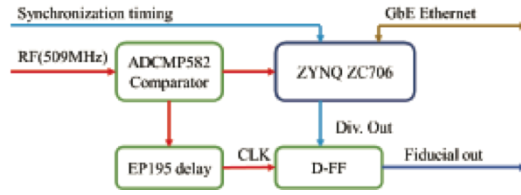
599

Figure 12.82: Block diagram of SKI-16115 universal frequency divider.

external synchronization, EP195 delay are accessible from EPICS Soft-IOC through socket communication controlled by the peta-Linux on the ZYNC FPGA.

The timing deviation and the timing jitter with the delay (RF and EPE195) change at the frequency division ratio of 230 has been measured using histogram function of Tektronix DSA8200 with 80E07 (30 GHz BW) module. The measured peak to peak deviation of the timing with the different delay setting relative to RF clock was about 4 ps with the flat timing jitter of 2.6 ps in all the delay settings.

As the design and the resources needed for the frequency divider has been established with this system, we are fabricating the new board with the same functions by employing smaller ZYNC FPGA (702) with the final form factor of NIM 1W.

From the measured cable length and the BPM placement in the ring, the fiducial timing delays for each 18K11 module have been calculated relative to the latest signal in a BPM station. Though the ring size is not large, the largest delay for two stations amounts to more than 180 ns. As it is not suitable to prepare such long delay with the change of cable length, we have decided to develop a 32-channel 32-bit digital delays (SKI-17029) also with the form factor of EIA-1U based on the code for SKI-16115 which counts RF clock (509 MHz) starting with the external timing (coming from SKI-16115) and distribute the fiducial timing for each 18K11 with the arbitrary delay with step of 2 ns. It consists of a Xilinx ZC702 evaluation board with a daughter card which has a RF comparator, 32 D-FFs and the level shifters from LVDS to PECL and PECL to NIM.

Effect of the vacuum components around BPM

Because of extremely tight spacing around BPM chamber, several vacuum components such as SR mask, ICF flange or bellows are anticipated to be installed very near to the BPM chamber. The effect of such components have been evaluated using HFSS[53] and GdfidL.

As the SR masks are designed to be in the ante-chamber part, the effect has shown less than 2% even in the case of the mask installed from 5 cm from the BPM. For the
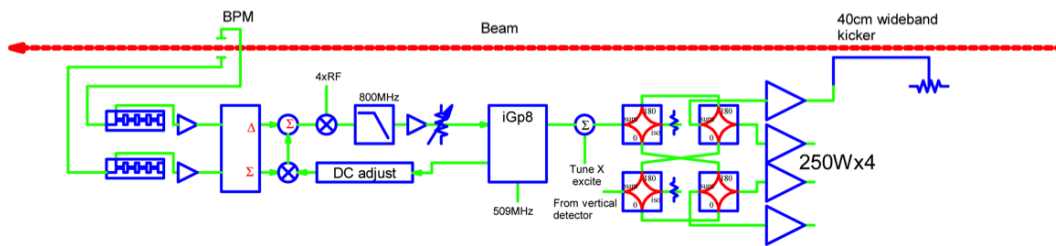
Figure 12.83: Block diagram of the transverse bunch by bunch feedback system for the damping ring.

vertical gap, such as bellows or ICF flange, objects within 5 cm is not acceptable but 10 cm might be acceptable.

12.7.3 Bunch feedback system

Since the number of bunches in the ring is less than 4 with the bunch spacing of larger than 98 ns, and the RF cavities and the vacuum components are well designed to suppress the dangerous trapped modes, no coupled-bunch instability is anticipated on the damping ring. It is nevertheless required to prepare the transverse bunch feedback system in the ring mainly to damp the transverse bunch motion due to residual kick from the injection or extraction kickers. Figure 12.83 shows the block diagram of the transverse bunch feedback system for the damping ring.

We will use the same bunch detection circuits as used in the SuperKEKB-LER and HER. Though no longitudinal feedback system will be installed in the damping ring, we will prepare longitudinal bunch position and intensity (bunch current) detection circuits. For the feedback digital filter, we will use iGp12 systems[54]. The modified firmware of the iGp12 has already been ready.

The feedback monitor chamber, DCCT and transverse feedback kicker will be installed in the north straight section upstream of the injection system. Figure 12.84 shows the drawing of the feedback monitor chamber. We use the same glass-sealing type feedthroughs used in the SuperKEKB-LER and HER[48]. Totally 20 electrodes, 16 of them are placed horizontal and vertical planes, and 4 are placed 45° from the horizontal and vertical planes.

Figure 12.85 shows the drawing of the transverse feedback stripline kicker. The length of the kicker is 40 cm. Since the size of the kicker is fairly tiny and the beam induced power will be much smaller than that of HER and LER, we employed (reverse)-N-type connector for the feedthroughs.

The beam response of the kicker has been simulated using GdfidL. Figure 12.86
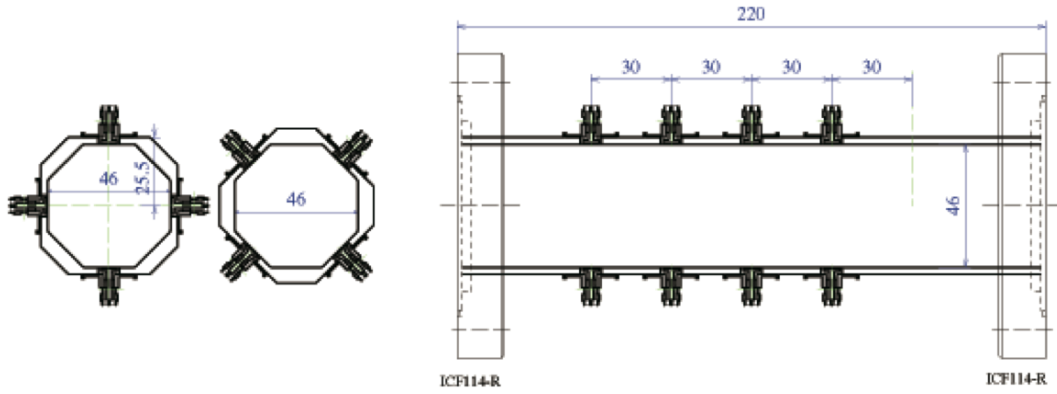
Figure 12.84: Drawing of the beam position monitor chamber for bunch feedback system.
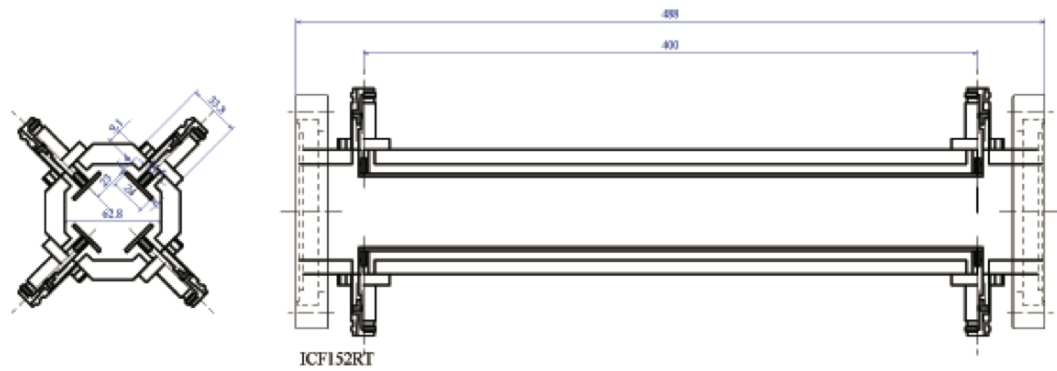

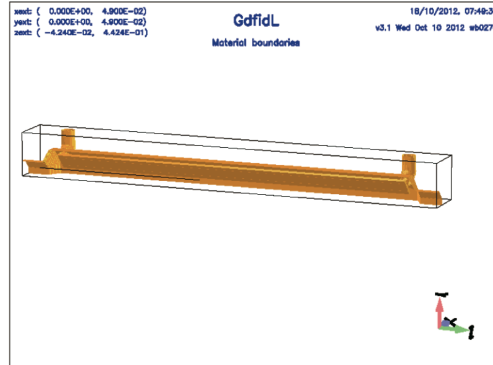Figure 12.85: Drawing of the transverse stripline feedback kicker.

Figure 12.86: GdfidL model of the transverse kicker including taper in both ends.

shows the GdfidL model of the transverse kicker.

The estimated longitudinal loss factor was 0.58 mV/pC for the bunch length of 5 mm including taper in both end. In real case, as we omit the taper at downstream end, the loss factor and the coupling impedance will be expected to be lower than that simulation.

The betatron tune and the bunch current will be measured using the similar system to the LER/HER[55]. To measure the phase advance between the BPMs, continuous betatron oscillation excitation system using PLL circuit will be installed.

We plan to use the same reflective memory system used for HER/LER on the bunch current monitor.

12.7.4   Synchrotron radiation monitor

We designed a SRM to measure a beam size [56]. Synchrotron light is extracted from a bending magnet with bending radius of 3.14m located near a straight section for beam extraction. Figure 12.87 shows the drawing of the light source magnet and SRM chamber which houses the extraction mirror. The light is led to the SRM room through a pit under a floor in a tunnel as shown in Fig. 12.88. Level of the SRM room is same as that of the tunnel in order to make propagation distance of the light as short as possible (10m). The radiation monitor is installed to the SRM room for safety since the room is near the DR extraction point and unexpected beam loss may happen.

A horizontal and vertical beam sizes at a source point of the light are 380 μm and 75 μm respectively. A bunch length is longer than 6.5mm. The transverse beam size is measured by a gated camera, and the bunch length is measured by a streak camera. The setup of these cameras are shown in Fig. 12.89.
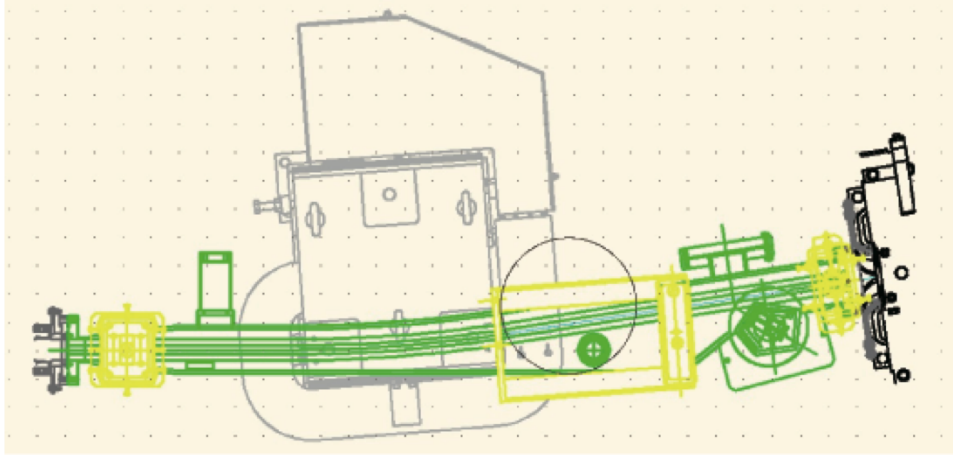
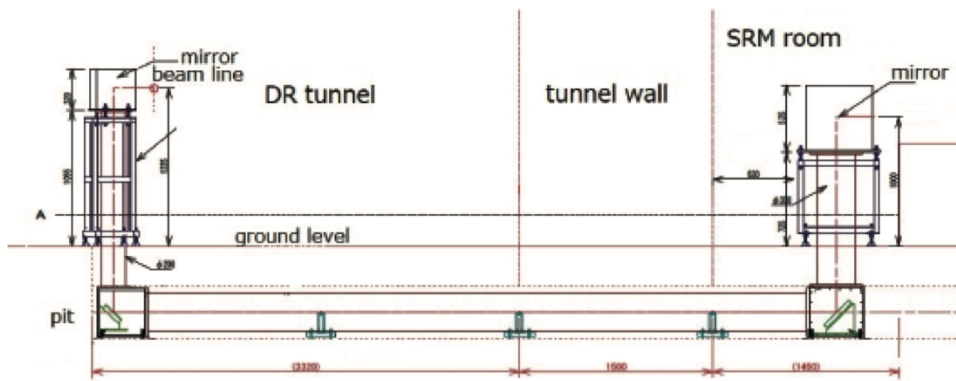Figure 12.87: Drawing of the DR SRM chamber.

Figure 12.88: Layout of the DR SRM line.

Figure 12.89: Layout of the DR SRM hut.

Resolution of the beam size measurement depends on diffraction of the light. The opening height of the extraction chamber is 8 mm at 590 mm downstream from the light emission point. Diffraction patterns calculated by following Fraunhofer formula [57] are shown in Fig. 12.90(a),

$$F(x,y) = (\frac{\sin(2\pi ax/\lambda L)}{2\pi ax/\lambda L})^2(\frac{\sin(2\pi bx/\lambda L)}{2\pi bx/\lambda L})^2, \qquad (12.28)$$

where a and b are opening size of the x and y direction, L is the distance from emission point to extraction point of SR and λ is the wavelength. Figure 12.90 (b) shows the convolution of the quantum efficiency of the camera and the Fraunhofer diffraction pattern at $\lambda = 200nm - 900nm$. We get 12 μm resolution by Gaussian fit of the convoluted distribution. This is small enough in comparison with beam size. The longitudinal resolution is 1psec that is caused by the measurement accuracy of the streak camera.

The extraction mirror of SR is a Beryllium mirror which we used in KEKB. When the power to the mirror is too large, it may cause the deformation of the mirror [58]. Emission power per unit angle and the total radiation power from the magnet are calculated by the following expression [59],

$$\begin{pmatrix} \frac{d^2P_\sigma}{d^2\Omega} \\ \frac{d^2P_\pi}{d^2\Omega} \end{pmatrix} = \left[\frac{7}{64\pi}\frac{e^2}{\varepsilon_0}\frac{\gamma^5}{\rho}\frac{I}{e}\right]\frac{1}{(1+\gamma^2\psi^2)^{5/2}}\begin{pmatrix} 1 \\ \frac{5}{7}\frac{\gamma^2\psi^2}{1+\gamma^2\psi^2} \end{pmatrix}[W/rad^2], \qquad (12.29)$$

$$\begin{pmatrix} P_\sigma \\ P_\pi \end{pmatrix} = \frac{2}{3}\frac{e^2}{4\pi\varepsilon_0}\frac{I}{e}\frac{\gamma^4}{\rho^2}\begin{pmatrix} \frac{7}{8} \\ \frac{1}{8} \end{pmatrix}[W], \qquad (12.30)$$

605
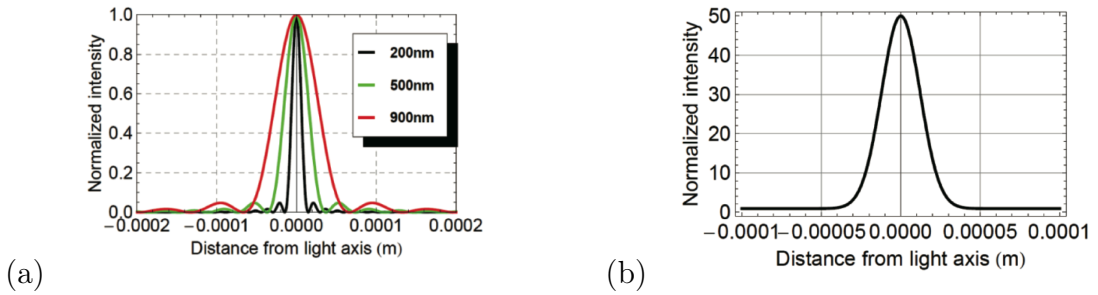
Figure 12.90: (a) A pattern of the Fraunhofer diffraction at the extraction mirror of the SR with   = 200nm, 500nm and 900nm. (b) The convolution of the quantum efficiency of the camera and the Fraunhofer diffraction pattern of   = 200nm - 900nm.
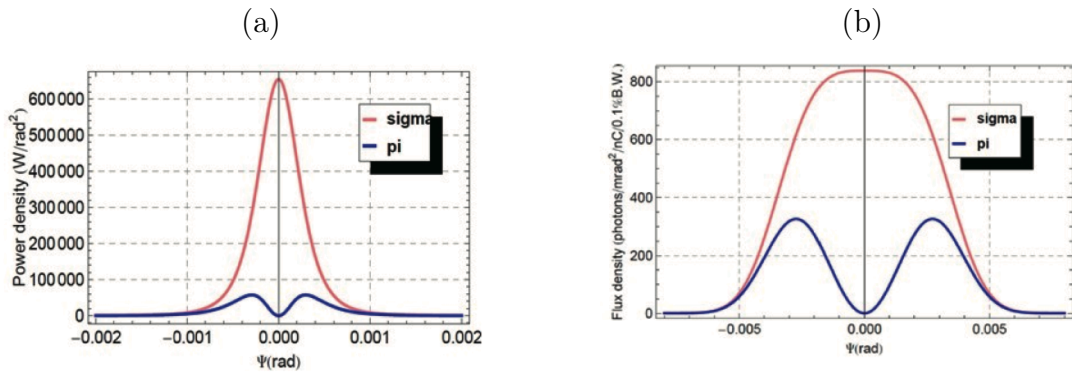

Figure 12.91: σ component and π component of (a) the emission power density and (b) spectral angular density of flux [photons/s/rad2/0.1 %band width/A] from the bending magnet.

where I is beam current, e is the electric charge, ε_0 is the vacuum dielectric constant, ρ_E is radius of the bending magnet, and is the orbital length. The result is shown in Fig. 12.91 (a) when we calculate with DR parameters. The total power is 70.5W when the maximum current is injected to DR. The power to the extraction mirror is 17.9W. We can provide the mirror and mirror cooling system used in KEKB. Figure 12.91 (b) shows the spectral angular density of the flux in the DR SRM. It is 2.99E+5[photons/0.1 % band width/nC] for a wavelength 550 nm used for the measurement and the band width of 0.1 % in DR. The measurement in DR is possible down to 0.1 nC bunch which emits photons of the same level as that from 5nC bunch of KEKB LER.

12.7.5   Beam loss monitor

The DR LM is not used for an interlock signal giving a beam abort. It is used for commissioning, injection tuning and monitoring in routine operation. The maximum beam current is 70 mA which corresponds to 8nCx4bunch accumulation. As for the injection efficiency of DR, the normal beam loss is estimated to be 2.5 % near the injection point and 2.7 % in all other arc sections. On the other hand, around 20 % of loss is expected in a collimator part. It is necessary to have enough sensitivity when loss more than expected happens.

Ion chambers which are shown in Fig. 12.92 are reused sensors that are used for the KEKB linac. It is a 9 m and 1 m FC-20D co-axial cable. The inner and outer conductors are separated by an air gap. A positive potential of 200 V is applied to the outer conductor to collect the electrons. The positive ion is collected to the inner collector with typical drift time of 1 ms. The 9 m IC's are mounted on the cable rack or the wall in the DR and LTR/RTL tunne as shown in Fig. 12.93 . Especially, the 1m IC's are attached to the down stream of extraction septum magnet in order to check the extraction beam condition. Read-out electronics is same as that used in MR [60]. That consist of an integrator and an amplifier. The amplifier gain is selected to 1, 10 and 100. The IC is sensitive down to the loss of around 0.1 mA/s. The signal is sent to ADC which is developed for the DR and MR LM and logged in SuperKEKB logging system. Pin photo-diodes and optical fibers are also installed to check the beam loss situation in detail as backup.

12.7.6   Beam current measurement

Spare DCCT for KEKB-HER/LER is installed in the damping ring. As the nominal storage time is short, we will install fast digitizer with the sampling frequency of 5 kHz.
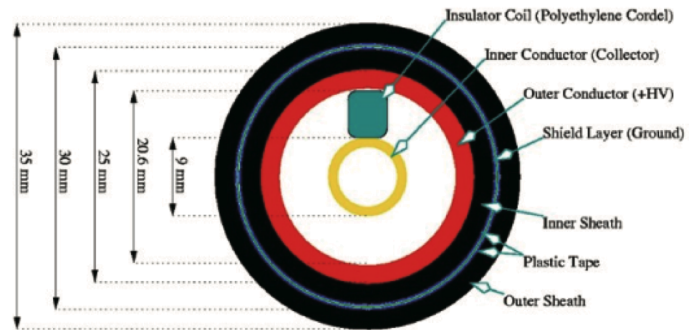
Figure 12.92: Cross section of the ion chamber for the beam loss monitor..

Figure 12.93: Ion chamber that mounted on the cable rack.

Expected resolution is about 30 μA at less than 200 mA beam current.

We do not install CT in the damping ring. For the first injection information, we extract 508 MHz component from the signal of FB button electrodes and down convert to base band signal.

12.8   Beam transport

12.8.1   Overview of Beam transport

Table 12.21: Required parameters of injection beam for SuperKEKB-LER in Phase 2 and 3

	DR Extraction	Phase2	Phase3–
$\gamma\epsilon_x$ [μm]	64.3	< 200	< 100
$\gamma\epsilon_y$ [μm]	3.2	< 40	< 15
σ_δ [%]	0.055	0.16	0.10
Charge [nC]	1.5	1.5	4.0

The required parameters for the positron injection beam of SuperKEKB-LER are shown in Table 12.21. It should be noted that these values are defined as "ultimate" parameters in each stage that should be realized in harmony with a development of collision performance.

As shown in Figure 12.94, the DR, a 1.1-GeV storage ring with a circumference of about 135.5 m has been constructed at 120 m downstream of the positron target of the linac. The positron beam is extracted from the end of Sector 2 of the linac whose energy is 1.1 GeV, and injected into the DR. Since the enormous energy spread from the flux concentrator (FC) exceeds the energy acceptance of the DR, an energy compression system (ECS) is installed utilizing the first arc of the LTR. The optical functions from the positron capture section to the end of the LTR are shown in Figure 12.95. The damped beam from the DR is returned to the entrance of Sector 3 of the linac. The acceleration frequency of the DR is about 508.9 MHz, which is same as that of SuperKEKB, the resulting bunch length is too long to be accepted to the linac with acceleration frequency 2856 MHz (S-band). Thus a bunch compression system (BCS) in the second arc of RTL is installed [61, 62, 63]. The optical functions from the RTL to the end of the injection point for the LER are shown in Figure 12.96. One more ECS is installed at the end of the linac to ensure that the energy spread of the beam from the linac is compressed within the LER energy acceptance.
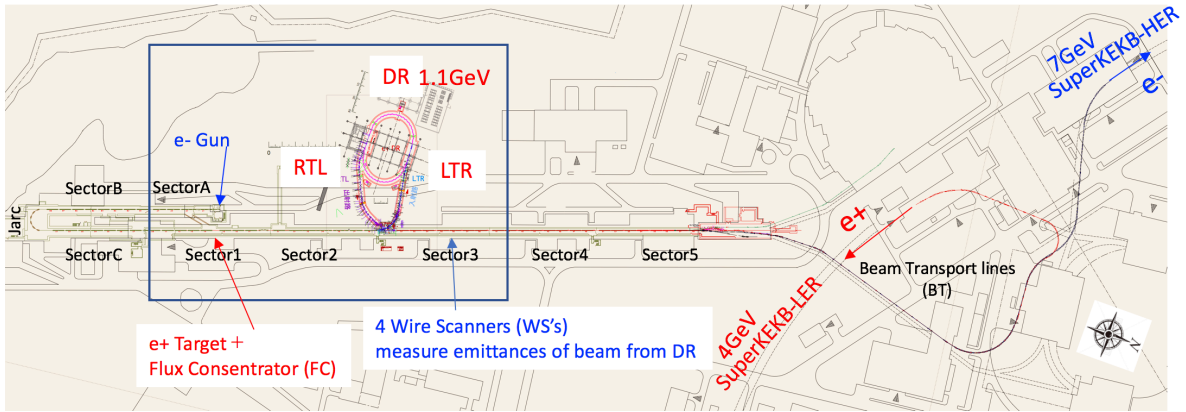
Figure 12.94: The linac consists of eight sectors from Sector A, B, C, and 1 to 5 starting from the electron sources. The electron and positron beams are accelerated up to 7 GeV and 4 GeV, respectively, and are injected into the HER and the LER of SuperKEKB via each beam transport line (BT). Both of the injection/extraction lines (LTR/RTL) for the damping ring (DR) have two arc sections with straight sections between them.
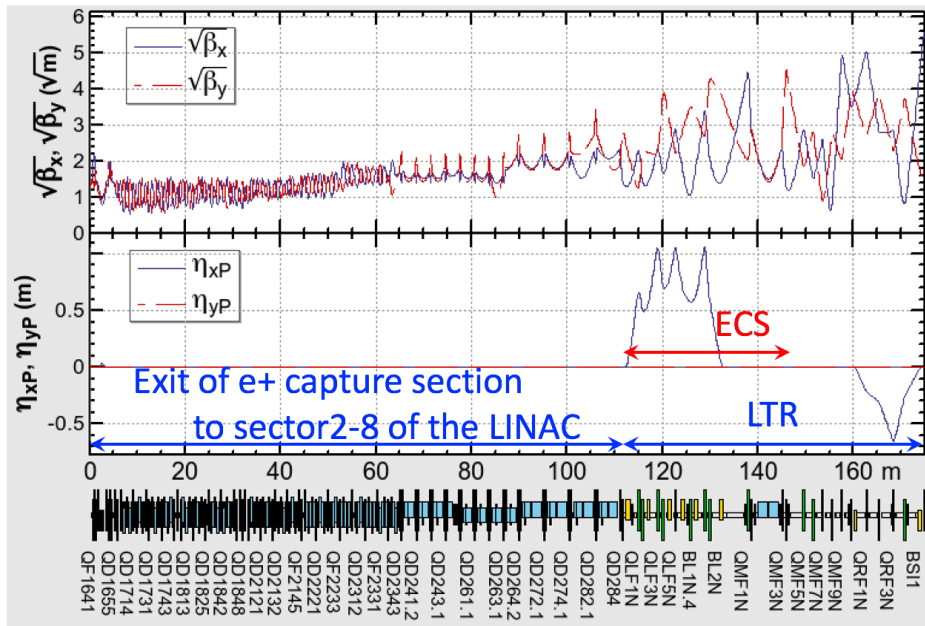

Figure 12.95: Optical functions from the positron capture section to the end of the LTR. The upper and lower figure show beta functions and dispersion functions, respectively.

Figure 12.97 shows the particle distribution before and after the DR in the longitudinal phase space simulated with the parameters on Table 12.22. The parameters of the DR have been modified from the design [64, 65] to match the changes in the
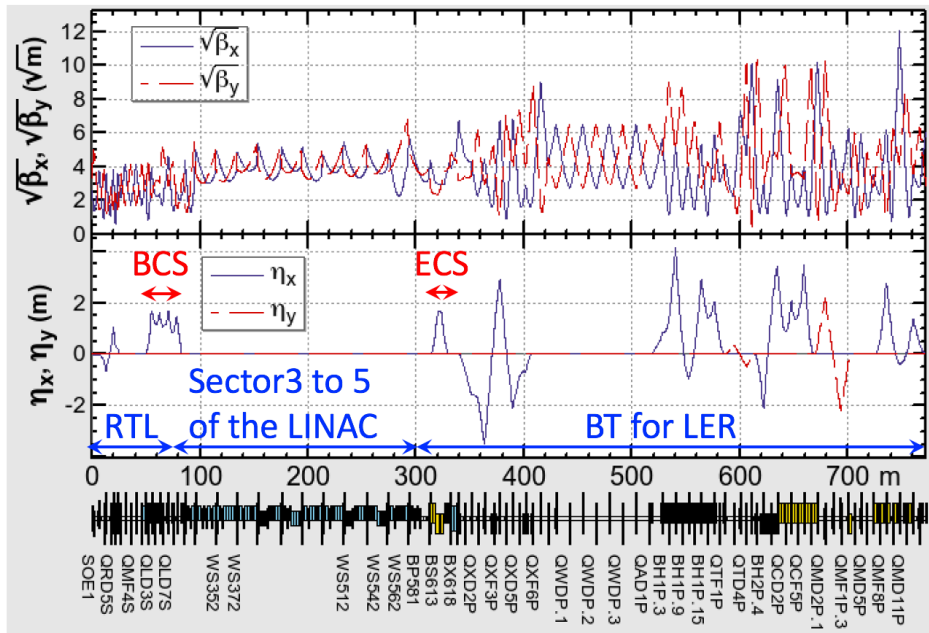
Figure 12.96: Optical functions from the RTL to the end of the injection point for the LER. The upper and lower figure show beta functions and dispersion functions, respectively.
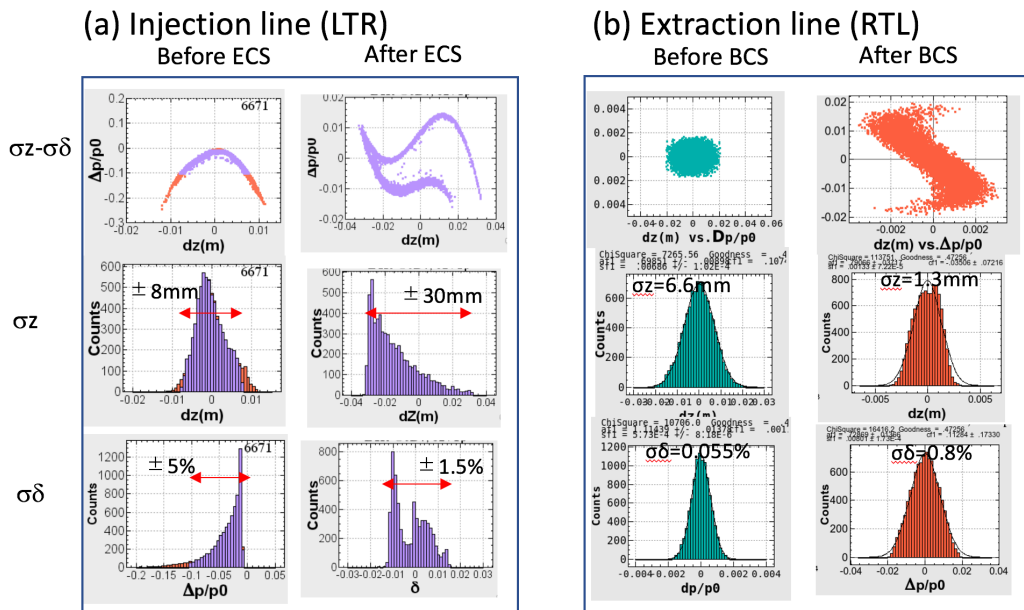

Figure 12.97: Simulated distributions of longitudinal phase space before and after (a) ECS and (b) BCS.

RF voltage from the design value of 1.4 to 1.0 MV, hence the emittance accordingly changed from 89 μm to 64.3 μm.

Table 12.22: Design parameters of the injection and extraction beam for the DR (* means a full width shown by red arrows in Fig. 12.97.) Twiss parameters with a symbol (av.) are calculated using beam sizes, while those with a symbol (TM) are deduced from the optimized parameters of R_{56} and V_c, assuming a linear transfer matrix.

Parameters	ECS		BCS	
	in	out	in	out
$\gamma\varepsilon_x$ [μm]	2800		64.3	
$\gamma\varepsilon_y$ [μm]	2600		3.2	
σ_z [mm]	$\pm 8^*$	$\pm 30^*$	6.6	1.3
σ_δ [%]	$\pm 5^*$	$\pm 1.5^*$	0.055	0.8
α_z (av.)	0	-0.52	0	1.4
β_z (av.) [m]	0.16	2.25	12	0.16
Compression rate	0.30		0.20	
R_{56} [m]	-0.61		-1.05	
V_c [MV]	41		21.5	
α_z (TM)	0	-1.73	0	3.2
β_z (TM) [m]	0.16	2.49	12	0.71

Since positrons from the FC have a long energy-tail, as shown in Fig. 12.97-(a), which cannot be accepted in the DR even with ECS, four collimators are installed in the arc section of the LTR to prevent the tail particles with an energy deviation larger than 5% from passing through the LTR. The energy spread of remaining particles is compressed to $\pm 1.5\%$, the DR bucket height. Because the bunch length of the beam in the ECS and BCS is also too long to be accommodated with the frequency of S-band, an nonlinear effect of RF curvature is visible in the figures named "After ECS" or "After BCS" in Fig. 12.97. With the parameters (R_{56}, V_c) as in Table 12.22, the beam can be transported without notable loss.

The transfer matrix of the ECS is expressed as follows;

$$\begin{pmatrix} 1 & 0 \\ k & 1 \end{pmatrix} \begin{pmatrix} 1 & R_{56} \\ 0 & 1 \end{pmatrix} = \begin{pmatrix} 1 & R_{56} \\ k & 1 + R_{56}k \end{pmatrix}, \tag{12.31}$$

where $k = -\dfrac{V_c}{E_0}\dfrac{2\pi f_{rf}}{c}\mathrm{sgn}(R_{56})$. The symbols V_c, E_0, f_{rf}, and c mean cavity voltage, the beam energy, RF frequency of the cavity, and a speed of light, respectively. Generally, the transfer matrix of the beam transport between point 1 and 2 is written using

longitudinal Twiss parameters as;

$$M = \begin{pmatrix} \sqrt{\frac{\beta_2}{\beta_1}} \cos\phi & \sqrt{\beta_1\beta_2} \sin\phi \\ -\frac{1}{\sqrt{\beta_1\beta_2}} (\sin\phi + \alpha_2 \cos\phi) & \sqrt{\frac{\beta_1}{\beta_2}} (\cos\phi - \alpha_2 \sin\phi) \end{pmatrix}, \tag{12.32}$$

where $\alpha_1 = 0$ is assumed. Comparing the (1,1) and (2,1) components of Eq. (12.31) and (12.32), we get

$$k = -\frac{1}{\beta_2} \left(\sqrt{\frac{\beta_2}{\beta_1}} - 1 + \alpha_2 \right), \text{ and } R_{56} = \sqrt{(\beta_2 - \beta_1)\beta_1}. \tag{12.33}$$

The beta functions can be identified using equations,

$$\beta_1 = \frac{\sigma_{z1}}{\sigma_{\delta 1}}, \text{ and } \frac{\sigma_{\delta 2}}{\sigma_{\delta 1}} = \sqrt{\frac{\beta_1}{\beta_2}(1 + \alpha_2^2)}. \tag{12.34}$$

For the case $\alpha_2 = 0$, from σ_z, σ_δ before ECS and σ_δ after ECS in Table 12.22, following parameters can be calculated: $\beta_1 = 0.16$ m, $\beta_2 = 1.78$ m, $k = -1.79$, $R_{56} = -0.509$ m, and, $V_c = 32.9$ MV. With these parameters, however, due to the RF nonlinearity, sizable amount of particles in the energy tails extend over the energy aperture of $\pm 1.5\%$. The phase space plot in the Figure. 12.98-(a) tells the situation.

We have to seek the optimum values of parameters through tracking simulations, which were obtained with a simulation, by scanning the ECS parameters of R_{56} and V_c to minimize the energy spread of the particles at the exit of the system. The initial particles were generated with the electromagnetic shower code EGS4 in the six-dimensional phase space, and they were tracked with the SAD code from the positron capture section, through Sector 1 and 2, to the entrance of the LTR. We found optimum values of V_c=41 MV and $R_{56} = -0.61$ which compress the entire energy distribution within the bucket height as shown in Fig. 12.98-(b).

Twiss parameters are deduced from R_{56} and V_c with equations,

$$\beta_2 = \beta_1 + \frac{R_{56}^2}{\beta_1}, \tag{12.35}$$

$$\alpha_2 = -\beta_1 k - \frac{(1 + kR_{56})R_{56}}{\beta_1}, \tag{12.36}$$

$$\tan\phi = R_{56}/\beta_1, \tag{12.37}$$

and we obtain $\beta_1 = 0.16$ m, β_2(TM)=2.49 m, α_2(TM)=-1.73 and ϕ(TM)= $-75.3°$.

On the other hand, the parameters β_2 and α_2 are calculated from the beam sizes
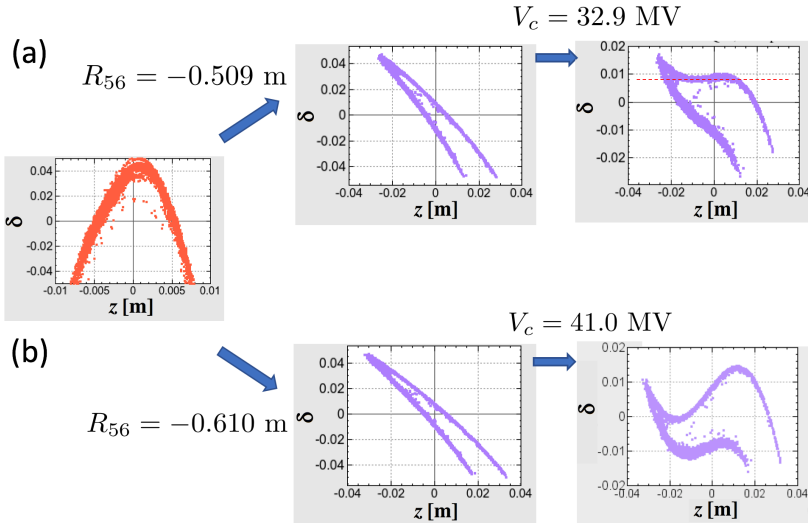
Figure 12.98: The simulated longitudinal distributions in the ECS. The left, center, and right figures show the phase space plots at the entrance of the ECS, after the 1st arc section of LTR and after the RF cavity, respectively. (a) The graphs show the plots with calculated $R_{56} = -0.509$ m and $V_c = 32.9$ MV assuming all distributions of particles is gaussian. (b) The graphs show the plots using optimized parameters, $R_{56} = -0.610$ m and $V_c = 41.0$ MV for particles with non-Gaussian distribution.

with the following equations,

$$\beta_2 = \frac{\sigma_{z2}^2}{\sigma_{z1}\sigma_{\delta1}}, \tag{12.38}$$

$$\alpha_2 = -\sqrt{\left(\frac{\sigma_{z2}\sigma_{\delta2}}{\sigma_{z1}\sigma_{\delta1}}\right)^2 - 1}, \tag{12.39}$$

and we obtain β_2(av.)=2.25 m and α_2(av.)=-0.52 as shown in Table 12.22.

The transfer matrix of the BCS is expressed as follows;

$$\begin{pmatrix} 1 & R_{56} \\ 0 & 1 \end{pmatrix} \begin{pmatrix} 1 & 0 \\ k & 1 \end{pmatrix} = \begin{pmatrix} 1 + R_{56}k & R_{56} \\ k & 1 \end{pmatrix}. \tag{12.40}$$

The definition of the symbols is the same as that in Eq.(12.31). The parameters calculated with Eq.(12.40) are shown in Table 12.22.

The bunch length of the extracted beam from the DR is compressed from 6.6 mm to 1.3 mm with the BCS. As shown in Figure 12.99-(a), the bunch length at the end of the RTL is compressed to its minimum for the RF voltage of the BCS, V_c =18.4 MV. However, we adopted V_c of 21.5 MV, since the energy spread as well as the bunch length at the injection point to LER is minimized with this value, owing to gymnastics
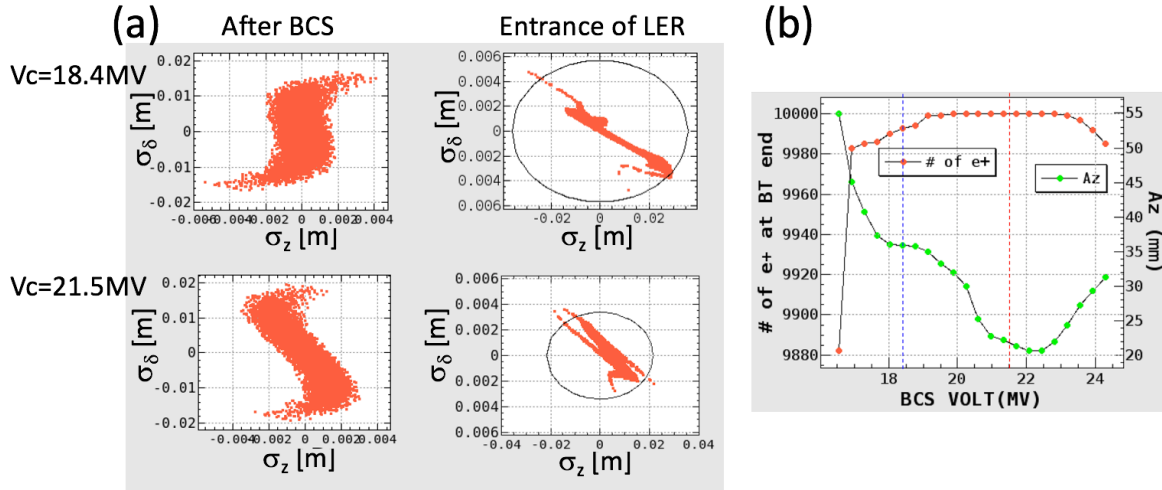
614

Figure 12.99: Simulated distribution of the longitudinal phase space in the BCS. (a) The left and right figures show the distributions at the end of the BCS and at the injection point of LER, respectively. The upper and lower figures show those with the BCS Voltage of 18.4 MV and 21.5 MV, respectively. (b) Red and green points show the number of positron that reach the end of BT and the longitudinal emittance, respectively as a function of BCS voltage. The inital number of particles is 10,000.

in the longitudinal phase space of the downstream. Figure 12.99-(b) shows that at 21.5 MV all of positrons can reach the end of BT while the longitudinal emittance is at minimum.

In the next subsection, designs for the subsystems will be described in detail.

12.8.2 From the positron target to DR

Figure 12.100 shows the schematic layout of the system from the positron target to the DR together with the longitudinal phase space at primary locations. The energy and charge of the primary electron beam are 3.5 GeV and 10 nC at the target. The positron target is made of a 14 mm-thick-Tungsten block. The crucial point in the design of the positron capture section is to maximize the capture efficiency by enlarging the energy acceptance as well as the transverse acceptance. For the energy acceptance, the adiabatic matching device (AMD) is used, though it tends to generate a long energy-tail in the lower energy side. In SuperKEKB, a flux concentrator (FC) is adopted as the AMD. For the transverse acceptance, acceleration structures with large aperture are indispensable. While an *L-band* structure would be the best solution, a *Large-aperture S-band* is another option, which will be discussed in the next section. The subsequent linac with S-band structures boost the energy from 120 MeV to 1.1 GeV.

615

Owing to the large transverse acceptance of the linac, the normalized emittance of the beam generated with the FC amounts to 2800 μm before the DR. The distributions in the longitudinal phase spaces are shown in the upper part of Fig. 12.100. Since the energy spread, especially its low-energy tail, is so huge compared to the DR's acceptance of $\pm 1.5\%$, it is necessary to cut the tail and to compress the energy spread prior to injection to the DR. Collimators play an important role to prevent particles from being injected that will be eventually lost in the DR. By truncating the energy tail by collimators, the energy spread decreases to $\pm 5.0\%$ at the entrance of the ECS.

Simulation study has been performed using various codes; EGS4 for the positron generation; a newly developed code that simulates the capture process in the capture-section; SAD[66] for the acceleration and beam transport.

As for the capture-process there are two major points in the design: one is the phase of the RF (acceleration or deceleration), and the other is the acceleration frequency (*L-band* or *Large-aperture-S-band*).

RF Phase of the Capture Section

The energy spread of the positrons right after the target is very broad. In the "acceleration phase", the generated positrons move on a crest of RF wave, and accelerated as usual. In the case of a "deceleration phase", the positrons are once decelerated to almost zero velocity then caught up by the next RF wave, and accelerated again. The particles in the higher energy tail, taking longer time to be decelerated, catching up the next RF wave with later timing, gains lower energy than the center particles do. Figure 12.101 illustrates the difference between them. In the acceleration phase there
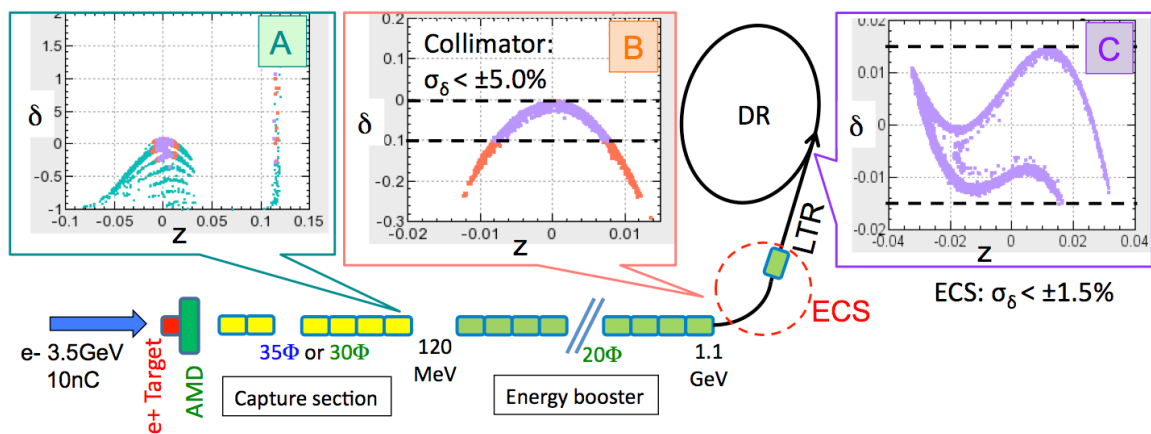

Figure 12.100: The schematic layout of the system from the positron target to the DR with distributions in the longitudinal phase space: [A] at the end of the capture section, [B] at the extraction point from the linac, and [C] at the entrance of DR.
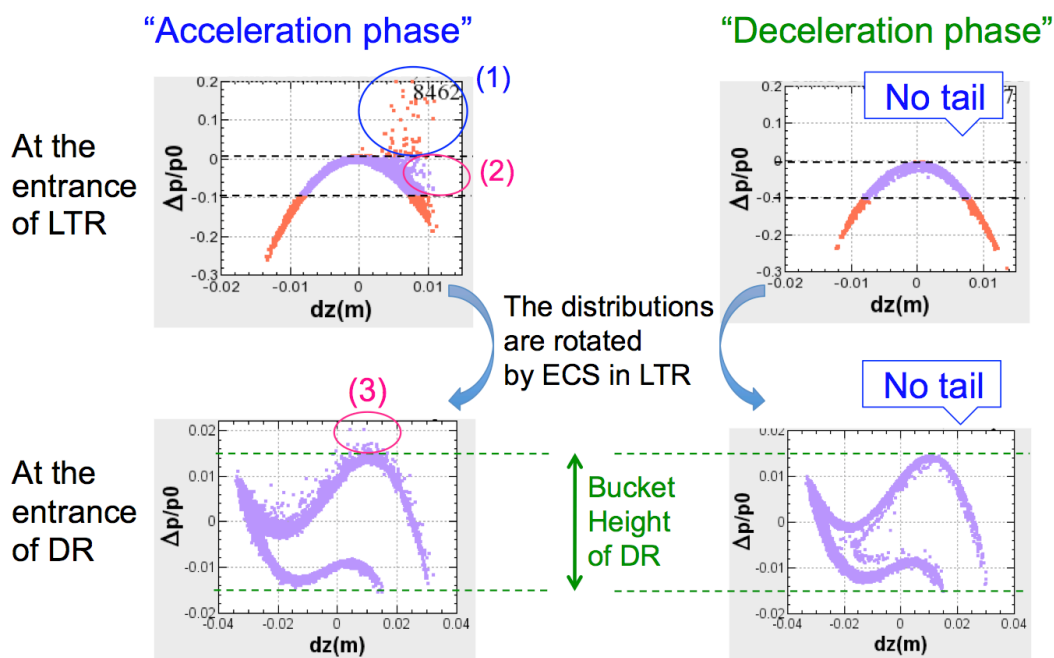
Figure 12.101: Comparison of longitudinal phase space for the acceleration case(left) and the deceleration (right). The upper (lower) figures show the distributions at the entrance of LTR (DR).

are tail particles at the higher energy at the entrance of LTR, see particles in the circle (1) in Fig. 12.101. Even if the collimators cut the tail at the LTR, there could still exist the other tail in the positive z-direction (2). After rotation in the longitudinal phase space by the ECS, the tail at the z-direction emerges as a new high-energy tail (3), which is no longer trimmed because no high-dispersion section exists after the ECS. In the deceleration phase, in contrast, there is no tail in the energy direction nor z-direction at the entrance of LTR, all positrons after the collimators are injected within the acceptance of DR[67].

While the intensity of the positrons injected to the DR has no significant difference between the acceleration and the deceleration phases(about 6 nC), we have chosen the deceleration phase from the viewpoint of the energy tail.

Accelerating Structure of the Capture Section

Larger apertures in the capture section is obviously preferable to capture more positrons. From this viewpoint, an L-band structure with a large aperture of 35 mmϕ, would be the best solution, however, considering costs, an S-band structure with large-aperture, say, 30 mmϕ, might be a candidate. Tracking simulations show that the charges that reach the DR are comparable for L-band and S-band; 6.6 nC and 6.3 nC, respectively.
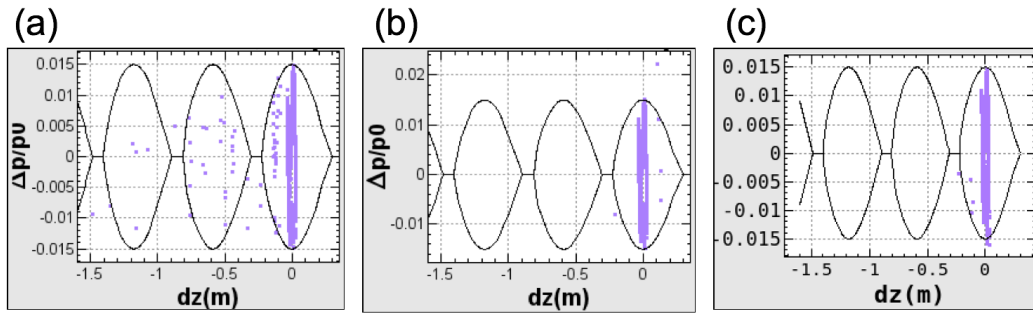
617

Figure 12.102: Distributions in the longitudinal phase space at the injection point of the DR. The lines show the separatrix of the DR. The accelerator frequencies of the capture section are; (a) all S-band, (b) a combination of L-band and S-band, and (c) *LAS* and S-band with optimization of the RF voltage in the capture section.

As shown in Figure 12.102-(a), for the S-band's, satellite bunches are generated due to circuitous trajectories in the solenoid field of the capture section. These satellites could cause a beam loss in the DR after injection. As we have to reuse the existing S-band linac as much as possible, the downstream accelerating structures must be S-band. In the L-band case, by choosing a coprime (5:11) frequency ratio of L-band to S-band, 1,298 MHz to 2,856 MHz, most of the L-band satellites drop into deceleration phase of the following S-band or less accelerated, and are eliminated by the physical aperture of the structure (See Fig. 12.102-(b).) at the end. The beam loss ratio in the DR is estimated as 0.403% and 0.053% for S-band and L-band, respectively. Since the maximum allowable loss rate is 0.1% in the DR, the use of L-band seems inevitable. However, as shown in Fig. 12.102-(c), it was found that the S-band with large aperture (*LAS*) can reduce the number of satellite particles by shortening the drift spaces between the accelerating tubes in the capture section, and by increasing the voltage of the first two accelerating tubes.

The reason why this works is understood as follows. To increase the injection efficiency of the positrons, they are injected on the decelerating RF phase as mentioned the previous section. The most of the positrons shift to the accelerating RF phase by the phase slip in the first accelerating structure and that becomes the main bunch. The positrons which has an energy with slightly higher than the energy gain in the first accelerating structure have low velocity ($\beta<1$) at the exit of the accelerating structure. Thus, those positrons reach the second accelerating structure several RF cycles behind the main bunch and becomes satellite bunches. The amount of the satellite bunches depends on the strength of the field in the first accelerating structure and the distance between the first and the second accelerating structure. It is confirmed that the production rate of satellite with over 16 MV/m of the accelerating field is less than 50%

618

than that of 10 MV/m. Beam loss in the damping ring is shown in Figure 12.103, by using the simulation codes GEANT, the GPT, and the SAD. Although the higher voltage looks better, we chose 16 MV which is the highest available voltage at this moment. The acceleration voltage at the downstream is 10 MV.

12.8.3   From the DR to the main ring

Figure 12.104 shows a layout of the linac and beam transport lines from the DR to the main ring. The extracted low-emittance beam must be transported to the entrance of the main ring without emittance growth. After the DR, the bunch length is reduced
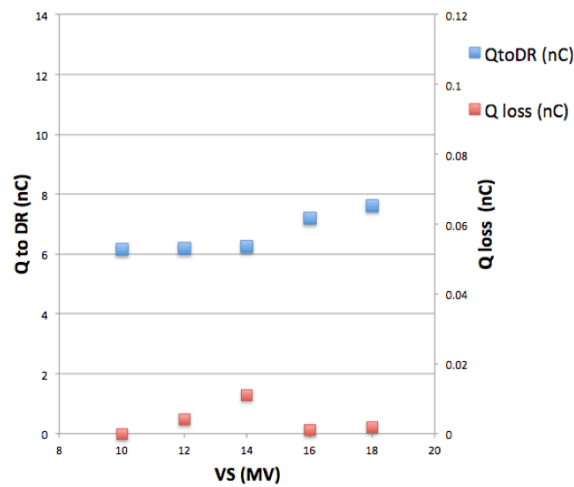
Figure 12.103: The horizontal axis is the voltage of the first two accelerator structures of the positron capture section. The blue points show the charge into the DR. The red points show the charge lost in the DR.
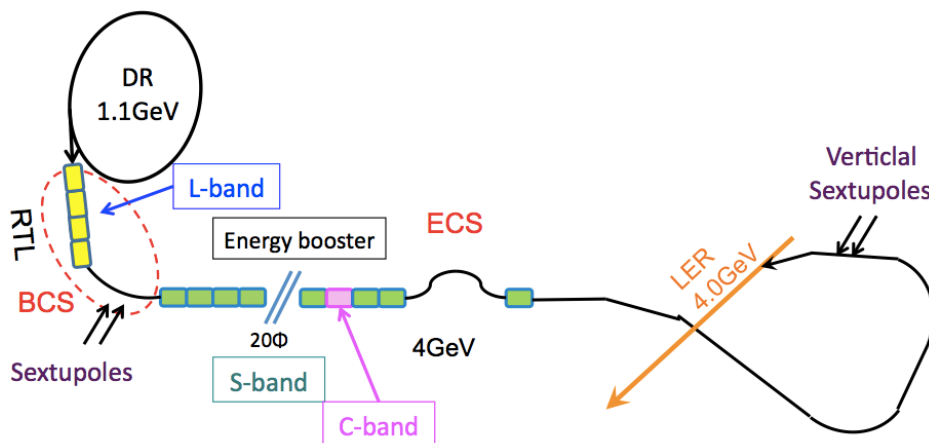

Figure 12.104: A schematic layout of the linac and the beam transport line from the DR to the main ring.

by one order of magnitude through the BCS to cope with the RF curvature of the downstream linac. For the simulations in this section we used L-band structures for the RTL and a few C-band structures in Sector 4, which are abandoned in the final design. To match the long bunch-lengths, it is best to use an L-band accelerator structure for BCS. There is another ECS at the end of the linac in order to match the beam with the momentum acceptance of the main ring.

Transporting the high bunch-intensity of 8 nC after the DR, various sources of emittance growth are conceivable :

1. Blowup of the energy spread due to mis-phasing of accelerating structures

2. The transverse emittance blowup due to;

   (1) transverse wake of accelerating structures,

   (2) second-order dispersion in the transport lines,

   (3) synchrotron radiation in the transport line

Enlargement of the Energy Spread

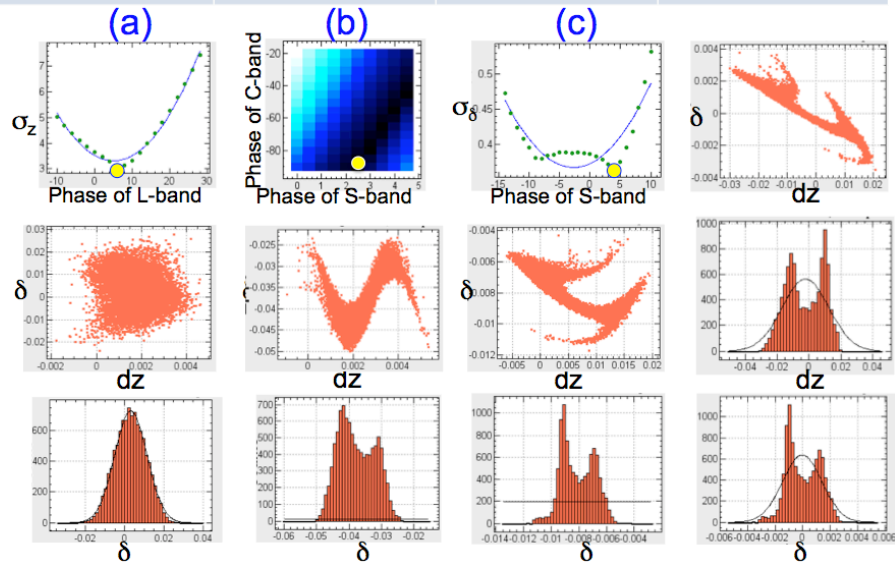| Tuning knob	L-band of BCS	S,C-band in LINAC	S-band of ECS	
Place	Entrance of LINAC	End of LINAC	Exit of ECS	Entrance of main ring
σ_z [mm]	±0.896	±2.15 (99% incl.)	±10.87 (99% incl.)	±21.93 (99% incl.)
σ_δ [%]	±0.825	±1.13 (99% incl.)	±0.271 (99% incl.)	±0.271 (99% incl.)

Figure 12.105: Optimization of acceleration phase to minimize the energy spread

In acceleration of high bunch-intensity of 8 nC, a strong wake field of accelerating structure has a sizable effect on the beam. To simulate the effects, a wake potential

620

by Yokoya's approximated formula[68] is included in the simulation. The RF-phase at three parts of accelerating structures was adjusted to minimize the energy spread in each section, which mimics the process in the actual beam operation, with the result shown in Figure 12.105; (a) L-band in the BCS, (b) S-band and C-band in the linac, and (c) S-band in the ECS.

Fig. 12.105 shows the results after the phase adjustment. The bunch length dependence on the phase is approximated well with parabola except at the bottom in Fig. 12.105-(c), which is a manifestation of the non-Gaussian distribution. At the LER the energy spread is $\pm 0.271\%$ in full width and the bunch length in full width is ± 21.9 mm, which are well within the longitudinal acceptance of the LER.
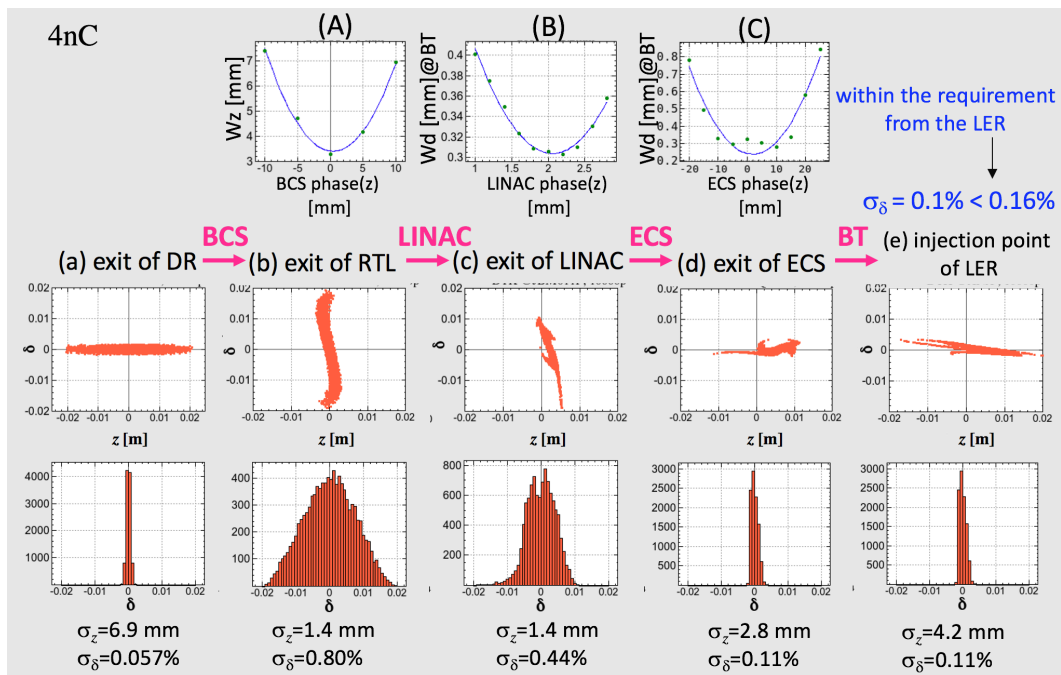

Figure 12.106: Optimization of acceleration phase to minimize the energy spread assuming 4 nC. Upper graph: [A] BCS phase optimization by bunch length of the RTL exit, [B] Optimization of acceleration phase of Sector 3-5 of the linac by energy spread of injection point, [C] ECS phase optimization by energy spread at the injection point. Middle plot: Particle distribution at each location in the longitidinal phase space after optimization. Lower histogram: Energy spread in each place.

Simulations were performed with more realistic parameters. After the simulation study described above, it is decided to replace the L-band in the RTL and the C-band in the Sector 4 with the S-band, because the similar simulation showed that the positrons from DR are safely transported and injected into the LER as shown in Fig. 12.99. The optimizations of the RF phases should be done to minimize the energy spread at the end of the BT as well as in Sector 3-5 in the linac. The results of the distributions are

shown in Figure 12.106. The ECS at the end of linac compresses the energy spread to about a quarter.

Transverse Emittance Growth

   Misalignments   Off-centered orbit in the accelerating structures can induce the transverse instability due to a transverse wake field.
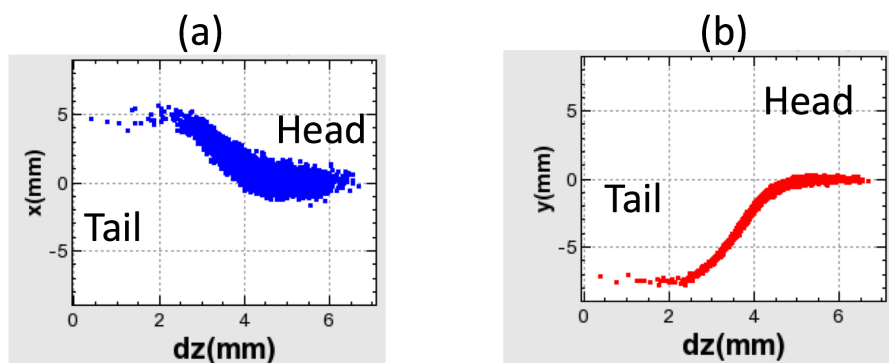

Figure 12.107: An example of the beam shape at the end of linac when the standard deviation of misalignment in Sector 3-5 is 0.15 mm. The horizontal axis shows the longitudinal direction, and the vertical axis represents (a) horizontal direction and (b) vertical direction.

   Figure 12.107 shows an example of simulation results when the misalignment between the accelerator structure and the quadrupole magnet is given in a normal distribution with a standard deviation of 0.15 mm. The misalignment in this case is assumed that the installation error of the accelerator tube and the quadrupole magnet follows a Gaussian distribution, and the orbit is not corrected. Since the tail is kicked by the wake field with respect to the head in the bunch, projecting in the lateral direction increases the beam size, resulting in an increase in projected emittance. Since the vertical beam size is about an order of magnitude smaller than the horizontal direction, the relative emittance growth is larger in the vertical direction even if the tail displacement is the same.

   The influence of the wake field depends on the beam optics of Sector 3-5. Figure 12.108[70] shows the effect of misalignment on emittance growth. For the several cases of the optics in Sector 3-5, triplet, doublet and singlet (FODO), the effects of misalignment on emittance growth are shown. The orbit correction was performed in the simulation. For the triplet and doublet, the results have almost the same, and if the misalignment σ is about 200 μm or less, there is no problem in the linac, but since there is no room for emittance increase, a misalignment less than 100 μm is desirable. Actually, a doublet is adopted. In the FODO case, no misalignment is allowed anymore.
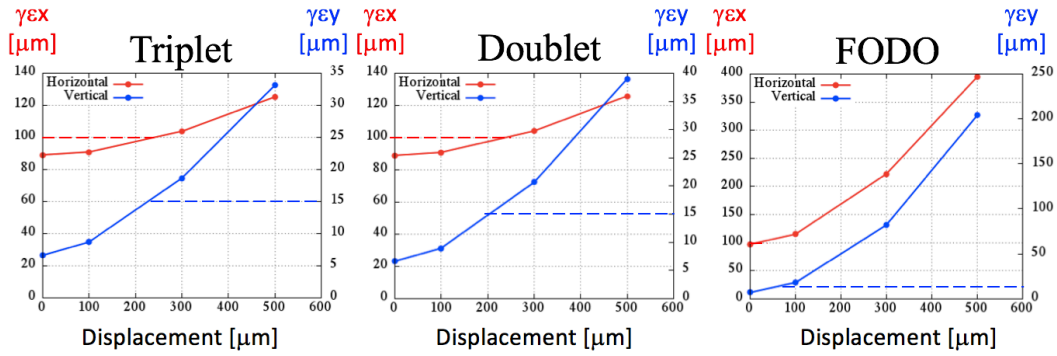
Figure 12.108: In each graph, the horizontal axis is the acceleration tube of Sector 3-5, the misalignment of the quadrupole magnet (1σ), the vertical axis is the normalized emittance (left axis: horizontal, right axis: vertical), and the dashed line is the request value from the main ring.

Above result is for the case where any positive correction is not done. On the other hand, there is a method called "offset injection" for reducing the effect of the wake field to some extent. This is to cancel each other out by selecting the proper trajectory and angle at the entrance of the linac[69]. Figure 12.109 shows the simulation results and Table 12.23 summarizes the results [70]. From Fig. 12.109, it can be seen that
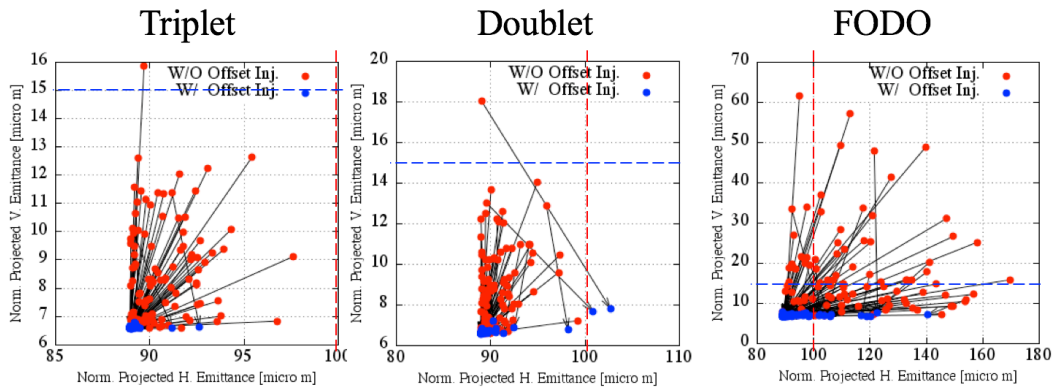

Figure 12.109: Simulation in each converging system when the misalignment of accelerator tube and quadrupole magnet in Sector 3-5 is $1\sigma = 100 \mu$ m. The horizontal axis is horizontal normalized emittance, and the vertical axis is vertical normalized emittance. The red and blue points show before and after the offset injection, respectively Before and after the offset incidence was connected with arrows. The dashed line is the required value from LER.

the emittance growth can be suppressed by the offset injection. However, in this case, the stabilities of the steering magnets that make the offset orbit might be a problem. When the kick angle jitter is 10 μrad or more, the normalized emittance is increased by 10 μm. For the stabilities of power supplies of pulsed steering in Sector 3-5, see the

623

Table 12.23: Emittance recovery when offset injection is performed in Sector 3-5.

Optics	$\gamma\varepsilon_x$ [μm]	$\gamma\varepsilon_x$ [μm] Offset injection	$\gamma\varepsilon_y$ [μm]	$\gamma\varepsilon_y$ [μm] Offset injection
Triplet	91	89	8.7	6.6
Doublet	91	89	8.9	6.6
FODO	115	93	17.9	6.9

Chapter 11.

Second-order Dispersion The energy spread of the beam is ±1.9 % after the BCS, and ±0.27 % at the BT to LER, where we define the spread as the width that contains 99 % of particles. For such low emittance beam from the DR, the emittance growth due to the second order dispersion is not negligible. As shown in Figure 12.110, the transverse positions and momenta are distorted at larger energy offset if not using a pair of sextupole correctors. The normalized emittances without/with sextupoles at the end of RTL and the BT are 67.7/62.8 (μm) and 3.97/3.23 (μm) respectively. The strengths of the sextupoles, K2, are 0.32 m^{-2} and 0.18 m^{-2} in the RTL, and 0.55 m^{-2} and 0.45 m^{-2}, respectively. No emittance growth is observed after the corrections.
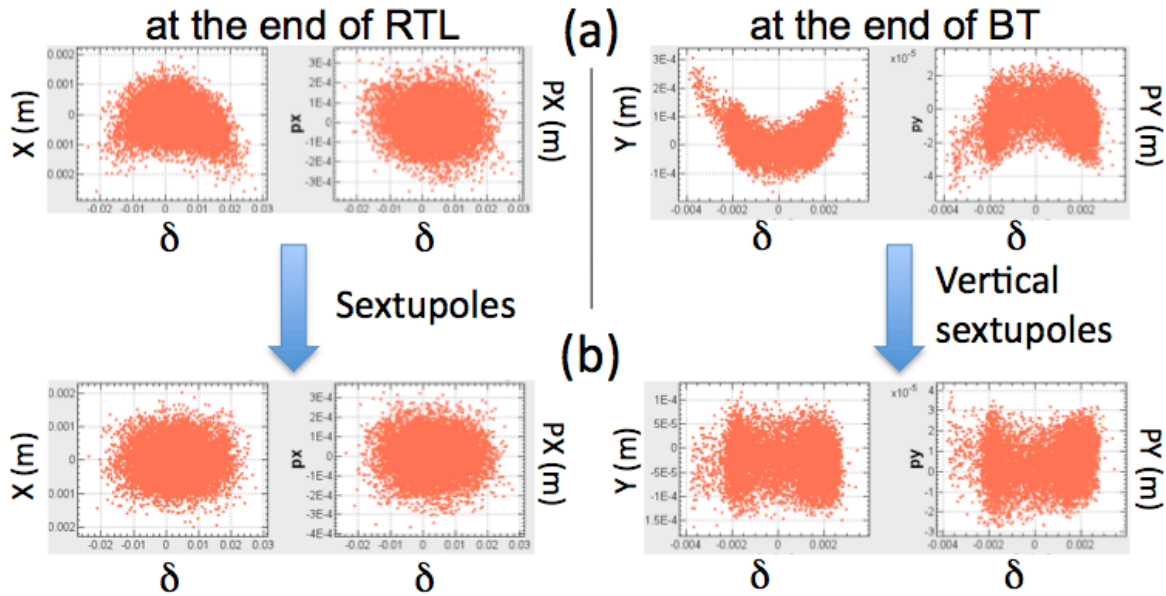

Figure 12.110: Correction of the second order dispersion using sextupoles at the end of RTL and BT. The figures show correlation plots of the transverse position as well as transverse momentum versus energy deviation for the case (a) without sextupoles, (b) with sextupoles.

Synchrotron Radiation in the BT The emittance growth due to the synchrotron radiation in the transport line between the linac and LER might not be negligible because the emittance itself is very small. The growth factor by this effect is, however only 9%(from 64 μm to 70 μm) in the horizontal plane and almost zero in the vertical. This effect is not an issue for the injection.
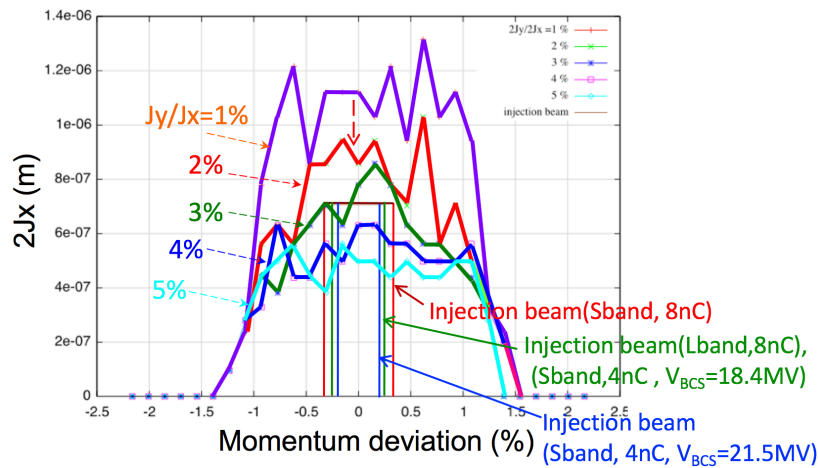
12.8.4 Injection into the main ring

Figure 12.111: Dependence of dynamic aperture of the main ring[71] on the vertical action of the injection beam. The horizontal axis is the momentum deviation and the vertical is the horizontal injection aperture. J_y/J_x is the ratio of the vertical action to the horizontal one of the injected beam. The rectangle region corresponds to the injected beam discussed so far.

The maximum horizontal-action and the energy deviation of injected beam are drawn as rectangles in Figure 12.111, for various combination of parameters. If a ratio J_y/J_x of the injected beam is less than 2%, which corresponds to the vertical action of 7 nm, the injected beam is within the dynamic aperture. The vertical emittance is thus less than 2.29 nm, assuming the transmission of 95.5 %. On the other hand, the vertical emittance assuming 5% coupling in the DR is 0.58 nm, which is well below the required value.

Beam-beam Effect

The last issue is the vertical emittance growth due to beam-beam effect. As shown in Figure 12.112, by the beam-beam kick from the stored beam the vertical emittance of the injected beam is transiently grown 16 times larger than that without beam-beam effect[72]. That is caused by the vertical incoherent motion. This is especially strong

in the nano-beam scheme, where the vertical beta function has very small waist at the interaction point. The particle with a large horizontal position and with nonzero vertical offset receives a beam-beam kick at the location that has a very large β_y. Due to the effect, 5.5 % beam particles are estimated to be lost in the main ring.
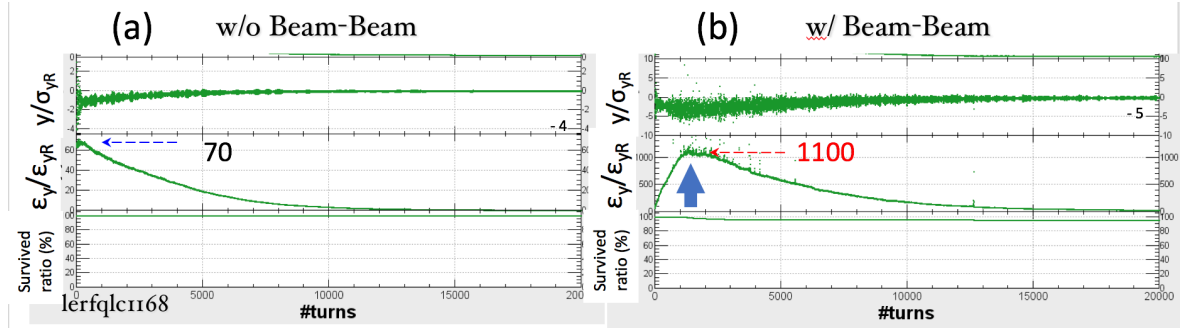

Figure 12.112: Evolution of the vertical emittance after injection in the LER, without(a) and with(b) beam-beam interaction. Top, middle, and bottom rows in each figure are the vertical position divided by equilibrium beam size, the vertical emittance divided by the design emittance, and the ratio of survives, respectively. A weak-strong model of the beam-beam effect[73] embedded in SAD has been applied.

12.9 Injection and extraction systems

12.9.1 Injection and extraction systems

Beam injection to DR is designed to be on-axis injection method. Injection system is composed of a septum magnet and two kicker magnets. The positron beam is bent by the septum magnet and the quadrupole magnet and injected to DR through thin slit of the vacuum chamber. The injection septum magnet is designed as a pulsed laminated magnet under vacuum with a single-turn water cooled coil.

On the other hand, the configuration of the extraction system is similar to the injection system, which is composed of an extraction septum magnet and two kicker magnets. The extraction septum magnet is designed as a pulsed laminated magnet under air with a ceramic vacuum chamber. We have avoided in-vacuum type septum magnet because it is located near the RF cavities.

12.9.2 Design of the septum magnet for injection

We have designed the eddy-current type septum magnet for the injection to DR. The eddy-current type septum can make the septum thickness thinner and makes the coil

design easier than the other type. Since the leakage fields to the circular beam is relatively large, we try to reduce the leakage fields by applying the full-sine pulse shape, which had been adopted by the KEKB injection septum [74]. Figure 12.113 shows the cross-sectional view of the injection septum and Figure 12.114 shows the picture of the magnet. The design parameters are listed in Table 12.24.
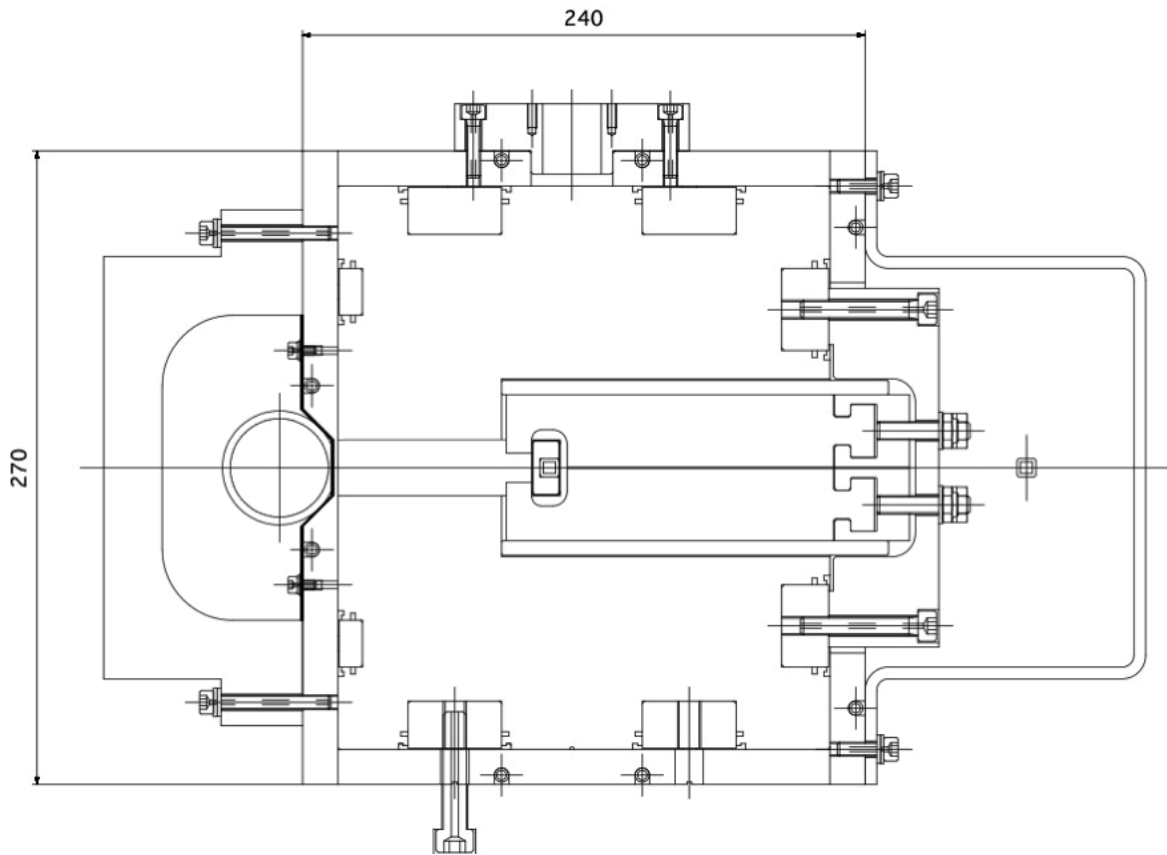

Figure 12.113: Cross-sectional view of the DR injection septum.

The wide aperture of 70^W mm x 24^H mm for the beam is required because the emittance of the injected positron emittance of 1400 nm-rad is very large. The magnet core is made of a laminated silicon steel with a thickness of 0.35 mm. The end plates are made of 25 mm thick HIP block (copper and stainless steel). These blocks have slits around the magnet gap which will mitigate the heating by the fringe fields. The laminated silicon steel and the end plates are welded with stainless steel flat bars for mechanical stiffness and are surrounded by copper plates to reduce the leakage field. Both of end plates and copper plates are cooled by water. The coil of magnet is one-turn and is made use of hollow-conductor with a ceramic coating of 0.3 mm thickness on it and wounded by Kapton film to protect against voltage breakdown. The coil is fixed by Si_3N_4 ceramic hooks to the return yoke by using locking nuts to resist loosening
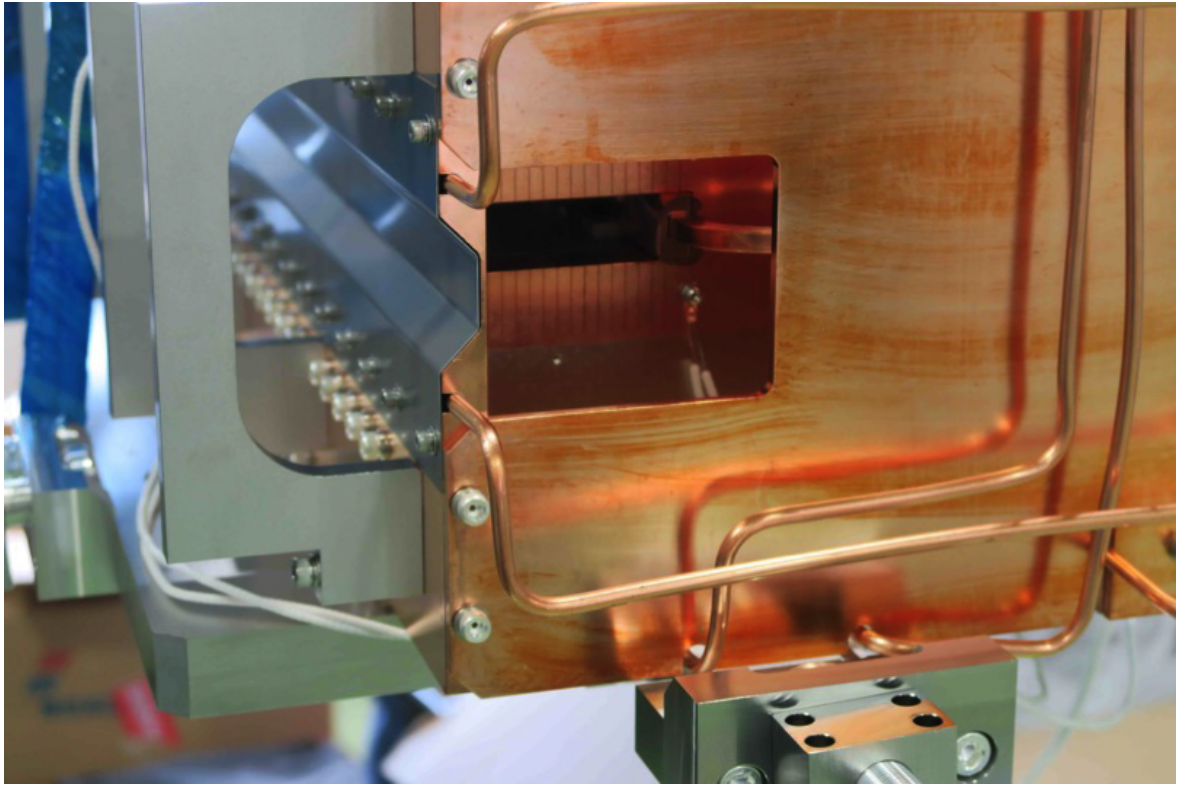
627

Figure 12.114: Photo of the DR injection septum magnet.

Parameters		unit
Deflection angle	79.2	mrad
No. of magnets	1	
Peak magnetic field	0.4	T
Septum thickness	4	mm
Core length	0.8	m
Magnet field aperture	$70^W \times 24^H$	mm
Maximum Peak current	8000	A
Pulse width	234 (full-sine wave)	μs
Repetition frequency	50	Hz

Table 12.24: Design parameters for the injection septum magnet.

from vibration. In order to reduce the leakage fields a silicon steel plate is attached to septum plate. Moreover the beam duct for circulating beam is made of iron yoke, inside of which are plated with 0.3 mm thick copper.

Injection septum magnet is installed in the vacuum chamber. The vacuum is common for both the injection and the ring. Four 300 l/s ion pumps are attached
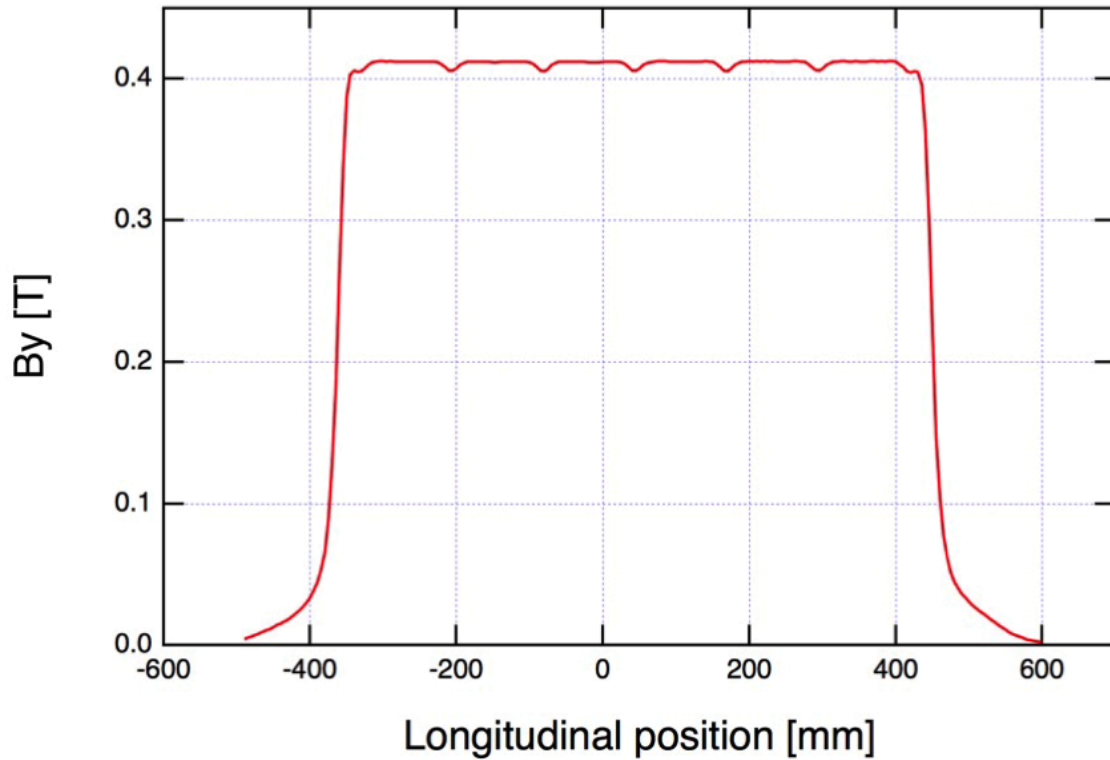
Figure 12.115: The field measurement results by pick up coil along the longitudinal direction.

to the chamber. The vacuum base pressure is less than 8×10^{-8} Pa after the 150 °C baking and the vacuum pressure under operation is about 1×10^{-7} Pa. Figure 12.115 shows the results of the magnetic field measurement with a pickup coil. Small dips on the flat top of the magnetic fields corresponds to the positions of the ceramic hook and the depth of the dip height depends on the horizontal position in the gap. The leakage fields for the circulating beam, which is shown in Figure 12.116, are less than 2 Gauss.

12.9.3 Design of septum magnet for the extraction from the DR

There are four circulating bunches in the DR, with a time spacing between bunches of about 100 ns and two bunches of those are extracted simultaneously by a single kicker-pulse, in turn, two new bunches are injected by a single pulse of the injection kicker. Whole process of the injection-extraction is repeated at up to 50 Hz. Requirements and main parameters for the extraction septum are shown in Table 12.25. Table 12.26 shows detailed specifications of the extraction septum. Definition of the parameters
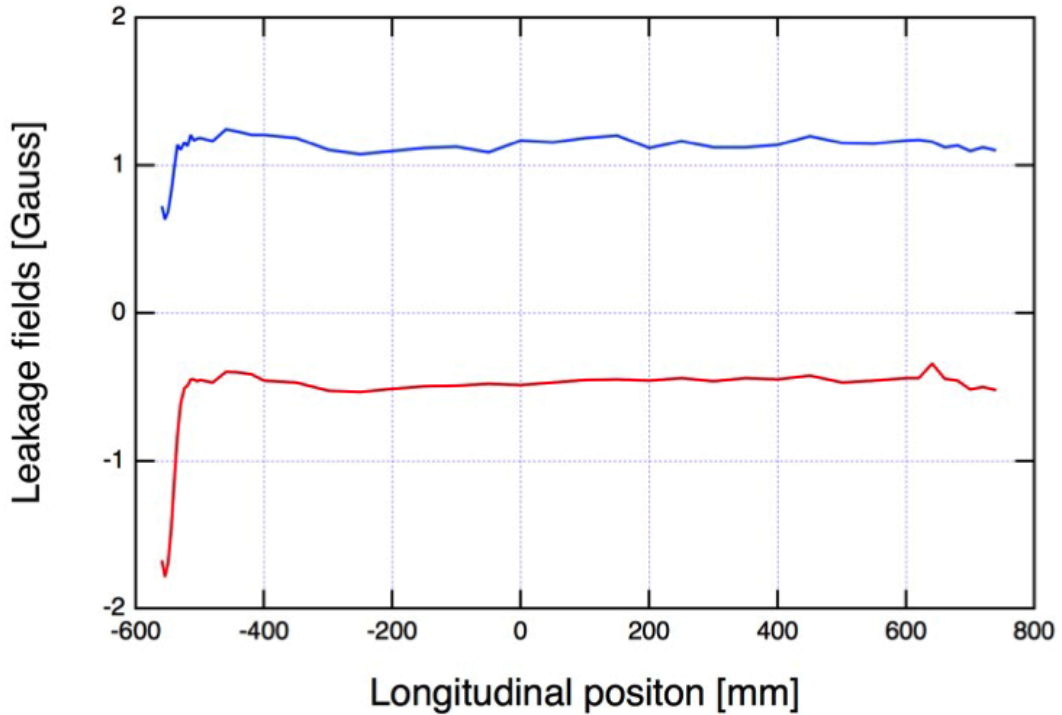
Figure 12.116: The field measurement results for the circulating beam. The probe position for the red and blue line is different in its horizontal position.

for the shim shape is shown in Figure 12.117. Eddy current type is adopted.

The extraction septum magnet is located at the downstream of the acceleration cavities. If the septum magnet is installed in the vacuum, the outgas from the core material might deteriorate the vacuum of the cavities that requires ultra-low vacuum pressure. Therefore, we have adopted the septum magnet operation in the atmosphere. Figure 12.118 shows the photo of the extraction septum magnet.

The extracted beam is guided into the vacuum chamber made of ceramics which is inserted in the gap of the magnet. Titanium coating of about 2 μm was made on the inner surface of the ceramics for preventing the charging-up on the ceramic surface. The vacuum chamber for the circulating beam is attached to the septum plate. For shielding of the leakage field, iron (STKM13A) is used at the material of the chamber. In order to reduce the beam impedance thin copper was plated with the thickness of 300 μm. Specifications of each duct are shown in Table 12.27.

Table 12.25: The main parameters for the extraction septum magnet.

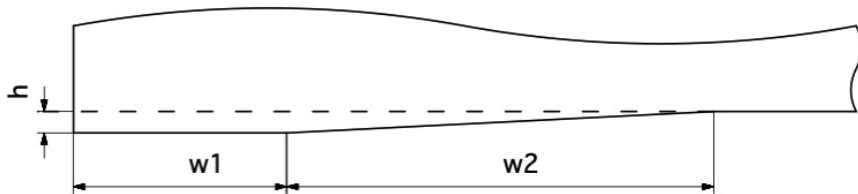| Parameters		unit
Extracted beam energy	1.1	GeV
No. of magnets	1	
Horizontal beam size	0.772	mm
Bending angle	104	mrad
Total septum thickness	10.5	mm
Field uniformity in the gap	< 0.025	%
Leakage magnetic field	< 1.3	Gauss

Figure 12.117: Definition of the parameters of the shim shape.

12.9.4 Power supplies for the DR injection and extraction septum

Circuit diagram is shown in Figure 12.119 . The septum magnet power supply consists of the following parts.

631

Table 12.26: Specifications for the extraction septum magnet.

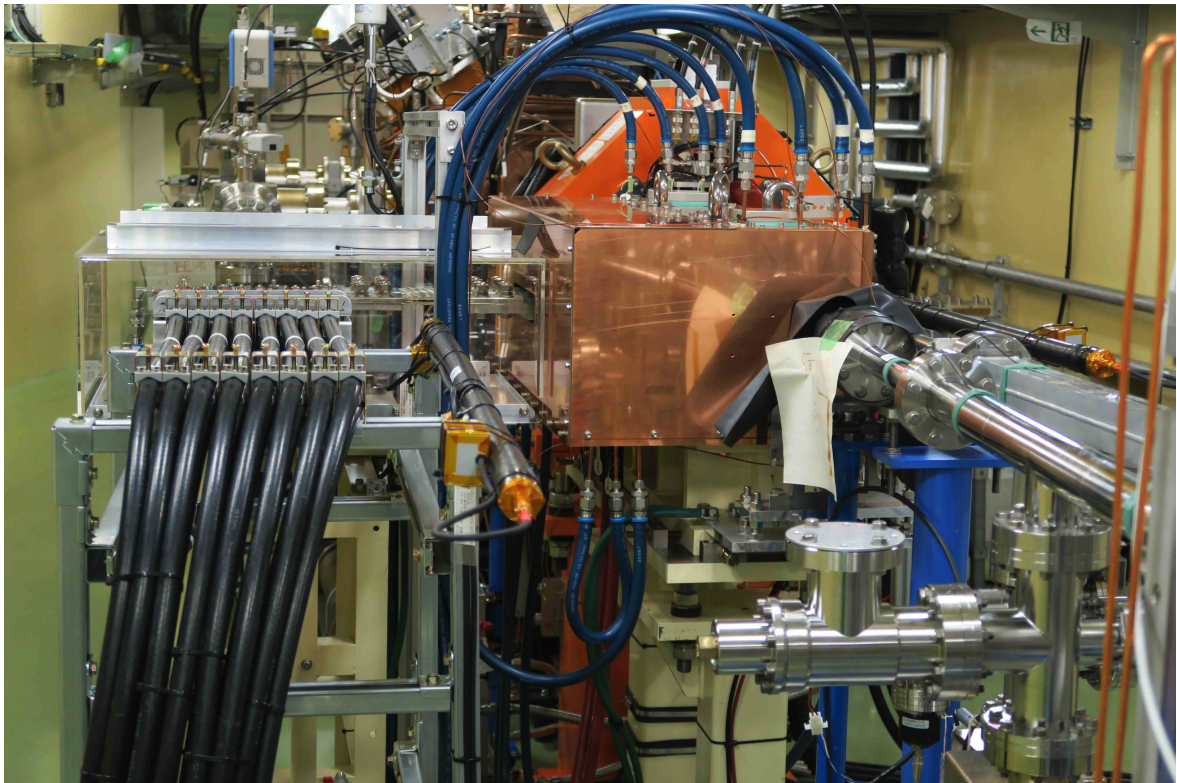| Parameters		unit
Magnetic field	0.477	T
Field uniformity in the gap	< 0.02	%
Maximum leakage field	< 1.0	Gauss
Core length	0.8	m
Gap width and height	$100^W \times 30^H$	mm
Shim dimension	1(w1)×2(w2)×0.1(h)	mm
Core width	70	mm
Laminated steel sheet thickness	0.35	mm
Inductance	5.85	μH
No. of magnet	1	

Figure 12.118: Photo of the DR extraction septum magnet.

Main charger

With the inverter and the high voltage unit, the storage capacitor for the resonant charge (C0) is charged to the predetermined voltage.

Table 12.27: Specifications of the ring chamber and the septum chamber.

Parameters		unit
Outer diameter of the ring chamber	48.6ϕ	mm
Inner diameter of the ring chamber	41.2ϕ	mm
Minimum thickness of the ring chamber	1.0	mm
Plating thickness of the ring chamber	300	μm
Total length of the ring chamber	1.5	m
Outer dimension of the ceramic chamber	$62^W \times 28^H$	mm
Inner dimension of the ceramic chamber	$52^W \times 17^H$	mm
Coating thickness of the ceramic chamber	2	μm
Full length of the extracted beam duct	1.16	m

Resonance charging

The resonance charge is performed between C0 and the main discharge condenser (C1) through inductor (L0) by turning-on the resonance charge thyristor (THY2). De-Qing circuit is operated by turning-on the thyristor (THY1) in a proper timing resulting C1 is charged to around 99 % of the final voltage.

Precision charger

C1 is charged to the demanded voltage by this precision charging system. Precision of the voltage of C1 is accomplished independent on the repetition of frequency. Figure 12.120 shows the charging voltage of C1 of the extraction septum magnet power supply.

Main discharge department

C1 is discharged by turning on the main discharge thyristors (THY3), which have 5 thyristors in series. In order to reduce the load inductance we have used the ten and fifteen cables in parallel between the magnet and the power supply for the injection and the extraction septum, respectively. Specifications of the power supplies for the injection and extraction septum magnet are shown in Table 12.28. Figure 12.121 shows the output current of the extraction septum.
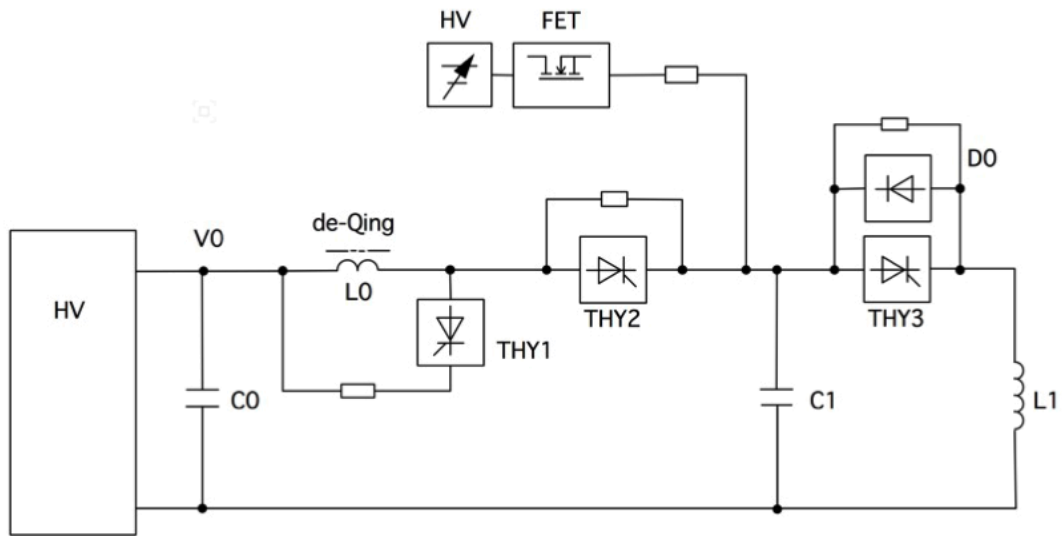
Figure 12.119: Basic circuit diagram of the DR septum magnet power supplies.

Table 12.28: Specifications of power supplies of the injection and the extraction septum magnet.

Parameters	Injection	Extraction	unit
Maximum current	8.0	12.5	kA
Maximum voltage	1.35	2.0	kV
Voltage stability	$< \pm 0.1$	$< \pm 0.01$	%
Timing jitter	$< \pm 0.3$		μs
Repetition frequency	50		Hz
Current waveform	Pseudo full-sine		
Pulse width	234	216	μs
Storage capacitance (C0)	20	16.7	mF
Capacitance of the main dischargers (C1)	225	225	μF
Inductance for resonant charge (L0)	1.0	1.0	μH
No. of output cables	10	15	
Load inductance @ 3.3 kHz (L1)	4.77	4.70	μH

12.9.5 Injection and extraction kicker magnets and its power supplies design

The circulating beam contains two trains that are separated about 100 ns, each having two bunches 96 ns apart. Because the injection and extraction kickers have to inject or
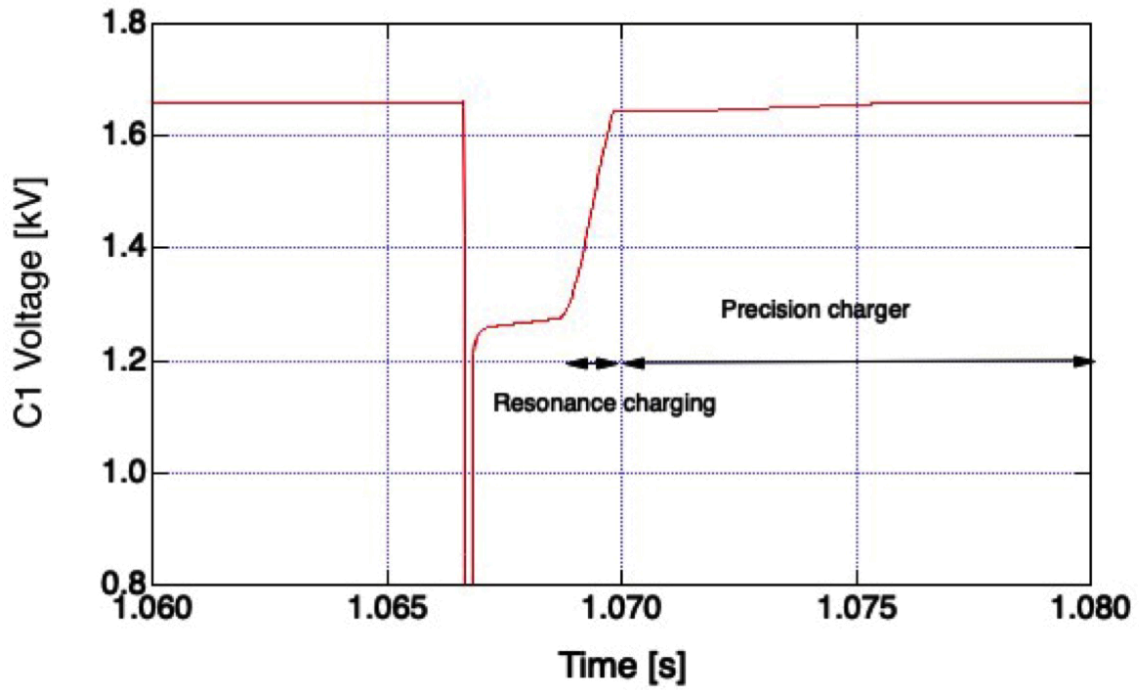
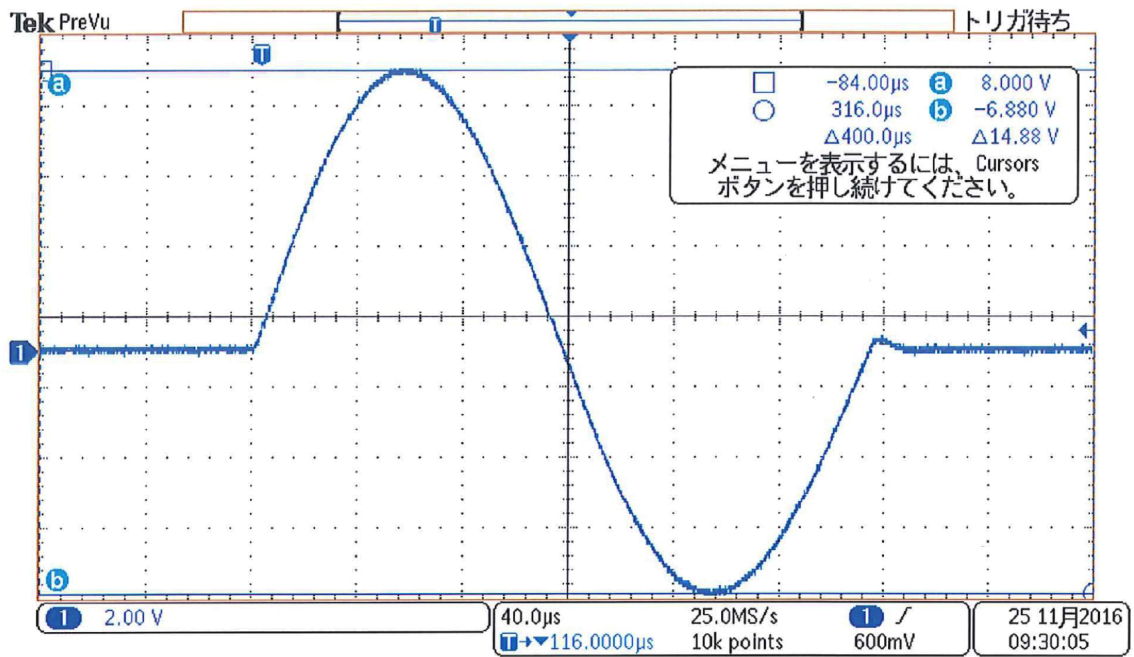Figure 12.120: Charging voltage of the main discharge condenser (C1) of the extraction septum.

Figure 12.121: Output current of the extraction septum magnet power supply.

extract two bunches with a single pulse, rise and fall time must be less than 100 ns. The kicker magnets for the injection and extraction have an identical design. The design parameters are listed in Table 12.29. Kicker magnets are designed as a conventional inductive (lumped) type that has a ceramic duct in the gap [75]. Schematic drawing of the kicker magnet is shown in Figure 12.122.

Parameters	Injection	Extraction	unit
No. of magnets		2	
Deflection angle	5.2	4.7	mrad
Peak magnetic field	0.04	0.036	T
Magnet core length		240	mm
Magnet field aperture		$82^W \times 53^H$	mm
No. of coil turn		1	
Magnet inductance		0.8	μH
Peak current	1708	1546	A
Voltage stability	$< \pm 1$	$< \pm 0.1$	%
Pulse width		300 (double half-sine)	ns
Rise time		< 100	ns
Fall time		< 100	ns
Timing jitter		< 1.4	ns
Frequency repetition		50	Hz

Table 12.29: Parameters table for DR Kickers.

Figure 12.123 shows the block diagram of the DR kicker power supply. Two HV chargers and two thyratrons and four magnetic switches are connected in parallel to the kicker magnet to produce double half sine pulse shape. The thyratrons and magnetic switches are placed in separate tanks filled with a silicone oil. The schematic drawing of the thyratron tank and magnetic switch tank are shown in Figure 12.124. Figure 12.125 shows the picture of kicker magnets and the power supplies. In order to produce a double half sine pulse shape, two independent power supplies are combined at their output terminals. Charging voltage and the turn-on timing can be controlled independently. A saturable inductor is used to achieve the short rise time of less than 100 ns. The leading current necessary for saturating the core of the inductor is expected to be less than 6 %. Since the magnetic field due to the leading current disturbs the bunches of the other train that are in the damping process the bunch-by-bunch feedback system is introduced. Bunch feedback system is indispensable to store four bunches in DR. Figure 12.126 shows the double pulse shape of the output current.
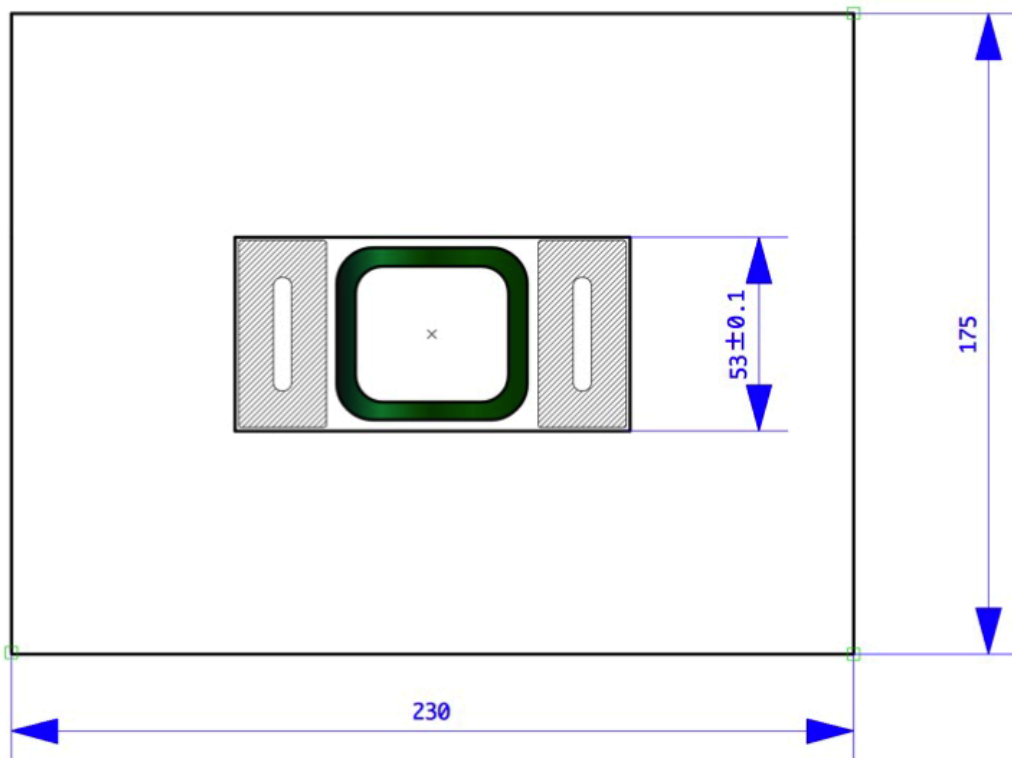
Figure 12.122: Schematic drawing of the cross-section of DR kicker magnet.

The voltage stability of 0.059 % (6 σ) and the switching jitter of 0.379 ns (3σ) have been achieved. Pre-pulse and tail noise are less than 6 %. However, long-term stability would be a concern because of a finite lifetime of thyratrons. We are developing a semiconductor switch using SI-thyristors in place of thyratrons.

The command chargers are used to charge the main capacitors in about 12 ms, holding the voltage in 0.1 ms before the thyratron is turned-on. Command charging has resulted in better performance in the stability. The midpoint of the coil is grounded and the applied voltage to the coil is twice of the charging voltage. Required timing jitter of the pulse is less than 1 ns, which are tight for usual operation of the thyratron, dc power supplies for the cathode's and reservoir's heater of the thyratrons are used. The low jitter E/O-O/E converter system has been developed for the low duty trigger pulse. Moreover a phase stabilized optical fiber is used in order to reduce the drift of the trigger timing by temperature.
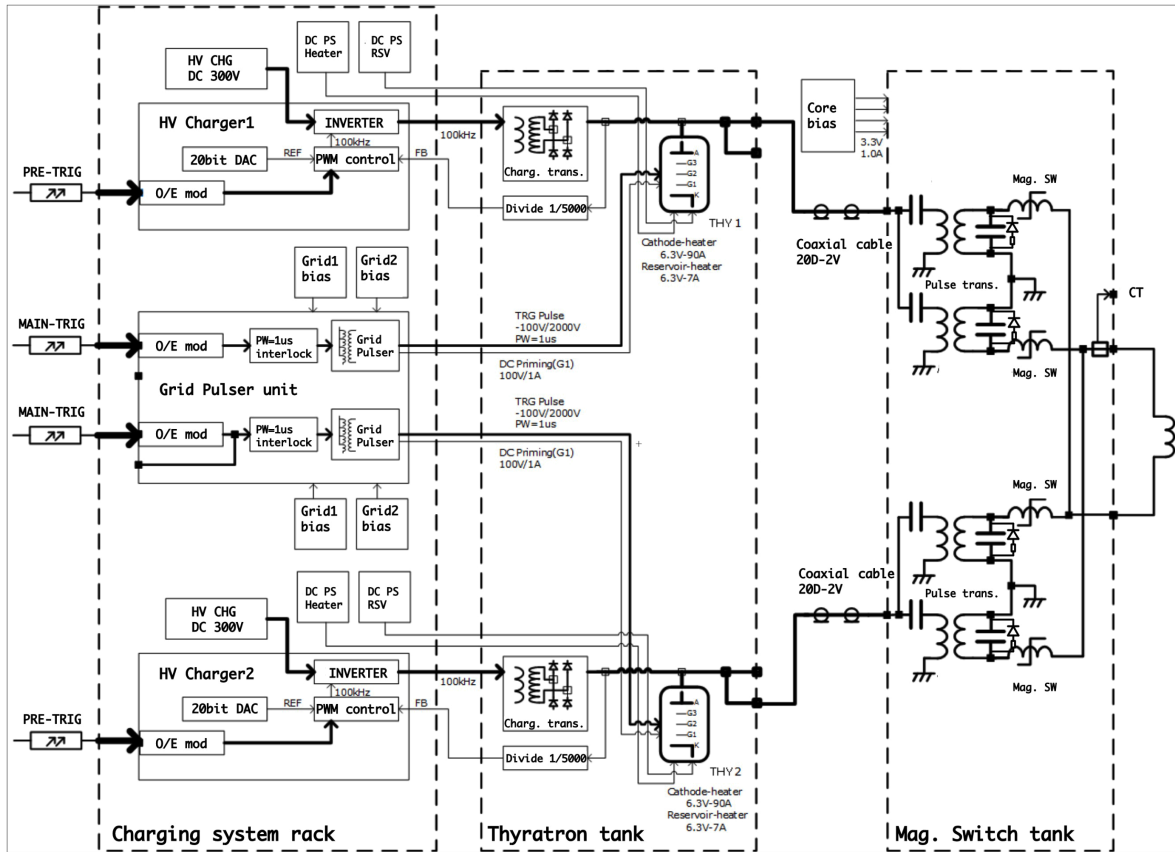
Figure 12.123: Block diagram of the DR Kicker power supply.

Ceramic duct for DR Kickers

Schematic drawing and the cross-sectional view of the ceramic duct is shown in Figure 12.127. Total length is 500 mm long for the injection kicker and 985 mm for the extraction, where two kicker magnets share a single ceramic duct.Because the coil is symmetrical and cannot be halved, in order to assemble the kicker magnet the flange of ceramic duct was designed to be removable. The ceramic duct is electrically isolated from the power supplies.

The inside of the ceramic duct has been coated with a titanium to sufficiently reduce the beam impedance. Because of very short rise and fall time, the penetration time as well as the attenuation of the magnetic fields due to eddy-current in the titanium coating is not negligible. The rise time of magnetic fields depends on the pulse shape as well as the surface resistivity. Figure 12.128 shows the opera-2d simulation results of the kicker fields for various titanium coating thickness [76]. Actually, however, the surface roughness of about 0.3 μm is expected because no surface-polishing were applied. We have chosen the coating thickness of 0.4 μm considering the surface of the ceramics and fluctuation in the thickness of the coating. The field measurements need
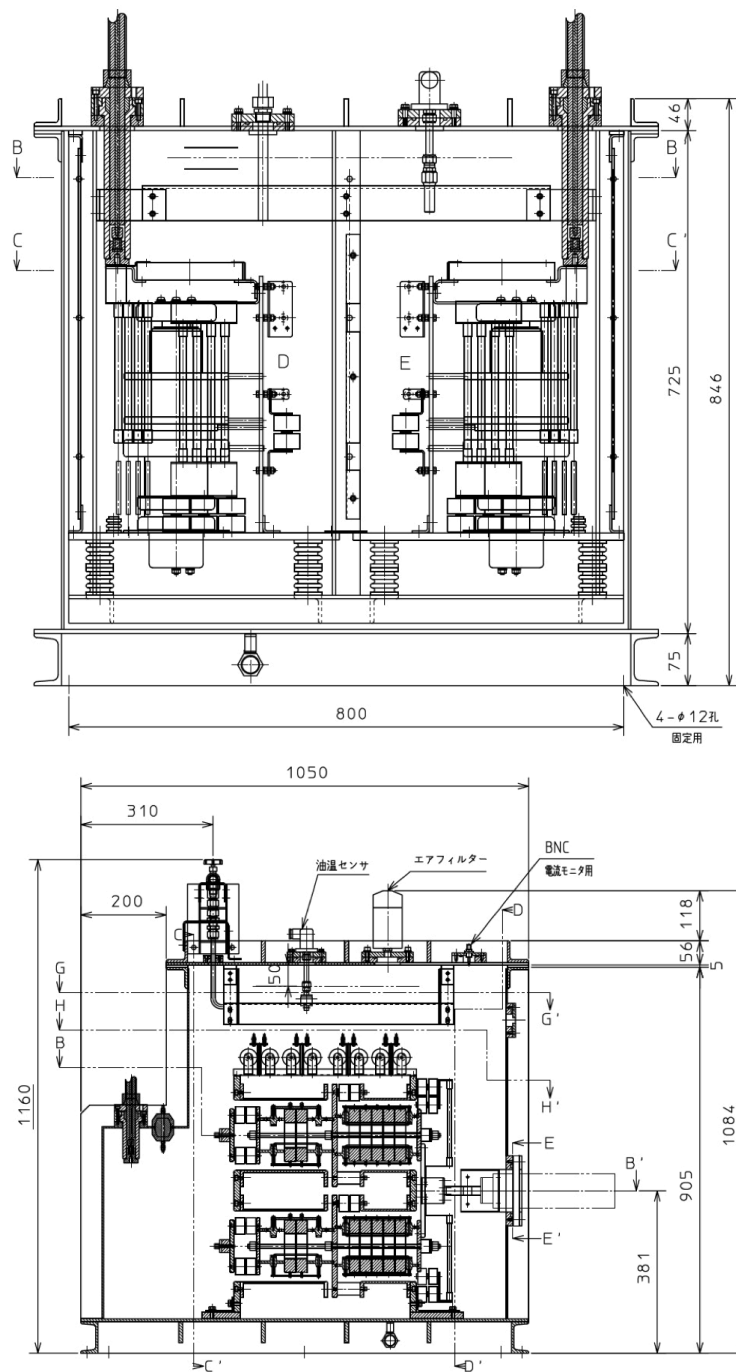
Figure 12.124: The drawing of the thyratron tank (up) and magnetic switch tank (down). Two thyratrons (e2V cx1836) are housed in a thyratron tank. The magnetic switch consists of four pulse transformers and four saturable inductances.

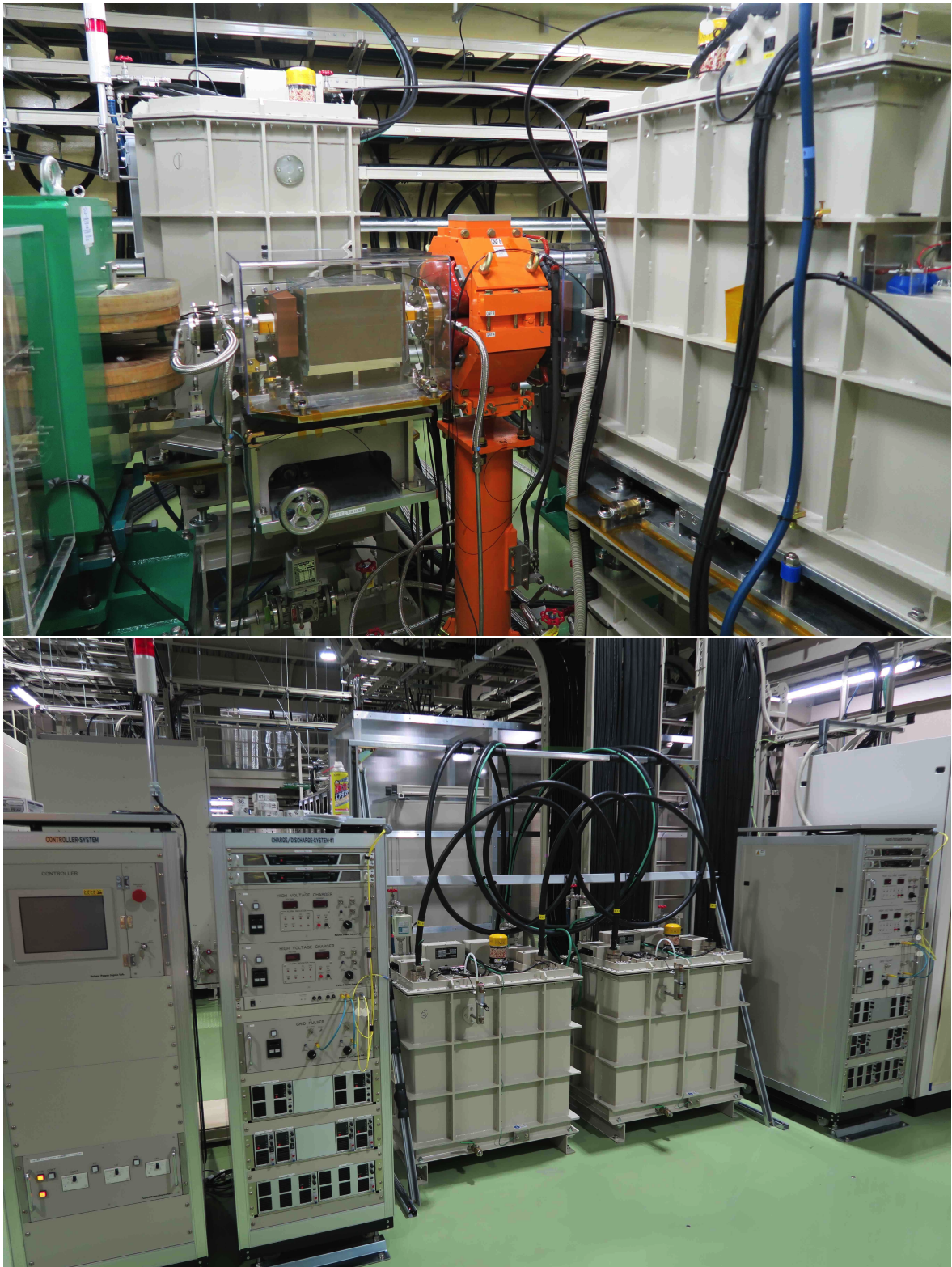to be performed with the ceramic duct inserted in the gap.

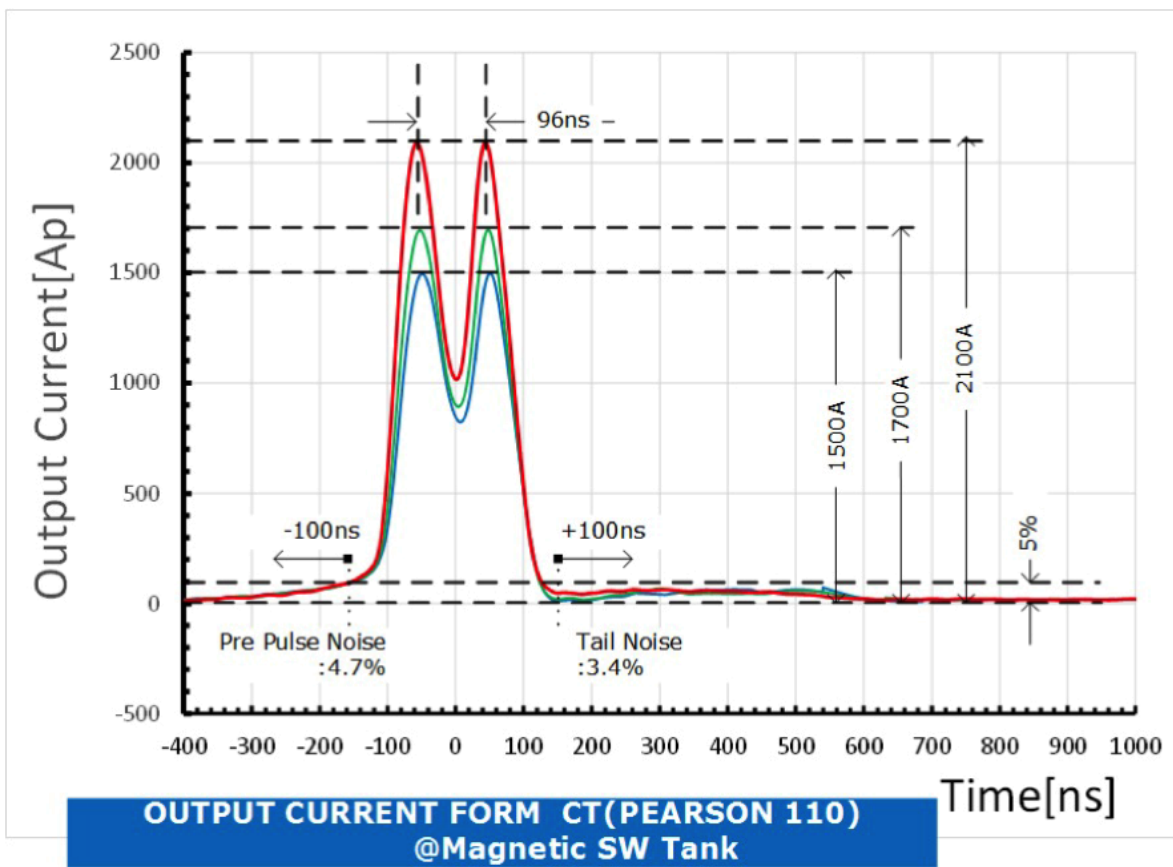Figure 12.125: Kicker magnets and its power supplies.

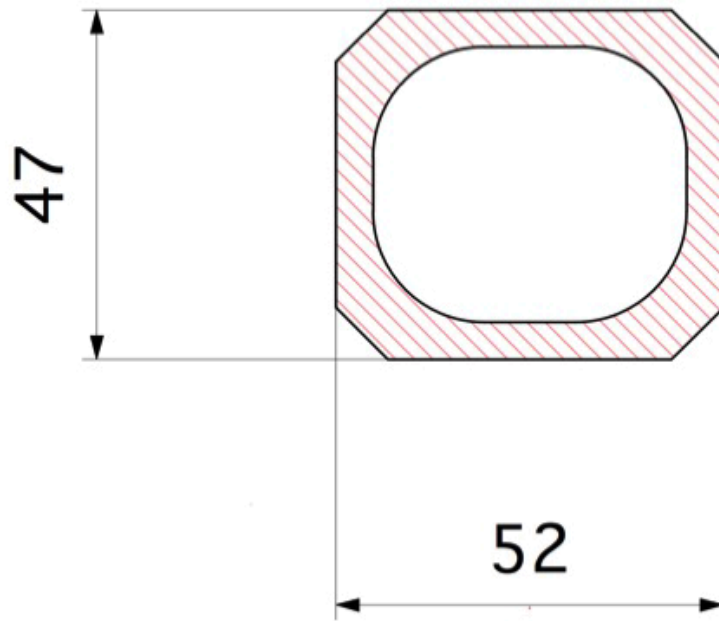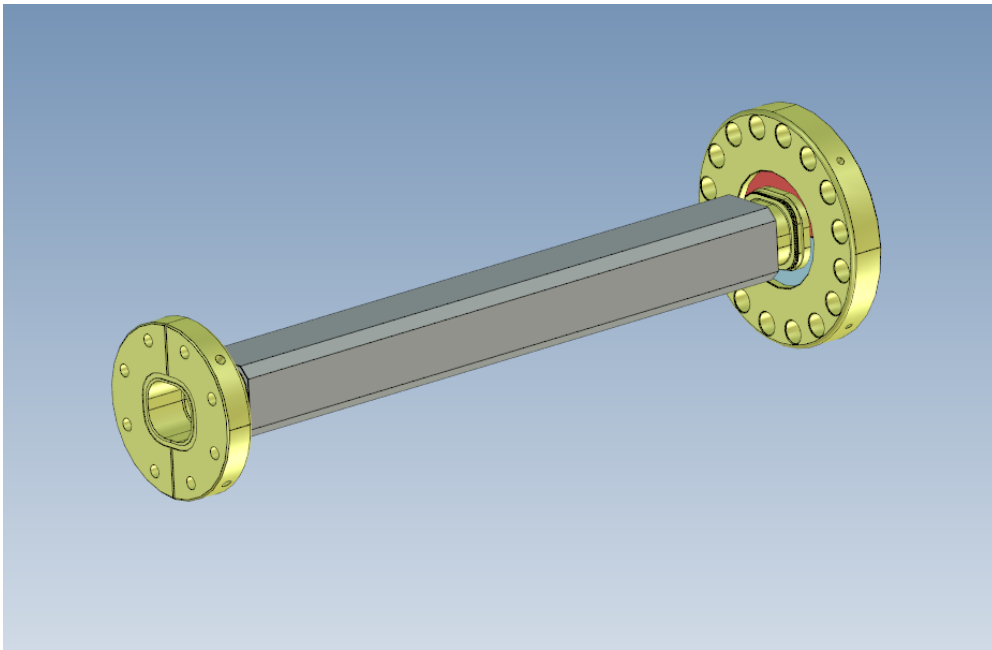Figure 12.126: Output current of the DR kicker magnet power supply.

Figure 12.127: Schematic drawing (up) and the cross-sectional view (down) of the ceramic duct for DR Kicker magnet.
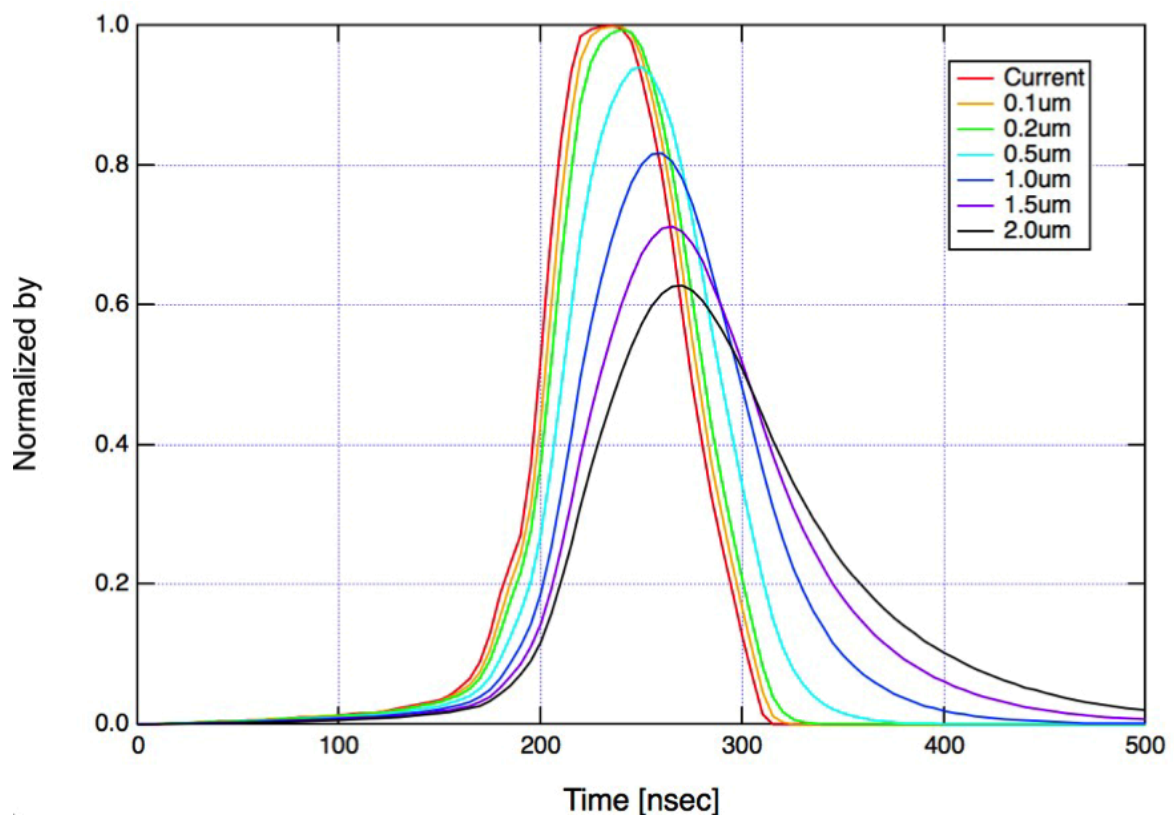
Figure 12.128: Simulation results of the magnetic fields with various titanium coating thickness. The red line indicates the case without the titanium coating. The other lines correspond to various thickness in the titanium coating.

Bibliography

[1] M. Kikuchi, "Reverse-bend FODO lattice applied to damping ring for SuperKEKB", Nucl. Instr. Meth. A 556, pp.13-19 (2006).

[2] J. A. Nelder and R. Mead, The Computer Journal 7, 308 (1965).

[3] H. Sugimoto *et al.*, in Proc.of IPAC2017,Copenhagen (Denmark, 2017) pp. 705-707.

[4] http://www.gdfidl.de/

[5] K. Oide, Proceedings of PAC ' 09, Vancouver, BC, Canada, MO3RAI01 (2009).

[6] H. Ikeda,"Effect of Coherent Synchrotron Radiation at the SuperKEKB Damping Ring", Proceedings of IPAC ' 11, San Sebastian, Spain, THPZ021 (2011).

[7] D. Zhou, et al.," CSR impedance for an ultrarelativistic beam moving in a curved trajectory " ,Proceedings of IPAC ' 11, San Sebastian, Spain, WEPC108 (2011).

[8] D. Zhou et al., "Interference od CSR fields in a curved waveguide", Proceedings of IPAC ' 11, San Sebastian, Spain, MOPS007 (2011).

[9] H. Ikeda et al., "Coherent synchrotron radiation predicted at the SuperKEKB damping ring", Proceedings of IPAC2013, Shanghai, China, TUPME014 (2013).

[10] Robert L. Warnock, SLAC-PUB-11955(2006).

[11] K. L. F. Bane, Y. Cai, and G. Stupakov, Phys. Rev. ST Accel. Beams 13, 104402 (2010).

[12] L. Wang et al., "Varidiation of the microwave instability in the damping ring of SuperKEKB using VFP solver", Proceedings of IPAC2013, Shanghai, China, TUPME017 (2013).

[13] K. Ohmi, "Electron cloud instabilities in the damping ring of International Linear Collider", KEK Preprint 2005-100 (2006).

[14] L. F. Wang et al., "Numerical study of the photoelectron cloud in KEKB Low Energy Ring with a three-dimensional particle in cell method", PRST-AB 5, 124402 (2002).

[15] K. Ohmi, "Particle-in-Cell Simulation of Beam-Electron Cloud Interactions", PAC2001, Chicago, IL, 1895-1897(2001).

[16] T. Ueda, et.al., "Tuning of the Magnetic Measurement System for the SuperKEKB Damping Ring", Proceedings of the 12th Annual Meeting of Particle Accelerator Society of Japan, 2015, pp.665-669.

[17] Y. Suetsugu, K. Shibata, H. Hisamatsu, M. Shirai, K. Kanazawa, "Development of copper beam ducts with antechambers for advanced high-current particle storage rings", Vacuum 84, p.694 (2010).

[18] K. Ohmi and F. Zimmermann, "Head-Tail Instability Caused by Electron Clouds in Positron Storage Rings", Phys. Rev. Lett. 85, p.3821 (2000).

[19] Y. Suetsugu, K. Kanazawa and K. Ohshima, "Bellows Design and Testing for KEKB", Vacuum 47, p.629 (1996).

[20] H. Ikeda, T. Abe, M.Kikuchi, K.Oide, K.Shibata, M.Tobiyama, and D.Zhou, "EFFECT OF COHERENT SYNCHROTRON RADIATION AT THE SUPERKEKB DAMPING RING", Proceedings of IPAC'11, San Sebastián, Spain (2010), p.3732.

[21] O. Gröbner, A. G. Mathewson, H. Störi and P. Strubin, "Studies of photon induced gas desorption using synchrotron radiation", Vacuum 33, p.397 (1983).

[22] M. Seidel, "Approximate Integrals of Synchrotron Radiation Spectra", DESY Report No. DESY-HERA-03-26 (2003).

[23] G. Dugan, and D. Sagan, "Synrad3D Photon Propagation and Scattering Simulation", Proceedings of ECLOUD 2010: 49th ICFA Advanced Beam Dynamics Workshop on Electron Cloud Physics, PST08, Ithaca, New York, USA (2010), p.118.

[24] Y. Suetsugu, H. Fukuma, M. Pivi, L. Wang, "Continuing study on electron-cloud clearing techniques in high-intensity positron ring: Mitigation by using groove surface in vertical magnetic field", Nuclear Instruments and Methods in Physics Research A 604, p.449 (2009).

[25] M. Tobiyama, M. Arinaga, J. W. Flanagan, H. Fukuma, H. Ikeda, H. Ishii, K. Mori and M. Tejima, "BEAM POSITION MONITORS FOR SuperKEKB DAMPING RING", Proceedings of the 8th Annual Meeting of Particle Accelerator Society of Japan, MOPS080, Tsukuba, Japan, 1-3 August 2011, p.507 (2011). (in Japanese)

[26] M. Tobiyama, H. Fukuma, K. Shibata, M. Tejima, S. Hiramatsu, K. Mori, H. Ishii, and T. Obina, "DEVELOPMENT OF BUTTON ELECTRODES FOR SU-PERKEKB RINGS" Proceedings of BIW10, Santa Fe, New Mexico, USA (2010), p.223.

[27] J. Le Duff, "CURRENT AND CURRENT DENSITY LIMITATIONS IN EX-ISTING ELECTRON STORAGE RINGS", Nuclear Instruments and Methods in Physics Research A 239, p.83 (1985).

[28] Molflow+, https://molflow.web.cern.ch

[29] K. Shibata, H. Hisamatsu, K. Kanazawa, Y. Suetsugu, M. Shirai, "DEVEL-OPMENT OF TiN COATING SYSTEM FOR BEAM DUCTS OF KEK B-FACTORY", the 11th European Particle Accelerator Conference, EPAC'08, Genoa, Italy, 23-27 Jun 2008, TUPP071, p.1700 (2008).

[30] K. Shibata, "SuperKEKB VACUUM SYSTEM", Proceedings of ECLOUD'12: Joint INFN-CERN-EuCARD-AccNet Workshop on Electron Cloud Effects, La Biodola, Isola d'Elba, Italy (2012), p.67 (2012).

[31] K. Shibata, Y. Suetsugu, H. Hisamatsu, M. Shirai, "TiN COATING FOR BENT BEAM PIPES", Proceedings of the 11th Annual Meeting of Particle Accelerator Society of Japan, Aomori, Japan, 9-11 August 2014, p.1342 (PASJ2014-SUP115) (2014). (in Japanese)

[32] T. Abe, T. Kageyama, H. Sakai, Y. Takeuchi, and K. Yoshino, "RF Accelerating Structure for the Positron Damping Ring of the SuperKEKB Injector," in Proceedings of the 8th Annual Meeting of Particle Accelerator Society of Japan, August 2011 (Paper ID: TUPS131).

[33] T. Abe, T. Kageyama, H. Sakai, Y. Takeuchi, and K. Yoshino, "Development of RF Accelerating Cavity for the Positron Damping Ring at SuperKEKB," in Proceedings of the 9th Annual Meeting of Particle Accelerator Society of Japan, Aug. 2012 (Paper ID: THLR06).

[34] T. Kageyama, et al., "The ARES cavity for KEKB," presented at the 1st Asian Particle Accelerator Conference (APAC 98), Tsukuba, Japan, 1998 (KEK Report No. KEK-PREPRINT-98-45).

[35] H. Ikeda, T. Abe, M. Kikuchi, K. Oide, K. Shibata, M. Tobiyama, and D. Zhou, "Effect of Coherent Synchrotron Radiation at the SuperKEKB Damping Ring," Conf. Proc. C **110904**, 3733 (2011).

[36] F. Naito, et al., "The Input Coupler for the KEKB ARES Cavity," in Proceedings of the 1st Asian Particle Accelerator Conference (APAC 98), Tsukuba, Japan, 1998 (KEK Preprint No. 98-44).

[37] T. Kageyama, "Grooved Beam Pipe for Damping Dipole Modes in RF Cavities," KEK-PREPRINT-91-133, 1991.

[38] Y. Takeuchi et al., "HOM Absorber for the ARES Cavity," KEK-PREPRINT-97-36, PAC97, 1997.

[39] Y. Takeuchi, T. Abe, T. Kageyama, H. Sakai, K. Yoshino, A. Arai, M. Ando, "Control of RF Dielectric Properties of SiC Ceramics for HOM Absorbers", in Proceedings of the 8th Annual Meeting of Particle Accelerator Society of Japan, Aug. 2011 (Paper ID: TUPS137).

[40] http://www.gdfidl.de/

[41] https://www.cst.com/

[42] T. Abe, T. Kageyama, H. Sakai, Y. Takeuchi, and K. Yoshino, "High Power Testing of the RF Accelerating Cavity for the Positron Damping Ring at SuperKEKB," in Proceedings of the 10th Annual Meeting of Particle Accelerator Society of Japan, August 2013 (Paper ID: SAP057).

[43] The actual moving range of the tuner for the DR cavity is within 10 to 30 mm.

[44] T. Abe, T. Kageyama, H. Sakai, Y. Takeuchi, and K. Yoshino, "RF Accelerating Structure for the Damping Ring of the SuperKEKB Injector," Conf. Proc. C **100523**, WEPE087 (2010).

[45] H. Kaji, et al., "Upgrade of Event Timing System at SuperKEKB", Proc. of ICALEPCS2013, THCOCA04 (2013) ; http://www-linac.kek.jp/linac-paper/2013/ical13-kaji-event.pdf

[46] K. Furukawa, et al., "Accelerator control system at KEKB and the linac", Progress of Theoretical and Experimental Physics (2013) 03A008; http://ptep.oxfordjournals.org/content/2013/3/03A008.full

[47] H. Ikeda et al," Beam diagnostics of SuperKEKB damping ring", in Proceedings of IBIC2013, Oxford, UK, MOPC051.

[48] M. Tobiyama, H. Fukuma, K. Shitaba, M. Tejima, S. Hiramatsu, K. Mori, T. Ishii and T. Obina, in proceedings of Beam Instrumentation Workshop 2010, Santa Fe, 2010.

[49] http://www.gdfidl.de/

[50] Stanford Research Systems, http://www.thinksrs.com/

[51] Masaki Tejima, Doctoral thesis.

[52] W. D. Peterson, "The VMEbus Handbook", ISBN 1-885731-08-6.

[53] ANSYS HFSS

[54] Dimtel Inc. http://www.dimtel.com/

[55] M. Tobiyama and J. W. Flanagan, in proceedings of IBIC2012, Tsukuba, 2012.

[56] H. Ikeda et al., in Proceedings of Annual Meeting of Particle Accelerator Society of Japan, Tsukuba, Japan, 2011.

[57] M. Born and E. Wolf, Principles of Optics, Cambridge, 1999.

[58] KEKB Accelerator Papers, NIM. A499 (2003).

[59] Kwang-Je Kim, in Proceedings of AIP 184 (1989).

[60] H. Ikeda et al," Beam loss monitor at SuperKEKB", in Proceedings of IBIC2014, Monterey, CA, USA, TUPD22.

[61] N. Iida *el al.*, "Design of the Positron Transport System for SuperKEKB", IPAC2010, THPD004.

[62] N. Iida *el al.*, "Beam Dynamics in Positron Injector Systems for the Next Generation B-factories", IPAC2011, THYA01.

[63] N. Iida *el al.*, "Commissioning of Positron Damping Ring and the Beam Transport for SuperKEKB", eeFACT2018, TUPAB07.

[64] M. Kikuchi, "Reverse-bend FODO lattice applied to damping ring for SuperKEKB", Nucl. Instr. Meth. A556, pp.13-19 (2006).

[65] M. Kikuchi *el al.*, TUPEB054, "Design of Positron Damping Ring for SuperKEKB", Proc. IPAC'10, Kyoto, Japan, May. 23-28, 2010.

[66] Strategic Accelerator Design (SAD) home page, `http://acc-physics.kek.jp/SAD/`.

[67] `https://www.dropbox.com/s/yrzf8wzoblojta9/SuperKEKB-DRBT_movie.ppt?dl=0`.

[68] K. Yokoya, private communication.

[69] L. Zang *el al.*, "KEKB LINAC Wakefield Studies of Comparing Theoretical Calculation, Simulation and Experimental Measurement", IPAC2011, MOPS058.

[70] H. Sugimoto, private communication.

[71] Y. Ohnishi, private communication.

[72] Y. Ohnishi, private communication.

[73] K. Ohmi *el al.*, "BEAM-BEAM SIMULATION STUDY FOR CEPC, Proc. IPAC2014, Dresden, Germany, ISBN: 978-3-95450-132-8 doi:10.18429/JACoW-IPAC2014-THPRI003 (2014).

[74] KEK-B: The KEK B-factory, Nuclear Instruments and Methods in Physics Research Section A, Volume 499, Issue 1.

[75] M. Tawada et al., Development of injection and extraction SuperKEKB Damping Ring.

[76] http://operafea.com/